

**On the Dynamics of Single-Electron Tunneling
in
Semiconductor Quantum Dots under
Microwave Radiation**

A Dissertation
Submitted to the Physics Department
of
Ludwig-Maximilians-Universität München

by
Hua Qin
from Wujin, China

30th July 2001, München

1. Gutachter: Prof. Dr. J. P. Kotthaus

2. Gutachter: Prof. Dr. W. Zwerger

Tag der mündlichen Prüfung: 26th July 2001

Abstract

Efforts are made in this thesis to reveal the dynamics of *single-electron tunneling* and to realize *quantum bits* (qubits) in semiconductor quantum dots. At low temperatures, confined single quantum dots and double quantum dots are realized in the two-dimensional electron gas (2DEG) of AlGaAs/GaAs heterostructures. For transport studies, quantum dots are coupled to the drain and source contacts via tunnel barriers. Electron-electron interaction in such closed quantum dots leads to Coulomb-blockade (CB) effect and single-electron tunneling (SET) through discrete quantum states. SET and its dynamics in single and double quantum dots are studied using both transport and microwave spectroscopy.

In transport spectroscopy, SET is monitored by measuring the direct tunnel current through the quantum dots in both the linear and nonlinear transport regimes, where ground states and excited states of the quantum dots are resolved. In a double quantum dot, *bonding* and *anti-bonding* molecular states are formed. Quantum dots proved to be well controlled quantum mechanical systems. In analogy to real atoms and molecules, single quantum dots and double quantum dots are termed *artificial atoms* and *artificial molecules*, respectively.

In microwave spectroscopy, continuous microwave radiation is applied to quantum dots. *Photon-assisted tunneling* (PAT) through the ground state and excited states is observed in single quantum dots. In a double quantum dot, the molecular states can be coherently superimposed by microwave photons, inducing the *Rabi oscillations* and a net direct tunnel current which is experimentally measurable. A qubit is formed in a double quantum dot.

Two new microwave spectroscopy techniques are developed in this thesis to explore the dynamics of PAT (SET) in quantum dots. Both techniques are called *heterodyne detection* of photon-induced tunnel current (photocurrent). In one method, two coherent *continuous* microwave sources with a slight frequency offset are combined to generate a flux of microwave photons. The photon intensity varies in time at the offset frequency. The induced alternating photocurrent at the offset frequency is detected by a lock-in amplifier. The in-phase component of the photocurrent reflects the tunneling strength, and the out-of-phase component reveals the dynamics of electron tunneling. In the other method, two coherent *pulsed*, i.e., broadband, microwaves are applied to irradiate the quantum dots, where the dynamic charge relaxation and the pumping by microwave pulses are studied. Both techniques allow to resolve PAT in the nonlinear transport regime. A long charge relaxation time of single quantum dots is found by using both techniques. No superposition of the ground state and the excited state is achieved.

Contents

1	Introduction	1
1.1	Quantum Dot Fabrication	5
1.2	Methods of Characterizing Quantum Dots	9
2	Coulomb-Blockade Effect and Single-Electron Tunneling: Theory	11
2.1	Metallic Islands	12
2.2	Single Quantum Dots	15
2.2.1	Weak Coupling to Contacts	16
2.2.2	Strong Coupling to Contacts	22
2.3	Coupled Double Quantum Dots	23
2.3.1	Weak Coupling between the Dots	26
2.3.2	Strong Coupling between the Dots	29
3	Transport Spectroscopy of Semiconductor Quantum Dots: Experiment	35
3.1	Charging Effect in An Array of Silicon Nanocrystals	35
3.2	Transport Spectroscopy of Artificial Atoms: Single Quantum Dots	39
3.2.1	Formation of A Single Quantum Dot	39
3.2.2	Level Spectroscopy	41
3.3	Transport Spectroscopy of An Artificial Molecule: A Double Quantum Dot	48
3.3.1	Formation of A Tunnel-Coupled Double Quantum Dot	48
3.3.2	Characterization of the Double Quantum Dot	51
3.3.3	Interaction of Molecular States with Acoustic Phonons	52

4	Photon-Assisted Tunneling in Semiconductor Quantum Dots: Theory	57
4.1	Photon-Assisted Tunneling through A Single Quantum Dot	58
4.2	Photon-Assisted Tunneling through A Double Quantum Dot	62
5	Microwave Spectroscopy of Semiconductor Quantum Dots: Experiment	67
5.1	Photon-Assisted Tunneling in A Single Quantum Dot	68
5.2	Microwave Spectroscopy of A Double Quantum Dot	73
5.3	Heterodyne Detection of Photon-Assisted Tunneling in A Single Quantum Dot	83
5.4	Broadband Microwave Spectroscopy of A Single Quantum Dot	95
6	Conclusion and Outlook	107
A	Fabrication Details and Quantum Dot Samples	111
B	Measurement Setup	117
C	Equivalent Circuit of A Double Dot	123

Chapter 1

Introduction

Since the invention of the semiconductor transistor in 1947 [BB48], this technology has led to a revolution in computation, information processing, and communication devices. All this has had a great impact on most peoples' work and our daily life. Nowadays, the most common electronic transistor is the Complementary Metal-Oxide-Semiconductor (CMOS) field-effect transistor [Sze85]. The physics involved is based on classical diffusive electron transport. Higher operation speed requires a further reduction of the device dimensions and a much smaller power dissipation. This will eventually lead to a break-down of the classical approach when the device dimension will be comparable to the Fermi wavelength and hence to the electron's phase coherence length. Recent advances in material science and modern nanometer fabrication techniques enable the fabrication of nanometer sized quantum electronic devices, in which electron transport is described by quantum mechanics.

The aim of this work is to investigate transistors in this quantum limit beyond the regime of classical physics. Transistors in this quantum regime are small regions of conducting material in which only 10 to 100 electrons are confined, hence they are also termed *quantum dots*. Since the dot's diameter is comparable to the Fermi wavelength, discrete electronic states can be distinguished similar to real atoms. In this sense, quantum dots can be called *artificial atoms* [HK93, Kas93, Ash96], while coupled quantum dots can be seen as artificial molecules. In addition to the energy quantization the number of electrons in the dots is well defined. This is due to the strong electron-electron interaction, which can be approximated by a constant capacitance (C_Σ) of the dot. A charging energy e^2/C_Σ , which can be much larger than the thermal energy, is required to add a single electron to the quantum dot. At sufficiently low temperatures, electron tunneling is blocked by this Coulomb charging energy, leading to the so-called *Coulomb-blockade effect* (CB) [GD92, MF95, KMM⁺97]. Coulomb blockade, however, can be overcome by the gate voltage, or by other excitation mechanisms,

e.g., phonons and photons, inducing *single-electron tunneling* (SET) through discrete quantum states [GD92, MF95, KMM⁺97].

A particularly simple and spectacular example of such a device is the *silicon single-electron transistor*. A silicon single-electron transistor is constructed by connecting a silicon quantum dot to a drain and a source contact via two tunnel barriers [TRH⁺96, GLC97, Til00]. A nearby plunger gate is used to tune the transistor. Using the silicon-on-insulator (SOI) material, sub-10 nm single-electron transistors have been fabricated, operating even at room temperature. Single-electron transistors based on silicon and AlGaAs/GaAs heterostructures have been used as ultra sensitive charge detectors [VLV⁺96, RJSaP98] and single photon detectors [Mat99, KAA⁺00]. The charge sensitivity has been shown to be as low as a few $10^{-5}e/\sqrt{Hz}$. This result is only an order of magnitude away from the theoretical limit of $10^{-6}e/\sqrt{Hz}$. An adiabatic electron pump based on an open quantum dot has been realized as well [SMCG99]. Naturally, single-electron transistors also found applications in metrology [KF99, KEMZ99]. Silicon single-electron transistor might challenge the conventional CMOS devices, since the former can be integrated much more densely and the required technologies are compatible with the existing state-of-the-art.

Studies on the electronic states and the transport properties are of great importance both for the understanding of the physics involved in such small devices and for applications. Quantum dots can be strongly coupled to contacts, leading to a strong hybridization of localized discrete electronic states in the dot with the continuum in the contacts. As a result higher order tunneling becomes important and effects such as the Kondo effect can be observed [GGSM⁺98, SBK⁺99, SFE⁺00]. Recently, semiconductor quantum dots were proposed to be applied to define *quantum bits* (qubits) for quantum computation [Bar95, Lan96, LD98, BRB01]. The essential point is to make a controllable *coherent superposition* of two quantum states ($|1\rangle$ and $|2\rangle$) in semiconductor quantum dots. The quantum states can be the charge states or electron spin states. The superposition of two quantum states can be realized by time-dependent microwave photons [BRB01], which is in analogy to the excitation of hydrogen atoms by laser light:

$$|s\rangle = a(t)|1\rangle + b(t)|2\rangle. \quad (1.1)$$

The qubit can be read out by measuring the tunnel current through the quantum dots [BRB01]. On the other hand, single-electron transistors are proposed for read-out devices for qubits, i.e., the transistor is a charge amplifier operating in the vicinity of the quantum limit [SS97, DS00]. Definitely, read-out devices will induce a collapse of the coherent states. This dephasing effect has been studied both experimentally and theoretically [Gur97, AWM97, BSH⁺98]. On the other hand, since quantum dots are usually fabricated in solid-state host materials, quantum states are naturally coupled to

their thermal and electromagnetic environment, leading to dephasing. Inelastic scattering of electrons by other electrons, phonons, and spin-flip scattering reduces the phase coherence [SIA94, Dat95, AGKL97, Imr97]. In order to realize quantum states with a longer lifetime, the quantum dots have to be isolated from the environment.

The investigation of the dynamics and dephasing of the electronic states in solid-state quantum dots is thus of great importance. By studying the time-dependent properties of quantum dots, the dynamics of electron transport can be obtained. Recently, time-resolved Cooper pair tunneling in coupled Josephson junctions has been studied by Nakamura *et al* [NPT99]. Mooij and van der Wal *et al* have shown the realization of qubits from two macroscopic Josephson persistent-current states [MOL⁺99, vdWtHW⁺00].

In this work, qubits are formed from the bonding and anti-bonding molecular states of a tunnel-coupled double quantum dot at low temperatures. The superposition of two molecular states is realized by applying microwave photons, inducing *Rabi oscillations*. Coherent superpositions are monitored by measuring the induced photon-assisted tunneling (PAT) and tuning the coupling strength between two quantum dots. Superpositions of the ground state and an excited state in single quantum dots are studied as a comparison. Coherent continuous and pulsed microwave sources are applied to reveal the dynamics of single-electron transport.

The thesis is organized as follows:

In **chapter 1**, an introduction to this work and the motivation will be given, followed by two sections on the techniques for fabricating quantum dots from a two-dimensional electron gas (2DEG) of an AlGaAs/GaAs heterostructure and on transport spectroscopy for characterizing quantum dots.

A review of basic theories on electron transport in quantum dots is given in **chapter 2**. In the first section, Coulomb-blockade and single-electron tunneling will be discussed in the classical regime, where the level spectrum is a continuum. Single-electron tunneling through discrete quantum states (of artificial atoms) will be discussed in the second section. The effect of tunnel coupling on transport properties is presented. In the last section the formation of “ionic” and “covalent” molecules from two tunnel-coupled quantum dots will be given.

In the first part of **chapter 3**, a silicon single-electron memory based on Coulomb-blockade and single-electron tunneling in the classical regime at room temperature will be presented. In the second part, the formation of single quantum dots and the characterization by transport spectroscopy will be shown. The formation of “ionic” and “covalent” double-dot molecules will be given in the third part, in which the interaction between the molecular states and acoustic phonons will be addressed as well.

In **chapter 4**, basic theoretical aspects on time-dependent transport through single quantum dots and double quantum dots in the non-adiabatic regime will be considered. Photon-assisted tunneling through single quantum dots (Tien-Gordon picture) and Rabi oscillations between two quantum dots will be discussed.

Experimental studies on photon-assisted tunneling in single quantum dots will be presented in the first part of **chapter 5**. In analogy to real atoms, photo-ionization of single quantum dots is observed, i.e., the ground state of the dot is depopulated by microwave photons and an excited state is then occupied, which is confirmed by probing the tunnel current through the excited state. The dynamics involved in this photo-ionization process is studied in the third part of this chapter, where a new microwave technique is applied to reveal the time-dependent transport. In the second part, coherent superpositions of the bonding and anti-bonding molecular states by microwave photons or by both microwave photons *and* acoustic phonons will be shown. A coherent superposition of photon- and phonon-assisted tunneling is observed in a double quantum dot. In the last part, pulsed microwave radiation is applied to reveal the dynamic charge relaxation processes in a single quantum dot.

The conclusion and outlook will be given in **chapter 6**.

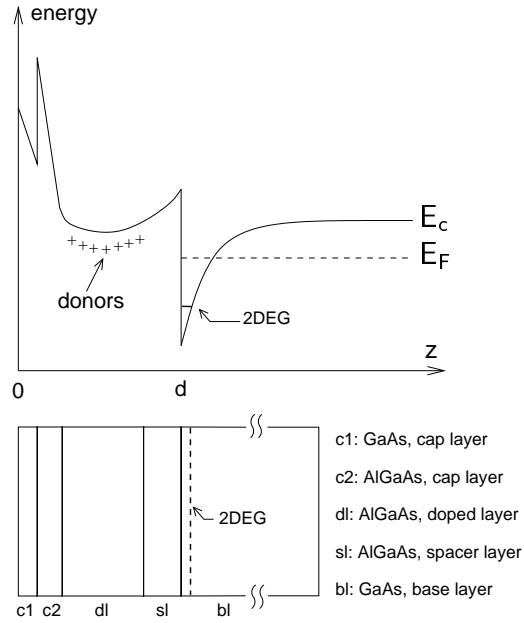


Figure 1.1: The conduction band profile in the direction perpendicular to the surface of a modulation-doped AlGaAs/GaAs heterostructure.

1.1 Quantum Dot Fabrication

The quantum dots studied in this thesis are fabricated by confining a small region of 2DEG from the large area of 2DEG of an AlGaAs/GaAs heterostructure. The band structure of a generic AlGaAs/GaAs heterostructure is shown in Fig. 1.1. The donors in the doped AlGaAs layer provide electrons accumulated in the interfacial potential well, forming an electron channel: A quasi two-dimensional electron gas due to the confinement in the direction perpendicular to the wafer. The spacer layer between the donors and the channel reduces the scattering of electrons in the channel by donors, hence the mobility of electrons in the channel is increased ($\mu_e \sim 8 \times 10^5 \text{ cm}^2/\text{Vs}$). The exact heterostructures used in this work are listed on page 114 in App. A .

Formation of Planar Quantum Dots from 2DEG

For the quasi two-dimensional electron gas with an area of A , continuum energy bands (subbands) are allowed in the plane of 2DEG (x, y). However, there exist discrete energy levels for the electron motion in the direction (z) perpendicular to the plane of

2DEG. The energy levels for the 2DEG have the form of two-dimensional subbands,

$$E = E_{sn} + \frac{\hbar^2}{2m_e^*}(k_x^2 + k_y^2), \quad (1.2)$$

where, E_{sn} is the bottom of each subband due to the confinement in direction z ¹, m_e^* is the effective electron mass, and k_x, k_y are the components of wave vectors in the plane of the 2DEG. The specific spectrum of E_{sn} depends on the details in the confinement potential in direction z . Usually, at low temperatures even the lowest subband (E_{s1}) is not completely occupied and the higher subbands do not participate in transport, which is the case in this thesis.

Including spin degeneracy, the density of states of electrons for the subband (E_{s1}) is a constant

$$D(E) = \frac{Am_e^*}{\pi\hbar^2}. \quad (1.3)$$

Given a sheet electron density of $n_s \sim 2 \times 10^{11} \text{ cm}^{-2}$, the Fermi wavelength is obtained as $\lambda_F = \sqrt{2\pi/n_s} \sim 60 \text{ nm}$.

To define a small quantum dot from the large area of 2DEG, about six main steps are processed. The details can be found on page 111 in App. A. Below, these steps are briefly described: In the first step, a piece of AlGaAs/GaAs heterostructure (about $5 \times 5 \text{ mm}^2$) is cleaved from the wafer and cleaned. In the second step, a mesa of 2DEG is formed by wet etching. The layout of the mesa is transferred from the optical mask to the surface of the heterostructure by optical lithography. The cross-like mesa is $30 \mu\text{m}$ wide and more than 1 mm long (see Fig. A.3 (a)). In the third step, ohmic contacts are defined at the ends of the mesa for probing the current flowing through the device. Again, the pattern transfer is done by optical lithography. In the fourth step, gold contacts are deposited on the surface connecting the large ohmic contacts (later used for connections to the bonding pads on a chip carrier) and the small connection pads (later for connections to the inner nanometer sized Schottky gates). The pattern transfer is done by optical lithography as well. In the fifth step, electron beam lithography is used to pattern the Schottky gates, which are then realized by deposition of gold, as schematically shown in Fig. 1.2 (a) and (b). In the last step, the whole heterostructure with defined circuits is glued into a chip carrier and the circuits are connected to the measurement setup (see Fig. A.3 (b, c)). The sample is then ready for the transport studies at low temperatures.

By applying negative voltages to Schottky gates, the electron gas under the gates are depleted. The outer two pairs of Schottky gates form two quantum point contacts

¹For the quasi 2DEG, the confinement in the direction of z is strong. Electrons behave two-dimensionally as long as the temperature is lower than the distance between neighboring subbands and the confinement potential is high enough so that the lowest unoccupied subband is a bounded state.

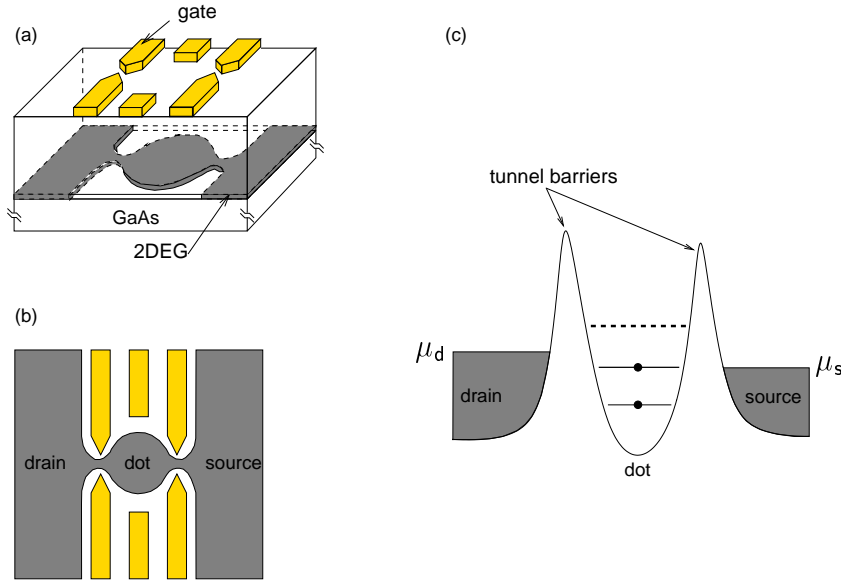


Figure 1.2: (a, b) A planar quantum dot is confined from the large area of 2DEG of an AlGaAs/GaAs heterostructure. The confinement is induced by the negative gate voltage applied to five pairs of Schottky gates on the surface. (c) The schematic energy profile of the confined quantum dot.

(QPCs) separating the central region of 2DEG from the whole 2DEG [vWvHB⁺88]. The two middle gates (plunger gates) further shrink the central region into a small puddle of electrons (see Fig. 1.2 (a) and (b)). When the conductance of the QPC is above $2e^2/h$, there are a few open modes for electron transport and no tunnel barrier is formed, i.e., electrons are not confined. When the conductance of two QPCs becomes lower than $2e^2/h$, tunnel barriers are formed and electrons are confined in the island (see Fig. 1.2 (c)) [BWvKP91]. When the size of the island becomes comparable to the Fermi wavelength, discrete quantum states appear due to the confinement in x - and y -dimension. The energy of electrons is fully quantized and the density of states becomes

$$D(E) \propto \sum_i \delta(E - E_i), \quad (1.4)$$

where E_i is the discrete single-particle states. Hence, this small island of electrons is called a quantum dot and an “artificial atom” [Kas93, HK93, Ash96].

For this kind of planar quantum dots formed by electrostatic confinement potential, the confinement strength in x and y direction is much weaker than that in the z direction. The actual potential is calculated in a self-consistent way [Kum92, Sto96]. For the simplicity, it can be approximated by a parabolic potential or a parabolic potential

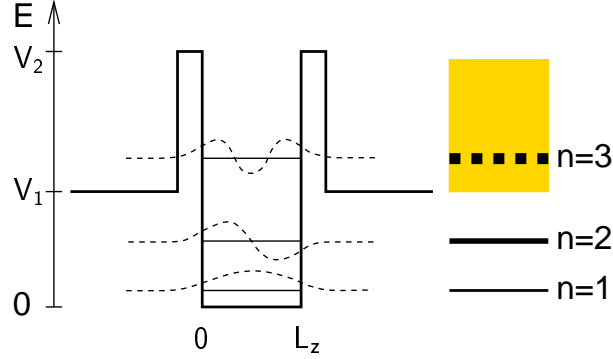


Figure 1.3: A Finite one dimensional potential well. Above energy V_1 , a continuum of energy occurs, in which virtual energy levels exist. The virtual states possess finite lifetimes due to the leakage of wavefunctions out of the potential well.

with a flat bottom [HK93]. The mean level spacing is approximated by $\bar{\Delta} = \pi \hbar^2 / m_e^* A$. The electronic states confined in the quantum dot is schematically shown in Fig. 1.3, where the 3D potential well is illustrated as a 1D square potential well with regular tunnel barriers. Below the energy V_1 , which corresponds to the Fermi levels (μ_d, μ_s) in the drain and source contact (see Fig. 1.2 (c)), there exist discrete stationary quantum states. Above V_1 , a continuum of quantum states begins. Within the continuum, however, there still exist some approximately stationary states. Such a state is also called “virtual energy level”, since it possesses a finite life time:

$$P(t) \propto \exp\left(-\frac{t}{\tau}\right), \quad (1.5)$$

where, $P(t)$ is probability density to find an electron on the virtual state, τ is the mean-life of the virtual state, reflecting the leakage of electrons through the barriers. The life time (τ) is related to the tunneling rate (Γ) at which an electron on the virtual state escapes out of the potential: $\Gamma = 1/\tau$. Obviously, by increasing the width of the tunnel barriers the leakage is less and hence the confined virtual state has a longer life time. In the limit of infinitely wide barriers, the virtual state develops into a stationary state. Comparing to a tunnel barrier formed by a thin layer of isolating materials, the tunnel barriers formed by QPCs are low in energy and wide, as schematically shown in Fig. 1.2 (c). The tunneling rates differ for quantum levels at different energies. However, one of the advantages of this kind of planar quantum dots is that the transparency of barriers can be tuned continuously by gate voltages.

Basic Physical Parameters of Planar AlGaAs/GaAs Quantum Dots

The AlGaAs/GaAs heterostructures used in this thesis are listed on page 114 in App. A. The 2DEG is typically located 40 – 90 nm below the surface. The effective electron mass in the GaAs host crystal is about $m_e^* \approx 0.067m_e$. A typical electron density of $n_e = 2 \times 10^{11} \text{ cm}^{-2}$ is found at a low temperature of 4 K. The corresponding Fermi wavelength is about 60 nm, which is comparable to the dot size. From the electron mobility around $\mu_e \approx 1 \times 10^6 \text{ cm}^2/\text{Vs}$, the mean free path is estimated as $l_f = v_F m_e^* \mu_e / e \approx 10 \text{ } \mu\text{m}$, which is much larger than the dot size. The phase coherence length is usually slightly shorter than the mean free path for a high mobility 2DEG at low temperatures [Dat95]. Given a planar quantum dot with a dot radius of $0.1 \text{ } \mu\text{m}$, the mean level spacing is about $\bar{\Delta} = \hbar^2 / m_e^* r^2 \approx 120 \text{ } \mu\text{eV} \sim 1.3 \text{ K}$. Quantum effects in transport through such small quantum dots are pronounced since the mean level spacing of electronic states can exceed the temperature. Furthermore, the total capacitance $C_\Sigma \approx 8\epsilon_0\epsilon_r r \approx 90 \text{ aF}$ ($\epsilon_r = 12.9$ is the relative static dielectric constant for GaAs) classically describes the ability of containing electrons on the dot. The charging energy of adding an additional electron onto the dot is $E_C = e^2 / C_\Sigma \approx 1.8 \text{ meV}$. At low temperatures ($k_B T \ll E_C$), charge quantization can be observed when the transmission of electrons through the dot is small, i.e., the conductance $G \ll e^2/h$. This charging energy gives rise to the Coulomb-blockade effect, which can be overcome by the gate voltage, the drain-source bias, or the temperature.

1.2 Methods of Characterizing Quantum Dots

Since the transmission of electrons through quantum dots is determined by the overlap of the wave functions in the dots and the leads, the transport studies of quantum dots reveal the electronic structure of quantum dots.

For quantum dots as shown in Fig. 1.2, both direct drain-source current (I_{ds}) and differential conductance ($g = dI_{ds}/dV_{ds}$) can be measured.² This method is usually called *transport spectroscopy*. To measure the differential conductance, a small low frequency³ alternating-current (ac) modulation voltage is added to the direct-current (dc) drain-source bias: $V_{ds} + \tilde{v} \cos(2\pi ft)$ with $e\tilde{v} \ll e|V_{ds}|, \bar{\Delta}, k_B T$, the amplitude of the resulting alternating current is $\tilde{I} \approx \frac{dI_{ds}}{dV_{ds}} \tilde{v} = g\tilde{v}$. By measuring this current using a

²In capacitance spectroscopy, no direct current flows through the quantum dot. However, the detection of capacitance, induced by electrons tunneling between the quantum dots and a contact, gives information on the electronic structure as well.

³Limited by the bandwidth of the cables used, the upper limit for this frequency is about 5 kHz.

lock-in amplifier, the differential conductance $g = dI_{ds}/dV_{ds}$ is obtained. The detailed measurement setup is described on page 117 in App. B

Microwave radiation with the one-photon energy comparable to the mean level spacing is applied to quantum dots, inducing *photon-assisted tunneling* (PAT) through the ground states and excited states. Photon-induced ground (excited) state transitions in the linear regime can be revealed by measuring the photocurrent through the quantum dots. In the nonlinear regime, the resonances are considerably broadened and photon-induced features can not be well resolved.

In addition to the straightforward *microwave spectroscopy* mentioned above, new techniques are developed to obtain more information on the dynamics of electron transport through quantum dots. On page 122 in App. B, two techniques for *heterodyne detection* of photocurrent are described in detail. The basic principle is the following: Two coherent microwave sources with a slight frequency offset (the intermediate frequency) are added to generate a flux of microwave photons whose intensity varies periodically in time with the intermediate frequency. Under the irradiation of such a flux of photons, the resulting alternating photocurrent at the intermediate frequency is solely due to the irradiation, which can be detected using a lock-in amplifier. Furthermore, since microwave sources are coherent, the rigid phase relation determines a constant time base for both the high frequency microwave signal and the intermediate frequency current signal. Hence, the relative phase between the alternating photocurrent and the incident microwave radiation is reliable and can be extracted with a lock-in amplifier. This relative phase reflects the amount of time spent by electrons to tunnel through the quantum dots, i.e., it presents a method to investigate the dynamics of electron transport in quantum dots.

In comparison to the above described technique, where a flux of “monochromatic” microwave photons (i.e., at a single frequency) is generated, another heterodyne detection technique applied in this thesis is termed *broadband microwave spectroscopy*: Two nonlinear transmission lines (NLTLs) are driven by two coherent single microwave sources. The pulsed microwave signals from the NLTLs are then combined to generate a flux of photons in a wide frequency range (20 – 400 GHz). Using a lock-in amplifier, photon-induced tunneling induced by different excitation energies can be detected. Since the heat load induced by broadband radiation is constant, the physical properties of the quantum dots are fairly unchanged when broadband spectroscopy is conducted. The pulsed nature allows to reveal the dynamics of electron transport.

Chapter 2

Coulomb-Blockade Effect and Single-Electron Tunneling: Theory

At low temperatures, when a nanometer sized island (dot) is weakly coupled to the contacts via tunnel barriers, the Coulomb repulsion by electrons on the island affects electron transport. The Coulomb interactions among the electrons on the island can be classically described with a total capacitance C_Σ . This approximation of electron-electron interaction is called the *constant-interaction model*. To add a single electron onto the island, a charging energy of e^2/C_Σ , is required. Hence, the tunneling of electrons onto the island is usually blocked by this so-called *Coulomb-blockade* (CB) energy. The Coulomb-blockade, however, can be eliminated by varying the gate voltage which is applied to the island via the gate capacitance C_g : Electrons are added onto the island one by one at certain gate voltages. The resulting conductance oscillations are called as Coulomb-blockade oscillations, i.e., *single-electron tunneling* (SET) regulated by Coulomb-blockade effect.

To observe Coulomb-blockade, the thermal fluctuation should not overcome the charging energy:

$$k_B T \ll \frac{e^2}{C_\Sigma}. \quad (2.1)$$

Furthermore, the time-averaged fluctuation of electron number on the island must be negligible: $\langle \delta N^2 \rangle \ll 1$, i.e., the average electron number $\langle N \rangle$ is well defined [MF95]. This condition is equivalent to that the time (τ) during which an electron stays on the island should be much larger than quantum uncertainty in this time ($\delta\tau$) [Tho77]: $\tau \gg \delta\tau$. The tunnel current (I) induced by a single-electron tunneling event is about e/τ . The energy uncertainty (δE) is smaller than the applied small bias voltage: $\delta E < eV$. Hence, from $\delta\tau\delta E \geq h$, and $\delta\tau \ll \tau \sim e/I$, the following equivalent condition for

Coulomb-blockade is obtained

$$G = \frac{I}{V} \ll \frac{e^2}{h}. \quad (2.2)$$

Coulomb-blockade oscillations were first observed in metallic grains [GZ68], where the mean level spacing is much smaller than the temperature $\bar{\Delta} \ll k_B T$, i.e., the level spectrum can be treated as a continuum. Hence the transport belongs to the classical regime. For semiconductor quantum dots, since $\bar{\Delta} \gg k_B T$ can be usually fulfilled by reducing the dot size or the temperature. Coulomb-blockade effect in this quantum regime was first observed by Scott-Thomas [STFK⁺89]. Reviews on single-electron tunneling and Coulomb-blockade effect can be found in a few literatures [AL91, GD92, MF95, KMM⁺97].

In this chapter, Coulomb-blockade and single-electron tunneling in metallic island are discussed in Sec. 2.1. In Sec. 2.2, single-electron tunneling in the quantum regime is presented. A tunnel-coupled double quantum dot is studied in Sec. 2.3.

2.1 Metallic Islands

A simple starting point for understanding quantized charge transport is the charging process in a small metallic island (as shown in Fig. 2.1 (a)). The metallic island is coupled to the substrate via a tunnel barrier and is capacitively coupled to a plunger gate. The barrier's conductance is much smaller than e^2/h , i.e., the island is almost isolated from the substrate. Since the mean level spacing is much smaller than the thermal energy, $\bar{\Delta} \ll k_B T$, a number of quantum levels ($k_B T/\bar{\Delta}$) in the island take part in transport. Hence the resonant tunneling of electrons through different states are mixed and the quantum levels in the island can be treated as a continuum.

The tunnel barrier itself is characterized by a capacitance $C \ll e^2/k_B T$ and a resistance of $R \gg (e^2/h)^{-1}$. The classic capacitance C describes the Coulomb repulsion from electrons already on the island. A gate voltage V_g is applied to the island via the gate capacitor C_g (see the equivalent circuit in Fig. 2.1 (b)).

The quantum charge fluctuation on the island is negligible, i.e., the electron number on the island is well defined. Furthermore, the lifetime broadening of quantum levels in the island is much lower than the temperature, $\hbar\Gamma \ll k_B T$. The possibility to find N electrons on the island in equilibrium with the contact (the substrate as shown in Fig. 2.1) is given by the grand canonical distribution function [vHBS92, Bee91]

$$P(N) = \text{const.} \times \exp\left\{-\frac{1}{k_B T}(F(N) - NE_F)\right\}, \quad (2.3)$$

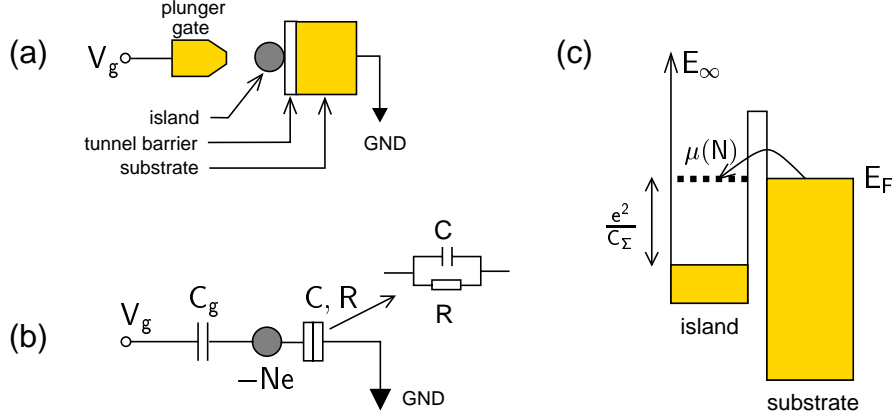


Figure 2.1: (a) A metallic island is connected to an electron reservoir via an ultrasmall tunnel junction (characterized by a capacitance C and a resistance R), and is capacitively coupled to the plunger gate by a gate capacitor C_g . The charge on the island is $Q = -Ne$. (b) The equivalent circuit for the device. (c) The energy landscape of the device. The dashed line indicates the condition of charge fluctuation: $\mu(N) = E_F$.

where, $F(N) = E(N) - TS$ is the free energy and $E(N)$ is the ground state energy of the island. At zero temperature, when both $P(N - 1)$ and $P(N)$ are non-zero, the electron number in the dot fluctuates between $(N - 1)$ and N . To have $P(N - 1) \times P(N) \neq 0$, the following condition must be met:

$$\mu(N) = F(N) - F(N - 1) = E_F, \quad (2.4)$$

where, the chemical potential $\mu(N)$ of the island represents the transition energy between the $(N - 1)$ -electron state and the N -electron state. At zero temperature, the free energy equals the ground state energy of the island. The ground state energy of the island with a charge $Q = -Ne$ is

$$E(N) = \int_0^{-Ne} dQ V_{island},$$

$$V_{island} = \frac{Q}{C_\Sigma} + \frac{C_g}{C_\Sigma} V_g,$$

where, V_{island} is the potential of the island and $C_\Sigma = C_g + C$ is the total capacitance of the island. The ground state energy is written as

$$E(N) = \frac{(Ne)^2}{2C_\Sigma} - Ne \frac{C_g}{C_\Sigma} V_g. \quad (2.5)$$

2. Coulomb-Blockade Effect and Single-Electron Tunneling: Theory

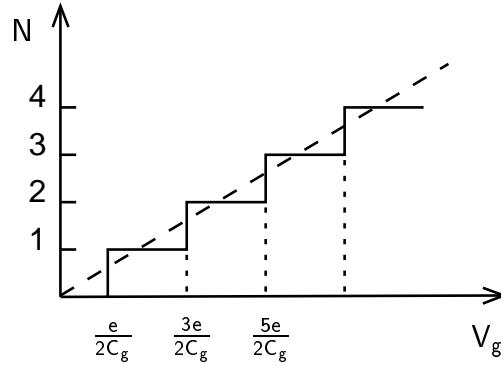


Figure 2.2: Adding single electrons onto the island by increasing the gate voltage ($E_F = 0$ is assumed).

As shown in Eq. 2.5, the gate voltage is an external control on the total electrostatic energy of the island. The energy change induced by a change in gate voltage is evenly distributed to single electrons on the island. The coefficient α , converting the change in gate voltage ΔV_g to the average energy change of a single electron ΔE , is deduced to be

$$\alpha = -\frac{\Delta E}{e\Delta V_g} = -\frac{1}{N} \frac{\partial E(N)}{e\partial V_g} = \frac{C_g}{C_\Sigma}. \quad (2.6)$$

At certain gate voltages, the condition of charge fluctuation (see Eq. 2.4) is fulfilled:

$$\begin{aligned} \mu(N) &= (N - \frac{1}{2}) \frac{e^2}{C_\Sigma} - e\alpha V_g^{\leftrightarrow}(N), \\ &= E_F. \end{aligned}$$

Thus, at a gate voltage of $V_g^{\leftrightarrow}(N) = (N - 1/2)e/C_g - E_F/e\alpha$, the electron number on the island fluctuates between $(N - 1)$ and N . The N -th electron tunnels through the island. As increasing the bias V_g further, single electrons are added onto the island one by one, as shown in Fig. 2.2. The periodicity of gate voltage for adding electrons is

$$\Delta V_g = \frac{e}{C_g}, \quad (2.7)$$

which is determined only by the gate capacitance. In the middle of two neighboring charge-fluctuating points, i.e., $V_g^{\leftrightarrow}(N - 1) = (N - 1)e/C_g - E_F/e\alpha$, no electron tunnels. To charge the N -th electron onto the island, the gate voltage is increased from

$$V_g^{\leftrightarrow}(N - 1) = (N - 1) \frac{e}{C_g} - \frac{E_F}{e\alpha}$$

to

$$V_g^{\leftrightarrow}(N) = N \frac{e}{C_g} - \frac{E_F}{e\alpha}.$$

Accordingly, the average single-electron's energy is changed by

$$\begin{aligned} E_{add} &= E_C \\ &= - \int_{V_g^{\leftrightarrow}(N-1)}^{V_g^{\leftrightarrow}(N)} \frac{1}{N} \frac{\partial E(N)}{\partial V_g} dV_g \\ &= \frac{e^2}{C_\Sigma}. \end{aligned} \quad (2.8)$$

Eq. [2.8] indicates that for adding an extra electron from the contacts to the island this electron has to obtain an addition energy E_C , i.e., the energy of each single electron on the island must be reduced by E_C . The energy E_C is thus called the *charging energy*¹ of the island, which is determined by the total capacitance.

In this device, since electrons fluctuate only between the island and the substrate, no net tunnel current flows through the device. However, the capacitance of the island exhibits oscillations when electrons are added to (removed from) the island. This is what the *capacitance spectroscopy* performs on quantum dots [HIL⁺89, ASW⁺93, DLH⁺94].

2.2 Single Quantum Dots

Both metallic and semiconductor dots can have a small size so that the charging energies become larger than the thermal energy: $E_C \gg k_B T$. For semiconductor quantum dots the mean level spacing $\bar{\Delta}$ is much larger than that of small metallic dots with a similar size. As discussed before, to observe Coulomb-blockade effect, the conductance of the dot should be small ($G \ll e^2/h$), which requires the $h\Gamma \ll k_B T, \bar{\Delta}$. When $h\Gamma \ll k_B T \ll \bar{\Delta}$, Coulomb-blockade oscillations reveal the quantum mechanical coherence in resonant tunneling of electrons through single quantum states. Hence, single-electron tunneling has been used as a method of level spectroscopy in semiconductor quantum dots.

Connected to two contacts (drain and source) via tunnel barriers and capacitively coupled to a plunger gate, a quantum dot forms a *single-electron transistor* based on Coulomb-blockade effect. According to the constant-interaction model, the two tunnel barriers are characterized by capacitances C_L and C_R , respectively, as shown in

¹The charging energy can be obtained as $E_C = \mu(N) - \mu(N-1) = e^2/C_\Sigma$ according to the definition of $\mu(N)$ in Eq. 2.4

Fig. 2.3 (a). The capacitance between the plunger gate and the dot is denoted as C_g . The extra electron number in the dot is N . In such a device, the fluctuation of electrons on the island can be probed by measuring the direct tunnel current (I_{ds}) through the island or the differential conductance ($g = dI_{ds}/dV_{ds}$).

In the following two sections, two regimes are discussed, concerning different coupling strengths between the dot and the contacts. In the weak coupling regime, only the lowest order of tunneling is considered. In the case of strong coupling where the localized electronic states in the dot hybridize with the continuum in the contacts, higher order tunneling processes through virtual states (cotunneling) are enabled.

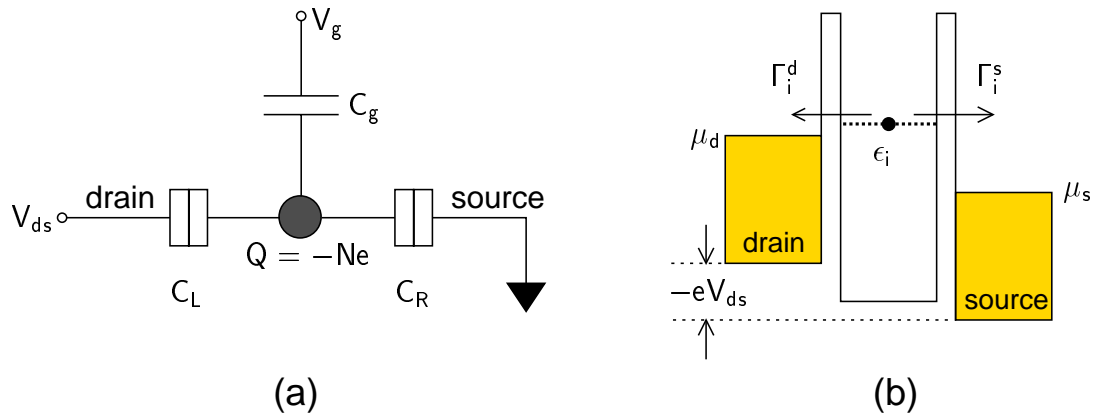


Figure 2.3: (a) A quantum dot is coupled to the drain and source contacts via two tunnel barriers. The drain-source bias V_{ds} shifts the difference in the Fermi energies of both contacts. The gate voltage varies the dot's electrostatic potential. (b) In the resonant tunneling regime with $h\Gamma_i = h(\Gamma_i^d + \Gamma_i^s) \ll k_B T \ll \Delta$, single electrons tunnel through discrete quantum states.

2.2.1 Weak Coupling to Contacts

In the weak coupling regime, the tunneling of electrons between the dot and the contacts are only a negligible perturbation to the ground state energy. The electrostatic energy of the system is described with three parameters: V_{ds} , V_g and N . The Fermi levels of the left (μ_d) and right (μ_s) contacts are related by the drain-source bias:

$$\mu_d - \mu_s = -eV_{ds}. \quad (2.9)$$

The dot's potential V_{dot} can be written as:

$$V_{dot} = \frac{Q}{C_\Sigma} + \frac{C_L}{C_\Sigma} V_{ds} + \frac{C_g}{C_\Sigma} V_g,$$

where, $Q = -Ne$, and $C_\Sigma = C_L + C_R + C_g$ is the total capacitance of the dot. The total electrostatic energy of the system $U(N)$ is then written as

$$\begin{aligned} U(N) &= \int_0^{-Ne} dQ V_{dot}, \\ &= \frac{(Ne)^2}{2C_\Sigma} - Ne [\alpha_d V_{ds} + \alpha V_g], \end{aligned}$$

where, $\alpha_d = C_L/C_\Sigma$ and $\alpha = C_g/C_\Sigma$ are factors of energy-to-voltage, converting the drain-source bias and the gate voltage into the contributed energies of the dot (refer to Eq. 2.6), respectively.

In the model of constant electron-electron interaction, the ground state energy of a quantum dot can be simply written as a sum of the single-particle energy and the electron-electron Coulomb energy:

$$E_{dot}(N) = \sum_{i=1}^N \epsilon_i + U(N), \quad (2.10)$$

where ϵ_i are the single-particle ground state energy of the dot. N electrons are distributed through the discrete quantum levels ϵ_i , $i = 1, 2, 3, \dots$. Each quantum state (ϵ_i) possesses a finite width ($\hbar\Gamma_i$), which is determined by the tunneling rate between the drain (Γ_i^d) and source (Γ_i^s) contact: ($\Gamma_i = \Gamma_i^d + \Gamma_i^s$). The distribution is denoted as $\{n_i\}$, where n_i is either 1 or 0, indicating the i -th level is occupied or empty, respectively.

The possibility of N electrons to remain in the dot in equilibrium with the drain and source contacts is given by the grand canonical distribution function [vHBS92, Bee91]:

$$P(\{n_i\}) = Z^{-1} \exp\left\{-\frac{E_{dot}(N) - N\mu_{d,s}}{k_B T}\right\}, \quad (2.11)$$

where Z is the partition function:

$$Z = \sum_{\{n_i\}} \exp\{-[E_{dot}(N) - N\mu_{d,s}]/k_B T\}. \quad (2.12)$$

At zero temperature, as discussed in Sec. 2.1, charge number fluctuates between ($N - 1$) and N when $\mu(N) = E_{dot}(N) - E_{dot}(N - 1) = \mu_{d,s}$, i.e.,

$$\epsilon_N + \left(N - \frac{1}{2}\right) \frac{e^2}{C_\Sigma} - e \left\{ (\alpha_d - 1) V_{ds} + \alpha V_{gd}^{\leftrightarrow}(N) \right\} = \mu_s, \quad (2.13)$$

$$\epsilon_N + \left(N - \frac{1}{2}\right) \frac{e^2}{C_\Sigma} - e \left\{ \alpha_d V_{ds} + \alpha V_{gs}^{\leftrightarrow}(N) \right\} = \mu_s, \quad (2.14)$$

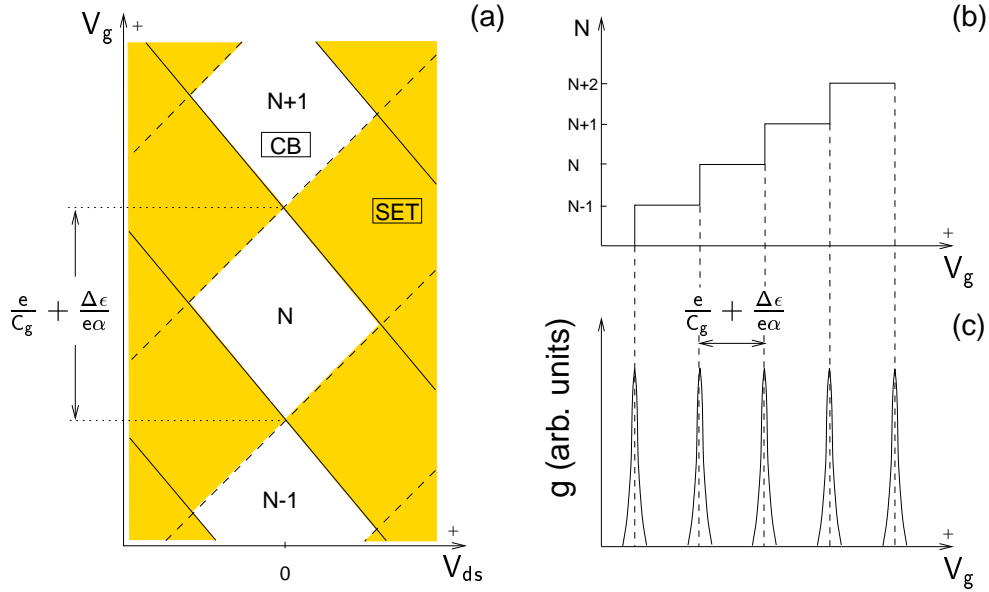


Figure 2.4: (a) CB diamonds revealed by plotting the dot's conductance (g) in the $V_{ds} - V_g$ plane (dark: $g > 0$, white: $g = 0$). The solid (dashed) lines represent the tunneling of electrons between the source (drain) contact and the dot. Within the diamonds, the number of electrons in the dot is fixed at $N, N - 1$, etc. (b) At zero drain-source bias, the electron number is increased one by one by increasing the gate voltage in steps of $e/C_g + \Delta\epsilon/e\alpha$ (see details in text). (c) The dot's conductance shows oscillations as a function of the gate voltage. The finite peak width stems from both the finite lifetime and the temperature.

where ϵ_N is the ground state energy of the quantum dot containing N electrons.²

Eq. 2.13 (Eq. 2.14) corresponds to the charge fluctuation between the drain (source) contact and the dot. Eq. 2.13 and Eq. 2.14 can be rearranged in the following format

$$V_{gd}^{\leftrightarrow}(N) = \left(N - \frac{1}{2}\right) \frac{e}{C_g} + \frac{(C_\Sigma - C_L)}{C_g} V_{ds} + \frac{\epsilon_N - \mu_s}{e\alpha}, \quad (2.15)$$

$$V_{gs}^{\leftrightarrow}(N) = \left(N - \frac{1}{2}\right) \frac{e}{C_g} - \frac{C_L}{C_g} V_{ds} + \frac{\epsilon_N - \mu_s}{e\alpha}. \quad (2.16)$$

At $V_{gd}^{\leftrightarrow}(N)$ and $V_{gs}^{\leftrightarrow}(N)$, the quantum state ϵ_N is “aligned” with the Fermi levels in the drain and source contact³, respectively. Accordingly, the above two conditions stand

²In the constant-interaction model, the ground state does not directly depend on the gate voltage. In the reality, the gate voltage will change the dot shape and hence the ground states. This was observed in the statistic properties of peak spacing in the CB regime [SBA⁺96, SHW97, PCS⁺98, Alh00].

³In fact, it is the renormalized quantum level ϵ_N according to Eqs. [2.13, 2.14] that matches the Fermi levels. For simplicity, the term “quantum state ϵ_N ” is used in this thesis instead of the renormalized quantum state when it is speaking about the level alignment.

for the drain- and source-related resonance (tunneling). $V_{gd}^{\leftrightarrow}(N)$ differs from $V_{gs}^{\leftrightarrow}(N)$ only when a non-zero V_{ds} is applied. At $V_{ds} = 0$, the distance between two neighboring peaks is

$$\Delta V_g = \frac{e}{C_g} + \frac{1}{e\alpha}(\epsilon_{N+1} - \epsilon_N), \quad (2.17)$$

where, ϵ_{N+1} and ϵ_N are the ground state with $(N + 1)$ and N electrons in the dot, respectively.

By mapping the condition of electron tunneling specified by Eq. [2.15] and Eq. [2.16] in the $V_{ds} - V_g$ plane, Coulomb-blockade diamonds are obtained, as shown in Fig. 2.4 (a). The solid lines (boundaries) mark the source-related tunneling, and the dashed lines for the drain-related tunneling. The corresponding slopes of these drain- and source-related boundaries ($s = \partial V_g / \partial V_{ds}$) are

$$s_1 = \frac{C_\Sigma - C_L}{C_g} = 1 + \frac{C_R}{C_g} > 1, \quad (2.18)$$

$$s_2 = -\frac{C_L}{C_g} < 0. \quad (2.19)$$

Similar to the device discussed in Sec. 2.1, the voltage-to-energy coefficient (α) of the plunger gate has the same form as Eq. 2.6, and the charging energy is the same as defined in Eq. 2.8:

$$\alpha = \frac{C_g}{C_\Sigma} = \frac{1}{|s_1| + |s_2|}, \quad (2.20)$$

$$E_C = \frac{e^2}{C_\Sigma}.$$

However, the addition energy required for adding an additional electron to the dot includes the single-particle energy:

$$E_{add} = E_C + (\epsilon_{N+1} - \epsilon_N). \quad (2.21)$$

In this thesis, no exact relation between the ground state energy and the electron number is known. Approximately, $(\epsilon_{N+1} - \epsilon_N)$ will be taken as the excitation energy of the lowest excited state of the dot containing N electrons or roughly as the mean level spacing $\bar{\Delta}$.

Linear transport regime

According to the work by Beenakker *et al* [Bee91], in the linear transport regime, i.e., $eV_{ds} \approx 0$, the conductance of a quantum dot is given as

$$g = \frac{e^2}{k_B T} \sum_{i=1}^{\infty} \sum_{N=1}^{\infty} \frac{\Gamma_i^d \Gamma_i^s}{\Gamma_i^d + \Gamma_i^s} \times$$

$$P_{eq}(N, n_i = 1) \left\{ 1 - f(\epsilon_i + U(N) - U(N-1) - \mu_{d,s}) \right\}, \quad (2.22)$$

where $P_{eq}(N, n_i = 1)$ is the joint probability that the dot contains N electrons and the i -th quantum level is occupied, and the Fermi-Dirac distribution

$$f(\epsilon_i + U(N) - U(N-1) - \mu_{d,s}) = \left\{ 1 + \exp \left[\frac{\epsilon_i + U(N) - U(N-1) - \mu_{d,s}}{k_B T} \right] \right\}^{-1} \quad (2.23)$$

is the probability of occupied states in the drain or source contacts. Eq. 2.22 is a sum of the contributions to conductance from all tunneling processes with different statistical weights, which correspond to different level configurations with N electrons on the dot at finite temperatures. Clearly, Eq. 2.22 is temperature-dependent.

At low temperatures, where $h\Gamma \ll k_B T \ll \bar{\Delta}$, E_C , only tunneling through one quantum state (ϵ_i), which is the closest to the Fermi levels, contributes to the dot's conductance at near-zero bias. The conductance of a quantum dot in this linear transport regime is given by

$$g = \frac{e^2}{4k_B T} \frac{\Gamma_i^d \Gamma_i^s}{\Gamma_i^d + \Gamma_i^s} \cosh^{-2} \left\{ \frac{-e\alpha[V_g - V_g^{\leftrightarrow}(N)]}{2k_B T} \right\}, \quad (2.24)$$

where $V_g^{\leftrightarrow}(N)$, standing for the gate voltage at which the tunneling of the N -th electron occurs, is determined by Eq. 2.15 or Eq. 2.16 with $V_{ds} = 0$. The conductance peak has a full-width-at-half-maximum of the gate voltage as

$$\text{FWHM} = \frac{3.52k_B T}{e\alpha}, \quad (2.25)$$

indicating that the electron transport is thermally broadened.

As increasing the tunneling rates through the barriers, the lifetime of a quantum state becomes shorter, i.e., the intrinsic level width of the state gets larger. When $\bar{\Delta} \gg h\Gamma \gg k_B T$, the broadening of a conductance peak is dominated by the lifetime of the involved quantum state but not by the temperature. However, in this regime the discreteness of quantum states are still resolvable since both $h\Gamma$ and $k_B T$ are smaller than $\bar{\Delta}$. The transmission probability through one quantum level of the dot has the Breit-Wigner form

$$T(V_g) \propto \frac{h\Gamma_i/2}{(h\Gamma_i/2)^2 + \left\{ e\alpha[V_g - V_g^{\leftrightarrow}(N)] \right\}^2}. \quad (2.26)$$

The full-width-at-half-maximum of the conductance peak is thus

$$\text{FWHM} = \frac{h\Gamma_i}{e\alpha}, \quad (2.27)$$

In this regime, the broadening of the conductance peak also reflects the contribution of inelastic scattering of electrons, e.g., inelastic scattering by other electrons, phonons or photons. The peak height of resonant tunneling in this regime will be reduced by inelastic scattering.

In the regime where the lifetime broadening and temperature broadening are comparable in magnitude ($\hbar\Gamma \sim k_B T$), the total width of the conductance peak shows a combination of both mechanisms, which can be approximated as [GGGK⁺98]

$$\text{FWHM} \approx \frac{0.78\hbar\Gamma_i + 3.52k_B T}{e\alpha}. \quad (2.28)$$

The conductance peak has a temperature broadened Breit-Wigner form [FMM⁺93, GGGK⁺98].

Nonlinear transport regime

In the linear transport regime where $e|V_{ds}| < \bar{\Delta}$, electrons can tunnel only through the lowest unoccupied state. Hence, Coulomb-blockade oscillations in the linear regime resulted from adding or removing electrons reveal the so-called *addition spectrum*. A finite drain-source bias opens up the transport window between the Fermi levels in the drain and source contacts: $-eV_{ds} = \mu_d - \mu_s$. As $|V_{ds}|$ increases and $e|V_{ds}| > \bar{\Delta}$, excited states can be aligned with the Fermi levels and contribute to transport. Hence, the tunneling of electrons in the nonlinear regime provides the *excitation spectrum* of the quantum dot. As shown in Fig. 2.5, tunneling through excited states are revealed in the SET regime. In the figure, $E_0(N-1)$, $E_0(N)$, and $E_0(N+1)$ represent the ground state energy of the quantum dot containing $N-1$, N , and $N+1$ electrons, respectively. $E_1(N)$ and $E_2(N)$ are the first and second excited state of the dot with N electrons. Similarly, $E_1(N+1)$ and $E_2(N+1)$ are the first and second excited state of the dot with $N+1$ electrons.

In the nonlinear transport regime, new channels induced by inelastic processes contribute to transport through the quantum dot as well. Different to the elastic processes, inelastic channels have different decay partial width Γ_{in} . The presence of inelastic processes modify the pure coherent tunneling. When $\Gamma_{in} \ll \Gamma$, electron transport is coherent resonant tunneling. While when $\Gamma_{in} \gg \Gamma$, the transport turns out to be sequential. Strong inelastic tunneling in the SET regime would mask resonant tunneling through excited states. The total tunnel current is a sum of all possible transitions which have different contributions since the tunneling rates are different for different channels.

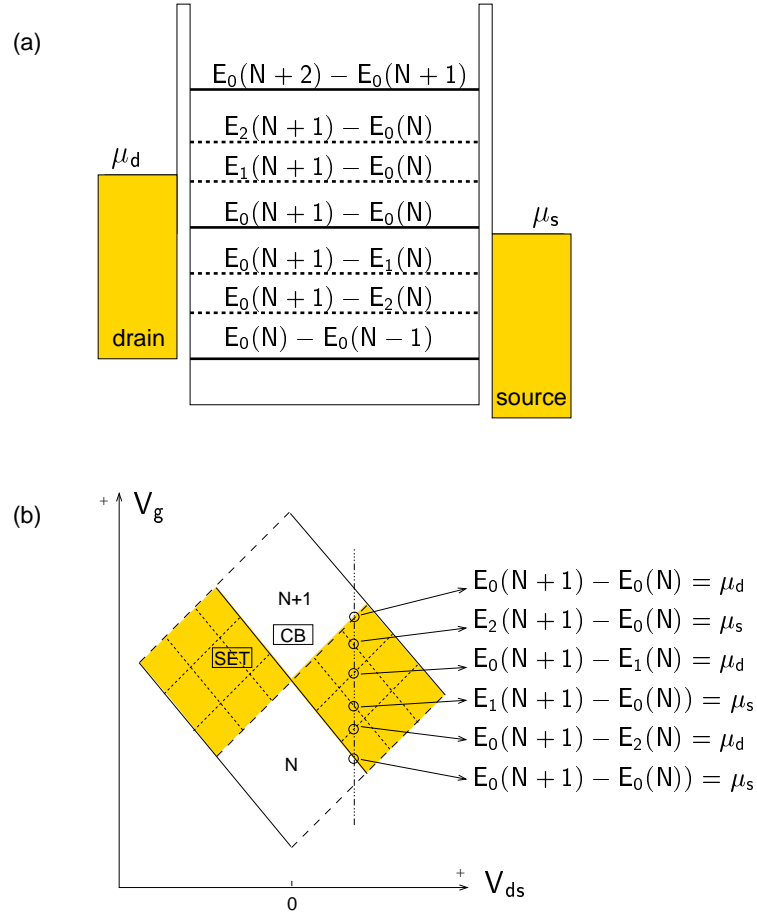


Figure 2.5: (a) Chemical potentials of the dot correspond to different transitions. (b) Coulomb-blockade diamonds reveal CB (white) and SET (dark) regimes. In SET regimes, tunneling through excited states is illustrated as dotted lines. For those dotted lines parallel to the dashed (solid) boundaries of CB diamonds, the dot's chemical potential is matched with μ_d (μ_s), i.e., drain- (source-) related resonance. At a positive drain-source bias marked by a vertical dash-dotted line, six resonances are related to different transitions as shown in (a).

2.2.2 Strong Coupling to Contacts

In CB regimes, even when the dot-contact coupling is weak ($\hbar\Gamma \ll k_B T$) there is small charge fluctuation of the number of electrons on the dot, which corresponds to the process in which electrons momentarily tunnel onto the dot with an energy deficit on the scale of the Coulomb charging energy [GM90, AN90, ZS91, AN92, MF95]. Electrons involved in this process stay on a virtual quantum state for a sufficiently short interval so that the energy uncertainty of this state is larger than the charging energy and hence the whole tunneling process can be realized. This tunneling process is the

so-called *cotunneling* [AN90, AN92, GM90], which induces off-resonance tunneling in CB regimes. With stronger tunnel coupling with contacts, but $\hbar\Gamma \ll k_B T$ still holds, cotunneling in CB regimes can be enhanced.

This cotunneling process has been studied using perturbation theories by taking into account the finite tunneling strength between the dot and the contacts. The first order is zero due to the Coulomb-blockade effect. The second order is the leading effect, which leads to two distinct types of cotunneling: *elastic cotunneling* and *inelastic cotunneling* [GM90, AN90]. In elastic cotunneling, an electron tunnels from one of the contacts onto the dot and out of the dot through the same intermediate state of the dot. In this process, the state of the quantum dot is unchanged and the cotunneling current is linear with the drain-source bias. In inelastic cotunneling, an electron that tunnels from one of the contacts into a state of the dot is followed by an electron in another state of the dot tunnels into the other contact. In this process, the dot state is changed inducing an electron-hole excitation in the dot and the cotunneling current is nonlinear with the drain-source bias.

When $k_B T < \sqrt{E_C \bar{\Delta}}$ and $eV_{ds} < \bar{\Delta}$, elastic cotunneling dominates. For small quantum dots, when electrons can traverse the dot much faster than the time spent in the virtual state ($\sim \hbar/E_C$), i.e., electrons can go through a virtual state of the dot, the off-resonance current induced by elastic cotunneling is found [AN90, AN92]

$$I_{ds}^{el-co} = \frac{\hbar G_L G_R \bar{\Delta}}{4\pi e^2} \left\{ \frac{1}{E_1} + \frac{1}{E_2} \right\} V_{ds}, \quad (2.29)$$

where E_1 (E_2) corresponds to the energy associated with adding (removing) an electron to (from) the dot. It is clear that the sum of E_1 and E_2 approximates the charging energy: $E_1 + E_2 = E_{add} \approx E_C$. G_L and G_R are the independent conductances of the left and right tunnel barriers, respectively.

When $k_B T > \bar{\Delta}$ or $e|V_{ds}| > \bar{\Delta}$, inelastic cotunneling prevails. The current induced by inelastic cotunneling can be written as [AN90, AN92]

$$I_{ds}^{in-co} = \frac{\hbar G_L G_R}{12\pi e^2} \left(\frac{1}{E_1} + \frac{1}{E_2} \right)^2 \left\{ (eV_{ds})^2 + (2\pi k_B T)^2 \right\} V_{ds}. \quad (2.30)$$

Inelastic cotunneling strongly depends on the temperature and the applied bias, which increase the number of possible electron-hole excitations in the dot for the realization of inelastic cotunneling processes. Both elastic and inelastic cotunneling current are proportional to $G_L G_R$. This is a characteristic of an off-resonance tunneling process.

2.3 Coupled Double Quantum Dots

Single quantum dots can be viewed as artificial atoms [Kas93, HK93, Ash96], then coupled quantum dots can be treated as artificial molecules [Kou95, BHvKE96]. Two

quantum dots can be coupled to each other electrostatically and quantum mechanically. Both electrostatic coupling and tunnel coupling between the dots determine the charge configuration, electronic states, and electron transport in coupled dots. In the former case, the inter-dot interaction concerned is mainly the electrostatic energy which is characterized by inter-dot capacitance. Electrons are localized in each dot and the electron number on each dot is well defined. Given the quantum mechanical coupling, electrons can tunnel from dot to dot. The inter-dot tunnel conductance can be comparable to or even larger than $2e^2/h$. Electrons are delocalized throughout the whole structure by tunneling, i.e., electron number on each dot will fluctuates. Nonetheless, the total electron number can be preserved when the double dot is weakly connected to the contacts. The modification of electronic states due to the tunnel coupling between the dots is analogous to the chemical bonding between real atoms.

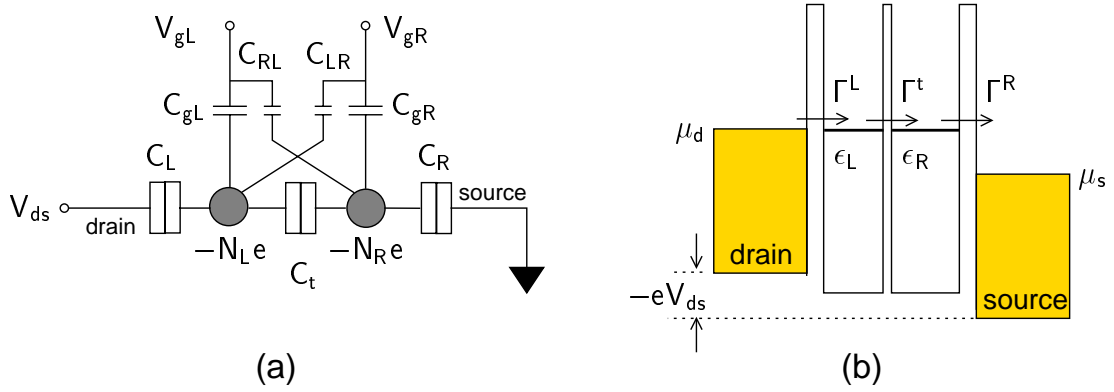


Figure 2.6: (a) The equivalent circuit of a coupled double dot according to the constant-interaction model. (b) The level diagram for the coupled double dot in the quantum regime where discrete levels are resolved at low temperatures ($\hbar\Gamma^L, \hbar\Gamma^R, \hbar\Gamma^t \ll k_B T \ll \bar{\Delta} \ll E_C$).

In this thesis, only coupled double quantum dot realized in the 2DEG of an Al-GaAsAs/GaAs heterostructure is discussed. Two single quantum dots are coupled by a tunnel barrier. Connected to the drain and source contacts by two tunnel barriers, the double dot allows to probe the tunnel current, as shown in the equivalent circuit in Fig. 2.6 (a). These tunnel barriers can be tuned by the respective gate voltages. In this thesis, dot-contact couplings are restricted to be weak, i.e., the double dot is almost isolated from the contacts and hence the finite width of the quantum states of the dots can be reduced. Furthermore, the drain-source bias is set to be small so that only two ground states (one in each dot) participate in transport, as shown in the level diagram in Fig. 2.6 (b). The potentials of the dots and hence the quantum states of the dots can be tuned by respective plunger gate voltages, i.e., V_{gL} (V_{gR}) for the left (right) dot, as shown in Fig. 2.6 (a). The detuning between these two quantum states and the population of single electrons in the double dot can be well controlled by these two plunger

gate voltages. The double quantum dot can be tuned to be “ionic” (“covalent”), i.e., a single electron is localized (populated) between two dots. As well controlled two-level systems, double quantum dots are proposed as quantum bits (qubits) for computation [LD98] and as quantum noise detectors [AK00]. For both applications, electron dynamics and interactions with environment are of great importance.

Since two dots are weakly coupled to the contacts, the dot-contact tunneling and the induced change in contacts and dots can be neglected. The electron-electron interactions is described by relevant capacitances according to the constant-interaction model. The tunneling between the dots is included additionally when the dots are strongly coupled to each other. The Hamiltonian of the double dot with $Q_L = -N_L e$ and $Q_R = -N_R e$ on the left and right dot respectively can be written as [Pfa98, RCU96]

$$H = H_L + H_R + H_T + H_C, \quad (2.31)$$

where, H_L and H_R stand for the Hamiltonians for the left and right dot excluding the inter-dot electrostatic interaction (H_C), respectively. H_T is the Hamiltonian describing the inter-dot tunneling. The detailed H_L , H_R , H_T , and H_C are

$$H_L = \sum_{i \in L} \left\{ \epsilon_{Li} - e(\gamma_{dL} V_{ds} + \gamma_{gL} V_{gL} + \gamma_{LR} V_{gR}) \right\} d_{Li}^\dagger d_{Li} + \hat{N}_L^2 \frac{e^2}{C_{\Sigma L}} \quad (2.32)$$

$$H_R = \sum_{j \in R} \left\{ \epsilon_{Rj} - e(\gamma_{dR} V_{ds} + \gamma_{RL} V_{gL} + \gamma_{gR} V_{gR}) \right\} d_{Rj}^\dagger d_{Rj} + \hat{N}_R^2 \frac{e^2}{C_{\Sigma R}} \quad (2.33)$$

$$H_C = e^2 \hat{N}_L \hat{N}_R \left\{ \frac{\gamma_{QL}}{C_{\Sigma L}} + \frac{\gamma_{QR}}{C_{\Sigma R}} \right\},$$

$$H_T = \sum_{i, i' \in L; j, j' \in R} t_{ij} d_{Li}^\dagger d_{Rj} + H.c., \quad (2.34)$$

where, ϵ_{Li} and ϵ_{Rj} are quantum states in the left and right dot, respectively. Accordingly, the electron number operators are $\hat{N}_L = \sum_i d_{Li}^\dagger d_{Li}$ and $\hat{N}_R = \sum_j d_{Rj}^\dagger d_{Rj}$. The factors γ_{dL} and γ_{dR} describe the influence of V_{ds} on the potentials of the left and right dot. Similarly, γ_{gL} and γ_{gR} stand for the influences from the left and right gate voltages. The coefficients γ_{LR} and γ_{RL} represent the influence of the right gate voltage to the left dot and the influence of the left gate voltage to the right dot, respectively. In the experiments, this kind of crosstalk between gate voltages usually exists. γ_{QL} and γ_{QR} describes the mutual electrostatic interaction between two dots. It is clear that $\gamma_{QL}/C_{\Sigma L}$ equals to $\gamma_{QR}/C_{\Sigma R}$. The above factors are determined by capacitances shown in Fig. 2.6 (a), whose explicit expressions are listed on page 123 in App. C.

2.3.1 Weak Coupling between the Dots

In the weak tunnel coupling regime, H_T is negligible comparing to the electrostatic energy between the dots. The ground state energy can be written as

$$E(N_L, N_R) = E_L + E_R + E_{L\leftrightarrow R}, \quad (2.35)$$

where, E_L , E_R , and $E_{L\leftrightarrow R}$ represent the energies for the left dot, the right dot and the inter-dot electrostatic energy, respectively. They are expressed in detail:

$$\begin{aligned} E_L &= \sum_{i=1}^{N_L} \epsilon_{Li} + \frac{Q_L^2}{2C_{\Sigma L}} + (\gamma_{dL}V_{ds} + \gamma_{gL}V_{gL} + \gamma_{LR}V_{gR})Q_L, \\ E_R &= \sum_{j=1}^{N_R} \epsilon_{Rj} + \frac{Q_R^2}{2C_{\Sigma R}} + (\gamma_{dR}V_{ds} + \gamma_{RL}V_{gL} + \gamma_{gR}V_{gR})Q_R, \\ E_{L\leftrightarrow R} &= \left[\frac{\gamma_{QL}}{C_{\Sigma L}} + \frac{\gamma_{QR}}{C_{\Sigma R}} \right] Q_L Q_R. \end{aligned}$$

Following the same procedure as described in Sec. 2.2, the conditions for charge transport under finite drain-source bias ($-eV_{ds} = \mu_d - \mu_s$) are

$$\mu_L(N_L, N_R) = E(N_L, N_R) - E(N_L - 1, N_R) = \mu_d; \quad (2.36)$$

$$\begin{aligned} \mu_{LR}(N_L, N_R) &= \mu_L(N_L, N_R) - \mu_R(N_L, N_R) \\ &= E(N_L, N_R - 1) - E(N_L - 1, N_R) = 0, \end{aligned} \quad (2.37)$$

or

$$\mu_R(N_L, N_R) = E(N_L, N_R) - E(N_L, N_R - 1) = \mu_s; \quad (2.38)$$

$$\begin{aligned} \mu_{LR}(N_L, N_R) &= \mu_L(N_L, N_R) - \mu_R(N_L, N_R) \\ &= E(N_L, N_R - 1) - E(N_L - 1, N_R) = 0. \end{aligned} \quad (2.39)$$

In the above equations, $\mu_L(N_L, N_R)$ and $\mu_R(N_L, N_R)$ represent the chemical potentials of the left and right dot, determining the energy levels at which the N_L -th (N_R -th) electron tunnel between the left (right) dot and the drain (source) contact. $\mu_{LR}(N_L, N_R)$ is the difference between $\mu_L(N_L, N_R)$ and $\mu_R(N_L, N_R)$. $\mu_{LR}(N_L, N_R) = 0$ indicates that a single electron fluctuates between the dots: $(N_L, N_R - 1) \leftrightarrow (N_L - 1, N_R)$.

Eq. [2.36] and Eq. [2.37] follow that the charge fluctuation between the drain and the left dot, and between the left and the right dot, respectively. This situation is illustrated in the level diagram shown in Fig. 2.6 (b), which can be termed as drain-related resonance. Eq. [2.38] and Eq. [2.39] represent the charge fluctuation between the right dot and the source contact and between the dots, respectively. Accordingly,

these conditions are for the source-related resonance. Both the drain- and source-related resonances induce finite tunneling through the double dot.

In the linear transport regime ($V_{ds} = 0$, $\mu_d = \mu_s$), the above two conditions are unified. The conditions can be rewritten as following

$$\begin{aligned}\mu_L &= \epsilon_L + (N_L - \frac{1}{2})\frac{e^2}{C_{\Sigma L}} + \left[\frac{\gamma_{QL}}{C_{\Sigma L}} + \frac{\gamma_{QR}}{C_{\Sigma R}}\right]e^2 N_R - e(\gamma_{gL}V_{gL} + \gamma_{LR}V_{gR}) \\ &= \mu_d,\end{aligned}\tag{2.40}$$

$$\begin{aligned}\mu_R &= \epsilon_R + (N_R - \frac{1}{2})\frac{e^2}{C_{\Sigma R}} + \left[\frac{\gamma_{QL}}{C_{\Sigma L}} + \frac{\gamma_{QR}}{C_{\Sigma R}}\right]e^2 N_L - (\gamma_{RL}V_{gL} + \gamma_{gR}V_{gR}) \\ &= \mu_s.\end{aligned}\tag{2.41}$$

The above two conditions mapped in the $V_{gR} - V_{gL}$ plane yield a hexagonal charging diagram [LCW⁺96, BHvKE96, FT97], as shown in Fig. 2.7. In the charging diagram, the boundaries (dashed lines) labeled as BL and BR are determined by Eq. [2.40] and Eq. [2.41], respectively. The dotted lines correspond to Eq. [2.37] and Eq. [2.39]. Only both conditions described by Eq. [2.40] and Eq. [2.41] are fulfilled, i.e., at the crossing points (p1 and p2) of the line BL and BR in Fig. 2.7, transport through the double dot is enabled. Along the boundaries tunnel current can be suppressed in a sufficiently weakly coupled double dot since the two quantum states (ϵ_L and ϵ_R) are mismatched and their wavefunctions are localized in the respective quantum dot⁴.

The slopes for boundaries BL and BR are

$$\begin{aligned}k_{BL} &= -\gamma_{LR}/\gamma_{gL}, \\ k_{BR} &= -\gamma_{gR}/\gamma_{RL}.\end{aligned}$$

Given the crosstalk between the dots is zero, the boundary BL and BR become parallel with the axis of V_{gR} and V_{gL} , respectively. As shown in Fig. 2.7, the direction \mathbf{A} , determined by connecting the crossing points p1 and p2, has a slope of

$$k_A = \frac{\gamma_{gR} - \gamma_{LR}}{\gamma_{gL} - \gamma_{RL}}.\tag{2.42}$$

The distance in V_{gL} between two successive boundaries (BL), which can be obtained from the charging diagram (as shown in Fig. 2.7), is

$$\begin{aligned}\Delta V_{gL} &= \frac{\Delta\epsilon_L + e^2/C_{\Sigma L}}{e\gamma_{gL}}, \\ &= \frac{E_{addL}}{e\gamma_{gL}}.\end{aligned}\tag{2.43}$$

⁴Again, for the simplicity, ϵ_L and ϵ_R are used instead of μ_L and μ_R defined in Eq. [2.40, 2.41]

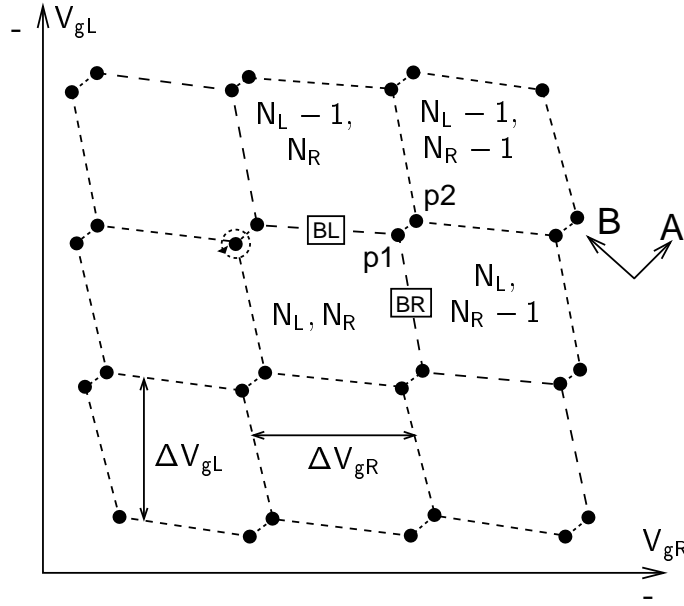


Figure 2.7: A charging diagram of a weakly tunnel-coupled double quantum dot.

Similarly, the distance in V_{gR} between two neighboring boundaries (BR) is

$$\begin{aligned}\Delta V_{gR} &= \frac{\Delta\epsilon_R + e^2/C_{\Sigma R}}{e\gamma_{gR}}, \\ &= \frac{E_{addR}}{e\gamma_{gR}}.\end{aligned}\quad (2.44)$$

Clearly, the peak spacing ΔV_{gL} (ΔV_{gR}) depends on the charging energy and the ground state energies of the left (right) dot.

Away from the crossing points, the number of electrons on the dots can be taken as constant. The variations of the gate voltages shift the potentials. Two energy variables are important in understanding the role of the two plunger gates: The average ($\bar{\mu} = (\mu_L(N_L, N_R) + \mu_R(N_L, N_R))/2$) of and the difference ($\mu_{LR} = \mu_L(N_L, N_R) - \mu_R(N_L, N_R)$) between the chemical potentials of the left and right dot. According to Eq. 2.40 and Eq. 2.41, the change in the average of and the difference of μ_L and μ_R can be expressed as

$$\delta\bar{\mu} = -\frac{1}{2}\left[e(\gamma_{gL} + \gamma_{RL})\delta V_{gL} + e(\gamma_{gR} + \gamma_{LR})\delta V_{gR}\right], \quad (2.45)$$

$$\delta\mu_{LR} = -e(\gamma_{gL} - \gamma_{RL})\delta V_{gL} + e(\gamma_{gR} - \gamma_{LR})\delta V_{gR}, \quad (2.46)$$

$$= -e\alpha_L\delta V_{gL} + e\alpha_R\delta V_{gR}. \quad (2.47)$$

Using the factors α_L and α_R defined in Eq. [2.47], the relative difference between μ_L and μ_R can be easily obtained. In the direction of **A** (see Eq. [2.42]), the relative

difference between the chemical potentials is constant since $\delta\mu_{LR} \equiv 0$. In the level diagram as shown in Fig. 2.6 (b), this characteristic can be illustrated in the following way: By shifting both the gate voltages (V_{gL} and V_{gR}) near one of the crossing points in the direction **A**, the levels ϵ_L and ϵ_R are lifted or lowered by the same amount of energy. On the other hand, there exists a direction **B**, along which $\delta\bar{\mu} \equiv 0$. Direction **B** has a slope of

$$k_B = -\frac{\gamma_{gR} + \gamma_{LR}}{\gamma_{gL} + \gamma_{RL}}. \quad (2.48)$$

Usually, direction **B** is not perpendicular to direction **A** since

$$k_A \times k_B = -\frac{\gamma_{gR}^2 - \gamma_{LR}^2}{\gamma_{gL}^2 - \gamma_{RL}^2} \neq -1 \quad (2.49)$$

The separation of p1 from p2 is a result of the Coulomb interaction between the charges on the two dots. The differences in gate voltages between the neighboring p1 and p2 are

$$\Delta V_{gL}^{p1p2} = \frac{\gamma_{gR} - \gamma_{LR}}{\gamma_{gL}\gamma_{gR} - \gamma_{RL}\gamma_{LR}} \frac{2eC_t}{C_{\Sigma L}C_{\Sigma R}}, \quad (2.50)$$

$$\Delta V_{gR}^{p1p2} = \frac{\gamma_{gL} - \gamma_{RL}}{\gamma_{gL}\gamma_{gR} - \gamma_{RL}\gamma_{LR}} \frac{2eC_t}{C_{\Sigma L}C_{\Sigma R}}, \quad (2.51)$$

which are proportional to the inter-dot capacitance C_t . From p1 to p2, both chemical potentials on the left and right dot are lifted by an amount of

$$E_{el} = \frac{2e^2C_t}{C_{\Sigma L}C_{\Sigma R}}. \quad (2.52)$$

E_{el} is termed *inter-dot charging energy*.

2.3.2 Strong Coupling between the Dots

As the tunnel coupling is increased so that H_T in Eq. [2.31] is not negligibly small, inter-dot tunneling induces charge fluctuation between the dots. The inter-dot coupling can be described with a tunneling rate Γ^t , as shown in Fig. 2.6. It is related to a tunneling matrix element $t = \hbar\Gamma^t$. With an inter-dot tunnel coupling not too strong so that Coulomb-blockade still prevails, i.e., $t \ll e^2/C_{\Sigma L}, e^2/C_{\Sigma R}$, only a single electron fluctuates between the dots: $(N_L, N_R) \leftrightarrow (N_L \pm 1, N_R \mp 1)$, and the inter-dot tunneling is only a small perturbation to the system. The total electron number is constant $N =$

2. Coulomb-Blockade Effect and Single-Electron Tunneling: Theory

$N_L + N_R$. The ground state of the system is then a superposition of two ground states with different charge configurations [Pfa98]:

$$|N\rangle = a|N_L, N_R\rangle + b|N_L + 1, N_R - 1\rangle, \quad (2.53)$$

where the coefficients depend on the detuning of two *decoupled* ground states for the isolated dots $\delta E = E(N_L + 1, N_R - 1) - E(N_L, N_R) = \mu_{LR}$ (see below) and the tunneling strength t . The ground states of this coupled two-level system are

$$E_- = \frac{1}{2} \left\{ E(N_L, N_R) + E(N_L + 1, N_R - 1) - \sqrt{(\delta E)^2 + 4t^2} \right\}, \quad (2.54)$$

$$E_+ = \frac{1}{2} \left\{ E(N_L, N_R) + E(N_L + 1, N_R - 1) + \sqrt{(\delta E)^2 + 4t^2} \right\}, \quad (2.55)$$

namely the bonding and anti-bonding states, respectively. Which can be further written as

$$E_- = \bar{\mu} - \frac{1}{2} \sqrt{(\delta E)^2 + 4t^2}, \quad (2.56)$$

$$E_+ = \bar{\mu} + \frac{1}{2} \sqrt{(\delta E)^2 + 4t^2}, \quad (2.57)$$

where, $\bar{\mu} = (E(N_L, N_R) + E(N_L + 1, N_R - 1))/2$ is the average of the chemical potential on the left and right dots. The distance between the molecular states is

$$E_+ - E_- = \sqrt{(\delta E)^2 + 4t^2}. \quad (2.58)$$

The detuning between the two decoupled ground states is the chemical potential difference between the dots:

$$\begin{aligned} \delta E &= E(N_L + 1, N_R - 1) - E(N_L, N_R), \\ &= \mu_{LR}, \end{aligned}$$

which can be tuned by the gate voltages as shown in Eq. [2.47]. In Fig. 2.8 (a) and (b), the molecular states are illustrated in the level diagram and plotted as a function of the detuning.

Close to the crossing points along the line of p1 and p2, the detuning is zero and the tunnel-coupling induced level splitting $(E_+ - E_-) - |\delta E|$ reaches its maximum $2t$. Both coefficients in Eq. [2.53] equal 0.5, indicating a single electron can be found on the two dots with an equal probability. Being completely delocalized among the two dots, a single electron in the bonding state tunnels back and forth between the two dots at a Rabi frequency of $\Omega_0 = 2t/\hbar$. However, at the crossing point p1 the bonding state is below the Fermi levels in the contacts with a distance of t . At the crossing point p2, the bonding state is above the Fermi levels with a distance of t . At sufficiently low

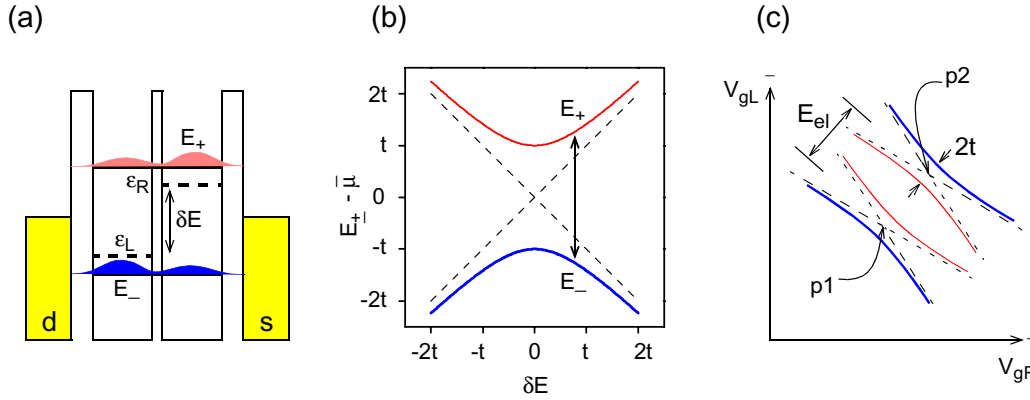


Figure 2.8: (a) A level diagram illustrates the formation of the bonding (E_-) and the anti-bonding (E_+) molecular states in a double dot. The dashed lines represent the two decoupled quantum states (ϵ_L and ϵ_R). (b) The bonding and the anti-bonding molecular states as a function of the detuning (δE). (c) The observation of molecular states near the crossing points in a charging diagram.

temperatures, the bonding state at p1 (p2) is always occupied (empty) and no electron tunnels through the double dot. Tunneling through the bonding state can be tuned by gate voltages as shown in Fig. 2.8 (c).

Along the boundaries of the hexagons (dashed lines in Fig. 2.9), the detuning becomes nonzero, but the bonding state is almost aligned with the Fermi levels in the contacts. The nonzero detuning will “localize” the electron in one of the dot. The localization depends on the inter-dot tunneling strength and the magnitude of the detuning. The single electron is totally localized on one of the dot when the inter-dot tunneling strength is negligibly small, which corresponds to the situation discussed in the previous section. Given a strong inter-dot tunnel coupling, a single electron on one dot has a small but finite probability to be found on the other dot. Hence, a finite tunneling current can be detected closely along the boundaries of the hexagons in the charging diagram (see Fig. 2.8 (c) and Fig. 2.9). The charging diagrams in this regime are then different to the weak tunnel coupling regime shown in Fig. 2.7.

When an anti-bonding state is aligned with the Fermi energies in the contacts, tunneling is enabled only when the drain-source bias or the temperature becomes comparable to the tunnel splitting ($e|V_{ds}| \approx 2t$ or $k_B T \approx 2t$). In a charging diagram, tunneling through the bonding and anti-bonding states can be resolved, as shown in Fig. 2.8 (c) where the thicker (thinner) solid line corresponds to transport through the bonding (anti-bonding) molecular state. In Fig. 2.9, only tunneling through the bonding states is displayed.

As will be shown in Sec. 4.2 and Sec. 5.2, a localized single electron on one of the dot can be delocalized by microwave radiation when the microwave photons are in resonance with the bonding and anti-bonding states. Rabi oscillations [SW96] and electron transport [SW96, SN96, SWL00] through a tunnel-coupled double quantum dot have been studied theoretically in this regime. Experimentally, Fujisawa *et al* studied PAT through a double quantum dot [FT97].

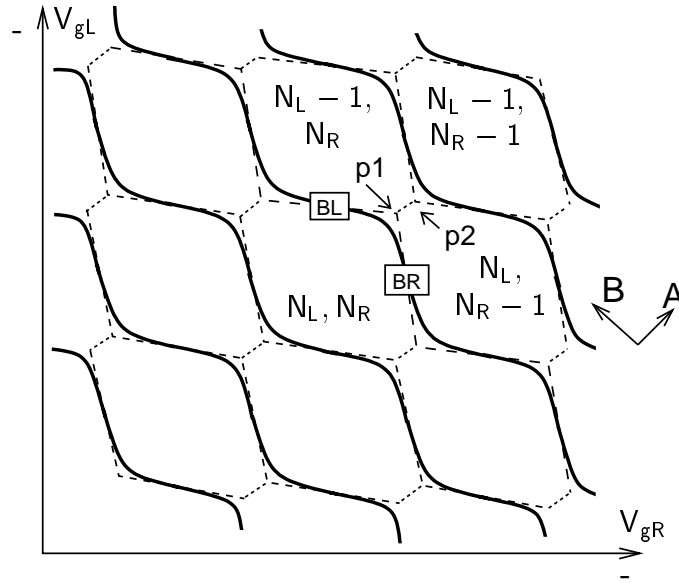


Figure 2.9: A charging diagram of a strongly tunnel-coupled double quantum dot. Solid lines indicate finite tunnel current. The dashed lines are the boundaries of hexagons as shown in Fig. 2.7.

Line Shape of the Tunnel Current Peaks

Resonant tunneling through the double quantum dot strongly depends on the relative magnitude between the tunneling rates of the three barriers (Γ^L , Γ^t , and Γ^R). At low temperatures, the peaks usually have a Lorentzian line shape [Pfa98], which is a result of the coherent superposition of incident tunneling electrons with the two-level quantum system. At higher temperatures, the resonant tunneling peak is temperature broadened since the incident electrons at the Fermi energies are thermally fluctuated.

By varying the gate voltage V_{gL} and fixing the gate voltage V_{gR} , resonant tunneling through bonding molecular states can be reached. By converting the gate voltage V_{gL} into δE according to Eq. [2.47], a single resonant tunneling peak as a function of

V_{gL} can be approximated with

$$I_{ds} \propto \cosh^{-2}\left(\frac{\delta E}{wk_B T}\right), \quad (2.59)$$

where the constant w determines the FWHM ($= 1.76wk_B T$) of the peak. However, this FWHM is smaller than that of a $I_{ds} - \delta E$ peak extracted from the charging diagram in direction **B**, i.e., with a constant $\bar{\mu}$ since both $\delta E = \mu_{LR}$ and $\bar{\mu}$ are shifted. For a single trace extracted across a crossing point in direction **A**, since $\mu_{LR} \equiv 0$ the double dot operates like a single dot and a single peak as a function of $\delta\bar{\mu}$ (refer to Eq. [2.45]) can be well approximated with $\cosh^{-2}(\delta\bar{\mu}/2k_B T)$.

In Sec. 3.3 and Sec. 5.2, the peak broadening will be extracted from the charging diagrams without and with microwave radiation, respectively. As will be shown in Sec. 4.2, photon-induced transport under a near-zero bias, is slightly influenced by thermal fluctuations in the contacts since both the bonding and anti-bonding states are far from the Fermi levels in the contacts. By reducing the fluctuations due to the contacts in this way, the dephasing of electron transport is mainly determined by other dynamic inelastic scattering processes, e.g., by phonons, photons, and impurities involving spin flips.

2. Coulomb-Blockade Effect and Single-Electron Tunneling: Theory

Chapter 3

Transport Spectroscopy of Semiconductor Quantum Dots: Experiment

3.1 Charging Effect in An Array of Silicon Nanocrystals

In this section, a device application based on single-electron tunneling is discussed [GLC97, QGL⁺99]. The device is a memory unit: a metal-oxide-semiconductor field-effect transistor (MOSFET), as schematically shown in Fig. 3.1 (a). For the details on fabrication see page 113 in App. A. Silicon nanocrystals embedded in SiO_x matrix serves as the floating gate [Sze85], in which electrons can be stored. The storage of electrons, representing a bit of information, changes the channel conductance and hence can be read out by measuring the current through the channel.

With a positive gate voltage applied to the polysilicon gate, an inversion layer is formed in the interfacial region between the p -type silicon substrate and the SiO_x layer. This inversion layer serves as an electron channel (n -channel) between the drain and source contacts. The channel is $W = 5 \mu\text{m}$ wide and $L = 10 \mu\text{m}$ long. Between this channel and the nanocrystals close to the channel, the thin layer of SiO_x is about $l_t \approx 2 \text{ nm}$ thick and forms the tunnel barrier. The SiO_x layer, between the nanocrystals and the polysilicon gate, is thicker ($l_g \approx 15 \text{ nm}$). No electron can tunnel through this barrier. A simplified equivalent circuit is drawn in Fig. 3.1 (b) where only a single nanocrystal is considered. The nanocrystals have a cylindrical shape with the long axis (about 13 nm) perpendicular to the surface. The average diameter (along the short axis) of the nanocrystals is about $d \approx 5 \text{ nm}$ (see Fig. A.1 (b) in App. A). The

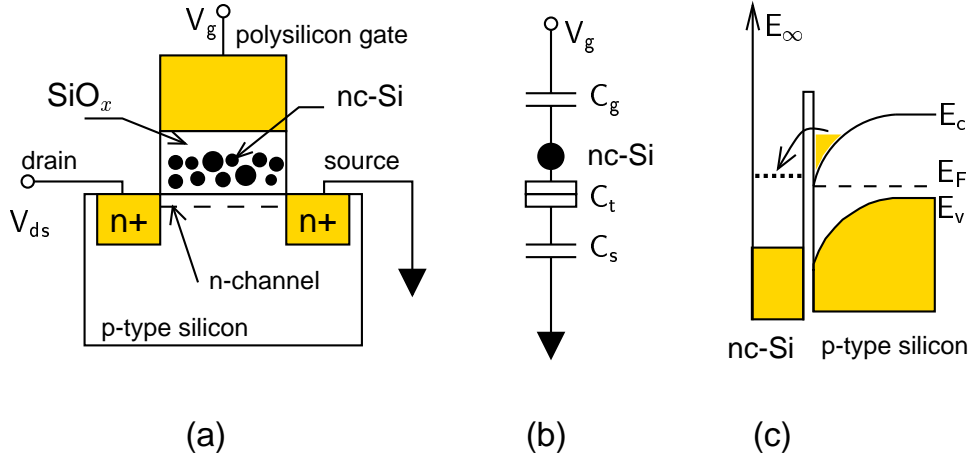


Figure 3.1: (a) A MOSFET-type single-electron memory. Silicon nanocrystals are used as floating gates, storing electrons from an n -channel. Stored electrons in nanocrystals reduce the potential of and hence the conductance of the n -channel. (b) The equivalent circuit for a single nanocrystal. (c) The energy landscape of a single nanocrystal connected to the n -channel by a tunnel barrier.

estimated partial capacitance between a single nanocrystal and the polysilicon gate is $C_g \approx \epsilon_0 \epsilon_r \pi d^2 / 4l_g \approx 4.6 \times 10^{-2}$ aF. Similarly, the partial capacitance between a single nanocrystal and the n -channel is $C_t \approx \epsilon_0 \epsilon_r \pi d^2 / 4l_t \approx 3.5 \times 10^{-1}$ aF. The capacitance C_s is the surface capacitance of the n -channel which depends on the gate voltage and it is much larger than both C_g and C_t . For a single nanocrystal, the charging energy is $E_C \approx e^2 / (C_g + C_t) \approx 0.2$ eV, which is much larger than $k_B T \approx 26$ meV at room temperature.

Since $k_B T \ll E_C$, tunneling of electrons from the n -channel to nanocrystals is regulated by Coulomb-blockade. Electrons can tunnel at certain gate voltages:

$$V_g(N)^{\leftrightarrow} = \gamma \frac{\langle Q^+ \rangle}{C_G} + \frac{(N + \frac{1}{2})e}{C_g}, \quad (3.1)$$

where, γ is a constant structural parameter, C_G is the effective total capacitance between the polysilicon gate and the channel, and $\langle Q^+ \rangle$ is the effective (fixed and mobile) positive charges in the silicon oxide matrix between the polysilicon gate and the channel. N is the number of electrons stored in a single nanocrystal. The first term is a background potential induced by positive charges in the oxide matrix. The second term is due to single electrons stored in the nanocrystal. For simplicity, the Fermi energy and the discrete quantum state energy are absorbed into the first term. This approximation will introduce errors in the effective number of positive charges (see below).

In this real device, the size fluctuation of the nanocrystals is large. The induced energy fluctuation is larger than the temperature broadening. The discreteness of quantum states of nanocrystals is smoothed out. In this case, nanocrystals can be approximated as metallic islands as discussed in Sec. 2.1. To describe the effect of the storage of electrons on the current through the channel, an average electron number $\langle N \rangle$ is adopted. With $\langle N \rangle$ electrons stored in each nanocrystal, the threshold voltage V_{th} of V_g for opening the n -channel is modified¹:

$$V_{th} = V_{th}^0 - \frac{\langle Q^+ \rangle}{C_G} - \frac{-em\langle N \rangle}{C_G} \frac{C_t}{C_g + C_t}, \quad (3.2)$$

where, V_{th}^0 is a constant determined by the Fermi level in the p -type silicon substrate [Sze85], m is the effective total number of nanocrystals close to the channel. The second term indicates that positive charges in the silicon oxide matrix decrease the threshold voltage. The third term is the effect of electron storage which increases the threshold voltage. Assuming a Gaussian distribution for the diameters of nanocrystals, the average electron number at a certain gate voltage of V_g is obtained self-consistently

$$\begin{aligned} \langle N \rangle &= \sum_{N=1}^{\infty} \int_{C_N}^{C_{N+1}} \frac{N}{\sqrt{2\pi\sigma}} \exp\left\{-\frac{(C_g - C_0)^2}{2\sigma^2}\right\} dC_g, \\ C_N &= \frac{Ne}{V_g - \gamma \frac{\langle Q^+ \rangle}{C_G}}, \\ C_{N+1} &= \frac{(N+1)e}{V_g - \gamma \frac{\langle Q^+ \rangle}{C_G}}, \end{aligned}$$

where, C_0 and σ are the average and the variance of C_g , respectively.

Under a small drain-source bias, a direct current flows through the channel which is opened when $V_g > V_{th}$. In the linear regime ($V_{ds} \ll V_g - V_{th}$), the current is proportional to the gate voltage:

$$I_{ds} = \begin{cases} I_{ds}^0(V_g - V_{th}) & V_g \geq V_{th}; \\ 0 & V_g < V_{th}. \end{cases} \quad (3.3)$$

By measuring the $I_{ds} - V_g$ characteristics, single-electron charging effect is observed in the shift of threshold voltage and hence in the variation of drain-source current. In Fig. 3.2, the measured $I_{ds} - V_g$ characteristic is compared to the simulation based on the above model. Two curves are measured by increasing the gate voltage from -20 V to +35 V (curve (a) in Fig. 3.2) and by continuously sweeping the gate voltage from

¹Here, we disregard the different work functions of p -type silicon, silicon oxide and the P^+ -doped polysilicon gate, which induce a finite threshold gate voltage.

3. Transport Spectroscopy of Semiconductor Quantum Dots: Experiment

+35 V to -20 V (curve (b) in Fig. 3.2), respectively. In curve (a), six almost equally spaced reduction of drain-source current are clearly resolved when the gate voltage is above +10 V. In curve (b) the current smoothly and linearly decreases to zero as the n -channel is closed by a negative gate voltage.

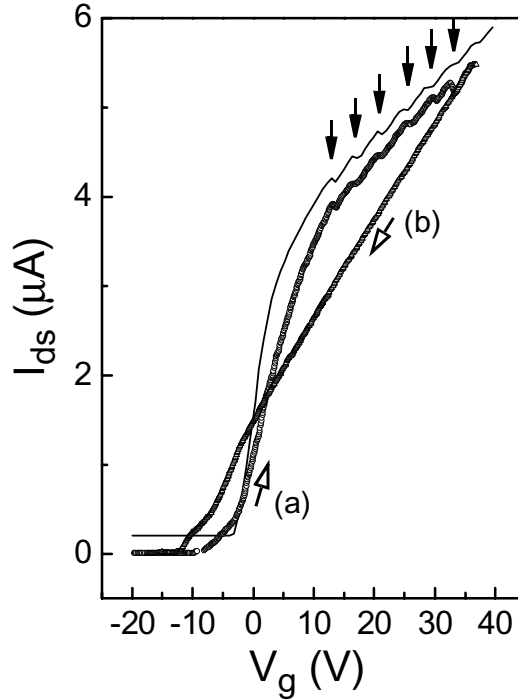


Figure 3.2: The $I_{ds} - V_g$ characteristics measured at room temperature. The curve (a) represents the data obtained by sweeping the gate voltage from negative to positive. The curve (b) is measured by sweeping back the gate voltage to -20 V immediately after the sweeping of curve (a). The solid line (offset by $0.25 \mu\text{A}$ for clarity) is a simulation based on single-electron tunneling taking into account the drift of positive charges in the SiO_x matrix and a size distribution of nanocrystals.

When the gate voltage is below +10 V the observed variation in current is mainly due to the drift of positive mobile charges, leading to a voltage-dependent threshold. Above +10 V, the influence of mobile positive charges keeps constant since most of the mobile charges are driven to the interface between the channel and the silicon oxide layer. When electrons tunnel into nanocrystals one by one regulated by Coulomb-blockade, the channel potential and electron density in the channel are reduced, inducing step-like features in current. The simulation (solid line) shows good agreement with the observation. In the simulation, parameters are taken as $m = 8.5 \times 10^5$, $C_0 = 4.2 \times 10^{-2} \text{ aF} \approx C_g$, $\sigma = 1.0 \times 10^{-3} \text{ aF}$ and $C_G = 0.1 \text{ pF}$. The density of fixed and mobile

positive charges are taken as $6 \times 10^{12} \text{ cm}^{-2}$ and $6 \times 10^{13} \text{ cm}^{-2}$, respectively, both of which are one order of magnitude higher than the density of nanocrystals ($m/(WL) \approx 1.7 \times 10^{12} \text{ cm}^{-2}$).

In comparison to curve (a), curve (b) is almost linear, indicating that no charge is moving around in the SiO_x matrix. From this, it is inferred that both the electrons stored in nanocrystals and the mobile positive charges are fixed at least during the measurement time (about 3 minutes). The faster decay in current in the negative gate voltage region indicates that mobile positive charges are dragged by the electric field toward the polysilicon gate and electrons begin to leak out of the nanocrystals toward the substrate where they are recombined with holes.

Summarizing for this section, Coulomb-blockade of electron storage in silicon nanocrystals is observed at room temperature. Single electrons are stored in nanocrystals by tuning the gate voltage. The storage time is longer than 3 minutes. Due to a large size fluctuation and about 8.5×10^5 nanocrystals are charged simultaneously, discrete quantum states are not resolved in this device.

3.2 Transport Spectroscopy of Artificial Atoms: Single Quantum Dots

In a quantum dot formed in the 2DEG of an AlGaAs/GaAs heterostructure, the tunnel barriers and the potential of the dot are well controlled by relevant gate voltages. In Sec. 3.2.1, the formation of such a quantum dot is described. In Sec. 3.2.2, transport spectroscopy is performed mainly by measuring the Coulomb-blockade diamonds, revealing both the ground states and excited states. The lifetime of ground states is studied by tuning one of the tunnel barriers.

The measurements are conducted at a $^3\text{He}/^4\text{He}$ bath temperature of $T_b = 140 \text{ mK}$ under zero magnetic field. The actual electron temperature is saturated at $T = 170 \text{ mK}$.

3.2.1 Formation of A Single Quantum Dot

This quantum dot is realized from QD-sample#1 described on page 114 in App. A. As shown in Fig. 3.3, the single dot² is formed by applying proper negative gate voltages to

²Only the measurement shown in Fig. 3.4 were obtained with a different configuration of gate voltages as shown in Fig. 3.3. For the left single dot, the plunger gate is formed by gate #10 and #15. Similarly, the gates #2 and #13 form the plunger gate for the right single dot. The gates #3 and #17 are bounded together, biased at around -600 mV , serve as the left tunnel barrier for the left single dot. The gates #14 and #16, biased at -670 mV , form the right tunnel barrier for the right single dot. The gates #1 and #8 are biased around -627 mV .

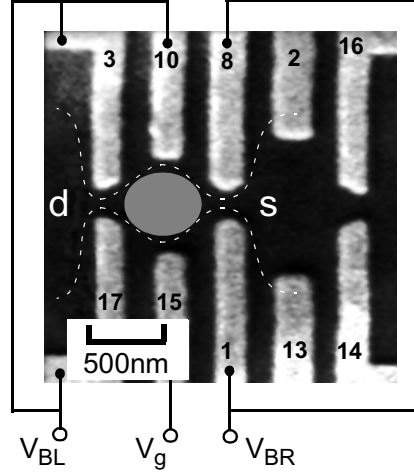


Figure 3.3: The formation of the left single quantum dot. The white dashed lines schematically show the edge of the 2DEG.

gates #1, #3, #8, #10, #15 and #17. Gate #15 serves as the plunger gate controlling the dot potential. The left (formed by gates #3 and #17) and right (formed by gates #1 and #8) tunnel barriers can be well tuned by gate voltage V_{BL} and V_{BR} , respectively. The other gates are not used and hence are grounded to minimize the possible electronic noise.

The 2DEG is located 90 nm below the surface of an AlGaAs/GaAs heterostructure. The electron sheet density at 4 K is about $n_s \approx 1.7 \times 10^{11} \text{ cm}^{-2}$, and an electron mobility of $\mu_e \approx 8 \times 10^5 \text{ cm}^2/\text{Vs}$, yielding a mean free path of around $5 \mu\text{m}$ (for more details see page 114 in App. A). The lithographic diameter of the dot is about 800 nm, while the effective electronic diameter is expected to be smaller (see below).

With the left and right tunnel barriers tuned in balance, the dot's conductance is measured while the plunger gate voltage is swept. The conductance shows more than 200 oscillations as shown in Fig. 3.4 (a). By decreasing the plunger gate voltage, not only the dot potential is increased, but also both the left and right tunnel barriers are more opaque. As shown in Fig. 3.4 (b), peaks (I and II) at higher gate voltage have a Lorentzian shape, while at low gate voltages peaks have a $\cosh^{-2}(e\alpha(V_g - V_g^{\leftrightarrow})/2k_B T)$ shape. The Lorentzian shape indicates that the life-time broadening overcomes the temperature broadening ($\hbar\Gamma \gg k_B T$). Some peaks between I and II have a temperature broadened Breit-Wigner peak shape since the lifetime and temperature broadening are comparable in magnitude. This effect is revealed further in detail by tuning one of the tunnel barriers (see Sec. 3.2.2).

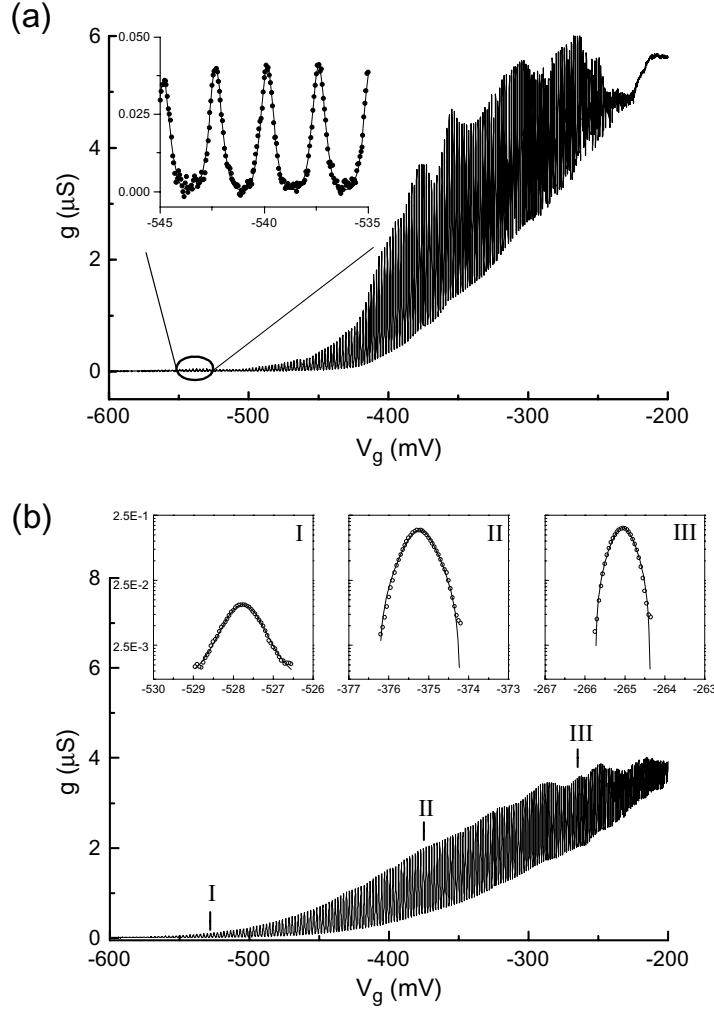


Figure 3.4: (a) More than 200 Coulomb-blockade oscillations are measured in the quantum dot as shown in Fig. 3.3. In the inset, conductance peaks are fitted with $\sum_{i=0}^5 \cosh^{-2}(-e\alpha(V_g - V_{g_i}^{\leftrightarrow})/2k_B T)$. (b) Similarly, about 200 oscillations are found from the right quantum dot (see the footnote on page 39). In the insets, three single conductance peaks are extracted at different gate voltages, which is marked by I, II and III. For low gate voltage (I), the conductance peak has a $\cosh^{-2}(-e\alpha(V_g - V_{g_i}^{\leftrightarrow})/2k_B T)$ shape, i.e., the temperature broadening dominates. At higher gate voltage (III), the large dot-contact barrier's transparency gives rise a Lorentzian shaped peak, indicating the lifetime broadening. $T = 170$ mK.

3.2.2 Level Spectroscopy

As discussed in Chap. 2, Coulomb-blockade diamonds characterize the quantum dot in both the linear and nonlinear regimes. Within the CB regimes, i.e., in the CB diamonds,

no electron tunneling is enabled, while in SET regimes electrons tunnel through ground states and excited states.

In Fig. 3.5, CB diamonds are shown. CB regimes are marked by “CB”, and SET regimes are denoted by “SET”. In the direction of lowering the gate voltage under zero bias $V_{ds} = 0$, each peak indicates a ground-state resonance where a single electron is removed from (added to) the quantum dot. At a finite drain-source bias, each ground-state resonance splits into two resonances (“gd” and “gs”) as shown in Fig. 3.5. The solid lines “gd” and “gs” (boundaries of the Coulomb diamonds) mark the resonance of a ground state which is matched by the Fermi levels in the drain and source contacts, respectively. The dashed lines (β , γ and δ) represent transport through excited states. In parallel with the boundary “gd”, these resonances are drain-related. From the slopes of the drain- and source-related boundaries ($s_1 = +9.75$ and $s_2 = -6.56$) (refer to the definitions on page 19), the coefficient of converting the gate voltage to energy scale is obtained: $\alpha = 1/(|s_1| + |s_2|) = 6.1 \times 10^{-2}$. From the distance (ΔV_g) between two adjacent conductance peaks, the addition energy is obtained $E_{add} = e\alpha|\Delta V_g| \approx 345 \mu\text{eV}$. In the SET regime (see Fig. 3.5), tunneling through excited states is visible. Excited states β and γ are observed $\Delta\epsilon_\beta^* \approx 110 \mu\text{eV}$ and $\Delta\epsilon_\gamma^* \approx 250 \mu\text{eV}$ above the ground state. The excited state δ is located $\Delta\epsilon_\delta^* \approx 170 \mu\text{eV}$ below the ground state. The charging energy estimated is about $E_C = e^2/C_\Sigma \approx 205 \mu\text{eV}$ by taking an averaged level spacing of $140 \mu\text{eV}$.

Assuming a 2D disk shaped quantum dot, the total capacitance of the dot is $C_\Sigma \approx 8\epsilon_0\epsilon r$, which yields a dot diameter of about $1.5 \mu\text{m}$. On the other hand, since $\bar{\Delta} \approx \hbar^2/m^*r^2$, where $m^* \approx 0.067m_e$ is the effective electron mass, the effective dot diameter is then estimated as $2r \approx 200 \text{ nm}$. The different values of dot size estimated above have large deviations from the lithographic diameter ($\approx 0.8 \mu\text{m}$). The irregular shape rather than sphere and the presence of nearby gold gates induce errors in the above estimations. Since the quantum dot is formed 90 nm below the surface and the gates have a width about 220 nm , the upper limit for the effective dot diameter is around $2r \approx 600 \text{ nm}$. With such a dimension, the dot contains about $n_s \times \pi r^2 \approx 480$ electrons. Since more than 200 oscillations are observed,³ there are about 200 – 300 electrons in the dot when the gate voltage is around $-700 \text{ mV} - -600 \text{ mV}$.

To reveal the influence on confined electronic states by contacts, CB diamonds from the conductance are measured by closing the right tunnel barrier: V_{BR} changes from -607.6 mV to -627.6 mV . As shown in Fig. 3.8, four measurements in the order (from (a) to (d)) of reducing the right tunneling rate are shown. The left tunnel barrier

³As mentioned in the footnote on page 39, the gate configuration for the measurements shown in Fig. 3.4 is different to that shown in Fig. 3.5. The dots, however, are almost the same since the gate voltages applied are almost identical. With two bounded gates as the plunger gate, the gate capacitance is about two times the gate capacitance when only one gate is applied as the plunger gate. Hence, the peak distance in Fig. 3.4 is only about half of that in Fig. 3.5.

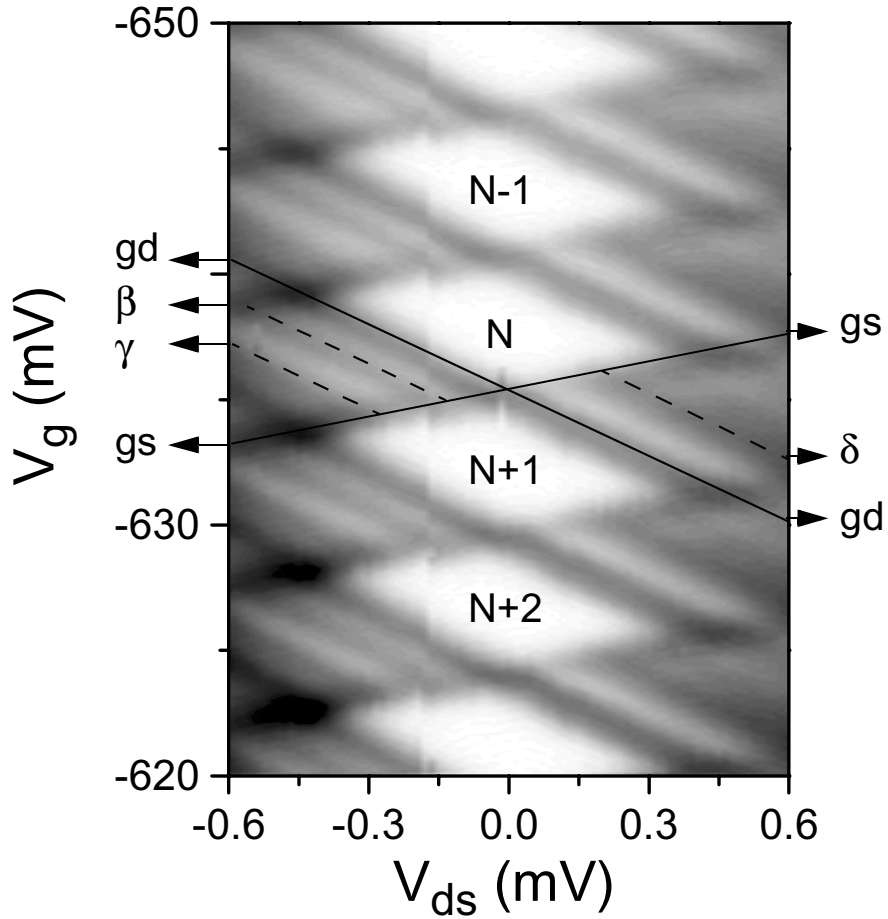


Figure 3.5: CB diamonds (conductance), measured from the left single dot with $V_{BL} = -600.08$ mV and $V_{BR} = -627.6$ mV, is plotted in a linear grayscale presentation (white: $g \sim 0 \mu\text{S}$, black: $g < 0.55 \mu\text{S}$). The solid lines mark the resonances of ground states (gd: drain-related ground state resonance, gs: source-related ground state resonance). The dashed lines represent transport through excited states (β , γ , and δ , see text and Fig. 3.6 for details). $T = 170$ mK.

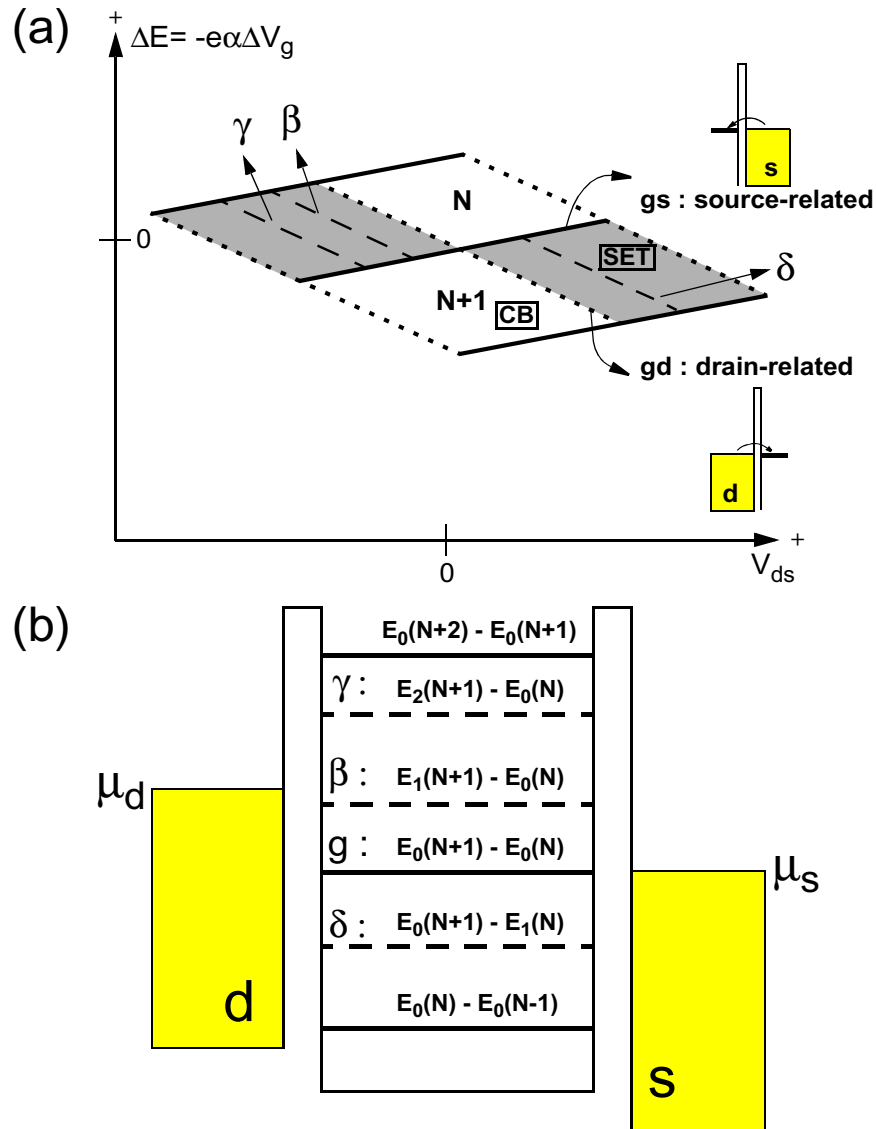


Figure 3.6: (a) Four diamonds are extracted from the measurement shown in Fig. 3.5. The vertical axis is converted from the gate voltage by $\Delta E = -e\alpha\Delta V_g = -e\alpha(V_g - V_g^{\leftrightarrow})$, V_g^{\leftrightarrow} is the resonance position at zero drain-source bias. The resonances of β , γ and δ , which are in parallel with the dotted boundaries, are drain-related excited state resonances. (b) Possible transitions through excited states of the dot with N or $(N + 1)$ electrons are listed.

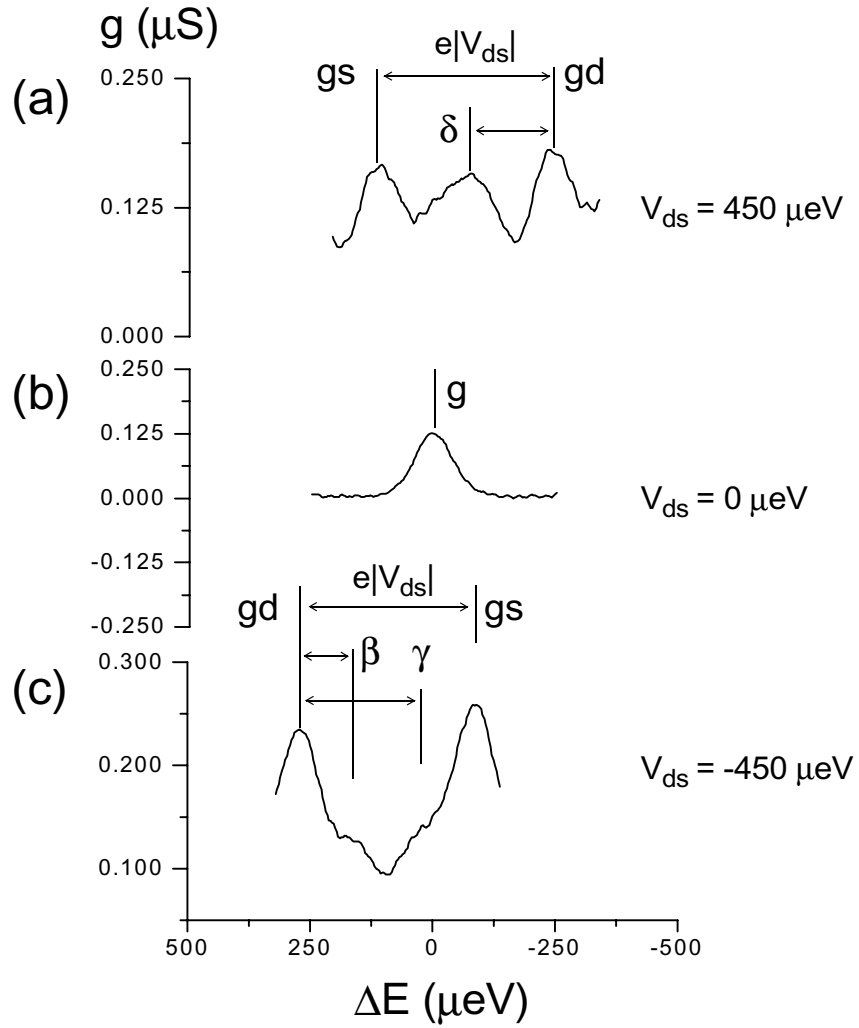


Figure 3.7: Single traces are extracted from Fig. 3.5 at (a) $V_{ds} = +450 \mu\text{eV}$, (b) $V_{ds} = 0 \mu\text{eV}$, and (c) $V_{ds} = -450 \mu\text{eV}$. Ground state resonance shown in (b) splits into two (drain- and source-related) resonances separated by $e|V_{ds}|$. Between the ground state resonances, resonances of excited states (β , γ and δ) are revealed.

3. Transport Spectroscopy of Semiconductor Quantum Dots: Experiment

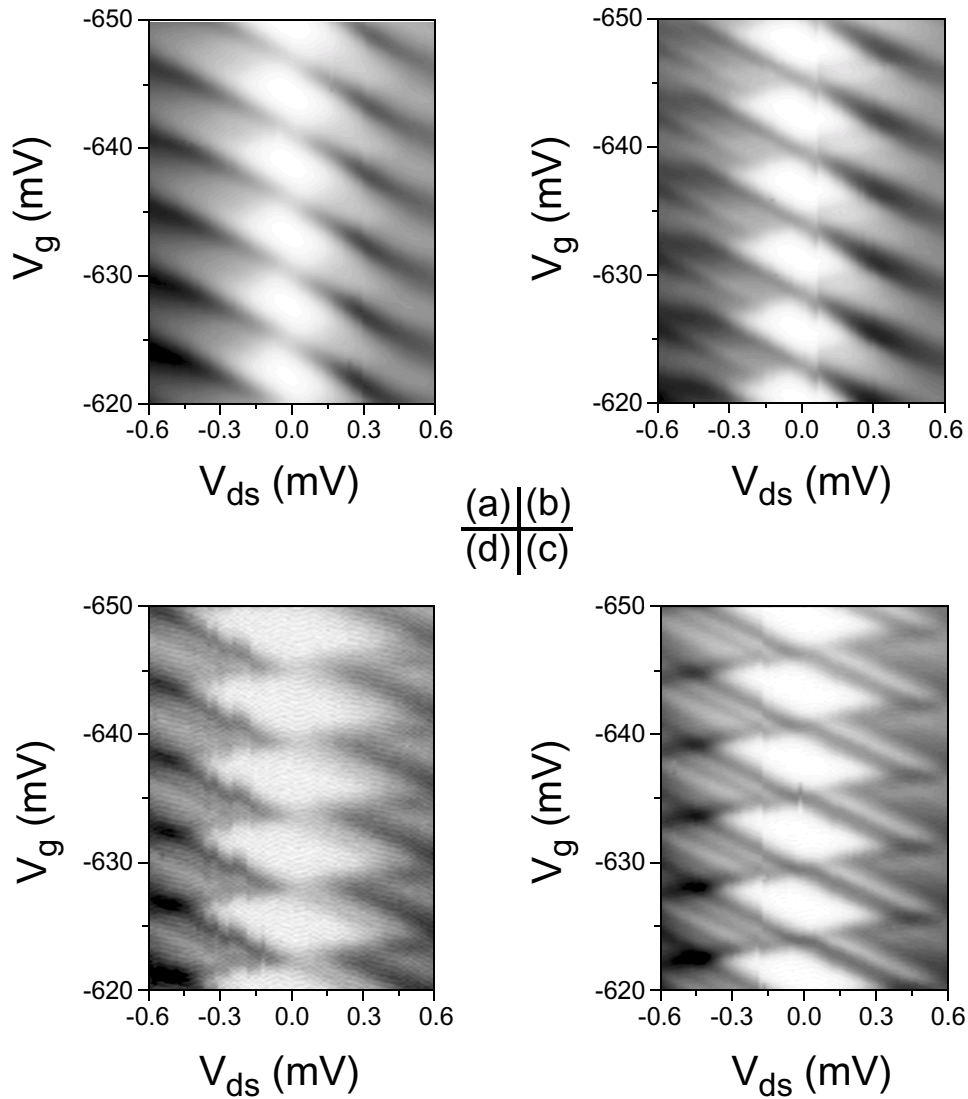


Figure 3.8: CB diamonds (conductance) of the left single dot with different tunneling rates through the right tunnel barrier, which is tuned by the gate voltage V_{BR} : (a) -607.6 mV (black: $g < 0.7 \mu\text{S}$, white: $g \sim 0 \mu\text{S}$), (b) -617.6 mV (black: $g < 0.4 \mu\text{S}$, white: $g \sim 0 \mu\text{S}$), (c) -627.6 mV (black: $g < 0.5 \mu\text{S}$, white: $g \sim 0 \mu\text{S}$), and (d) -630.6 mV (black: $g < 0.04 \mu\text{S}$, white: $g \sim 0 \mu\text{S}$). $T = 170$ mK.

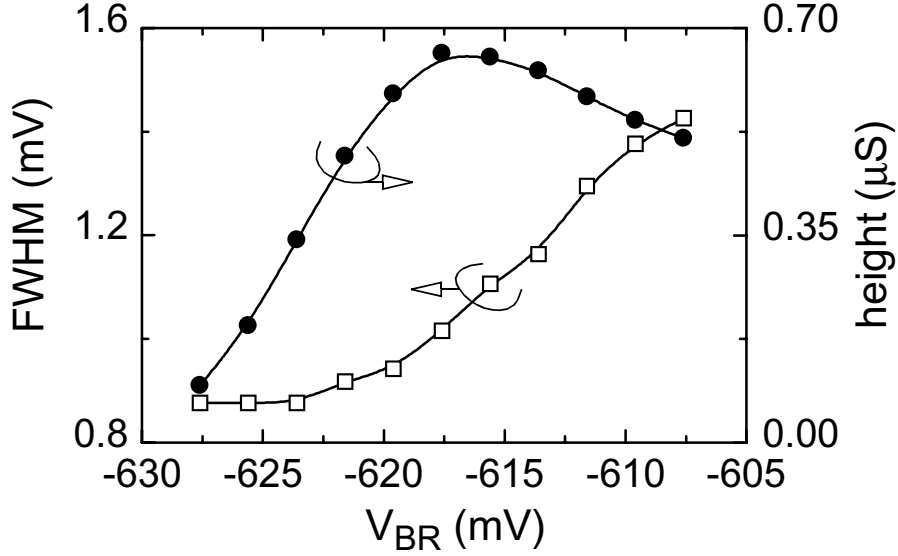


Figure 3.9: The FWHM (open squares) and the peak height (solid circles) of a conductance peak at $V_{ds} = 0$ vary with the gate voltage V_{BR} controlling the right tunnel barrier. $T = 170$ mK.

($V_{BL} = -600.08$ mV) is tuned to be small: $h\Gamma^d \ll k_B T$. With the largest tunneling rate of the right barrier ($V_{BR} = -607.6$ mV), Coulomb diamonds are still clearly shown (see Fig. 3.8 (a)). Under strong coupling between the dot and source contact, the source-related resonance is not well established at a finite drain-source bias, while the drain-related resonance is stronger and sharper. It follows that the quantum state at the Fermi energy in the source is much more broadened than that at the drain Fermi level. At zero drain-source bias, the quantum dot state at the Fermi level possesses a level width as a sum of the partial tunneling rates to both contacts. The FWHM of the conductance peak at a finite temperature is [GGGK⁺98]

$$\text{FWHM} \approx \frac{0.78h(\Gamma^d + \Gamma^s) + 3.52k_B T}{e\alpha}. \quad (3.4)$$

The FWHM is expected to decrease linearly with reducing the tunneling rate. As shown in Fig. 3.9, the FWHM and the peak height at resonance is plotted versus the gate voltage V_{BR} . The conductance of the right barrier is found proportional to V_{BR} in the voltage range shown. In accordance with Eq. [3.4], the FWHM linearly depends on the right tunneling rate when $V_{BR} > -617$ mV. When the tunneling rate Γ^s approaches zero with further decrease in V_{BR} ⁴, the FWHM reflects only the broadening

⁴At $V_{BR} = -627.6$ mV, Γ^s is small but not zero, otherwise no tunneling through the dot is enabled, i.e., no FWHM can be determined.

from the drain contact and thermal broadening. As shown in Fig. 3.9, the minimum peak height (at $V_{BR} = -627.6$ mV) is $e^2\Gamma^d\Gamma^s/4k_B T(\Gamma^d + \Gamma^s) \approx 0.11 \mu\text{S}$, and the minimum FWHM is $e\alpha \times \text{FWHM} \approx e\alpha \times 0.88$ mV $\approx 53.7 \mu\text{eV}$. Taken the balanced tunnel barriers ($\Gamma^d \approx \Gamma^s$) at $V_{BR} = -627.6$ mV, the total lifetime broadening is estimated: $h\Gamma = h(\Gamma^d + \Gamma^s) \sim h \times 70$ MHz. Accordingly, the electron temperature can be estimated (about 176 mK) and is in agreement with the bath temperature of the $^3\text{He}/^4\text{He}$ mixture.

While decreasing the tunneling rate Γ^s , the conductance increases at first, and then decreases linearly. The increase of peak conductance with reducing the tunneling rate is a signature of resonant tunneling. The further decrease in tunneling rate reduces the total transmission rate.

3.3 Transport Spectroscopy of An Artificial Molecule: A Double Quantum Dot

A tunnel coupled double quantum dot presents a well controlled two-level system (two quantum states, one in each dot), in which the detuning between two levels and hence the localization of an electron in the two dots can be tuned by the gate voltages applied to each dot and by the tunnel coupling between the dots. The double dot can be tuned into the weak and strong coupling regime. In the weak coupling regime, the inter-dot interaction is dominated by electrostatic inter-dot charging effect. In the strong coupling regime, electrons can tunnel back and forth between the dots easily. The two coupled levels form the bonding and anti-bonding molecular states. Even with a large detuning between the two quantum levels, tunneling through the bonding molecular state can be observed. In this regime, both the tunnel coupling and the electrostatic interaction have to be taken into account. Under weak tunnel coupling of the double dot to the contacts, the dephasing due to electron-electron interaction between the dots and the contacts is minimized. It is possible to study the interaction of molecular states with excitation from the environment, e.g., discrete phonon modes [KR94, FvdWK00]. Double quantum dots are proposed to realize quantum bits (qubits) [LD98] and detectors for quantum noise [AK00].

3.3.1 Formation of A Tunnel-Coupled Double Quantum Dot

The double quantum dot is realized from the same sample as that has been studied in Sec. 3.2 (see more detailed descriptions on page 114 in App. A). As shown in Fig. 3.10, the gates #3 and #17 form the tunnel barrier coupling the left dot with the drain contact. The gates #14 and #16 control the tunnel barrier between the right dot

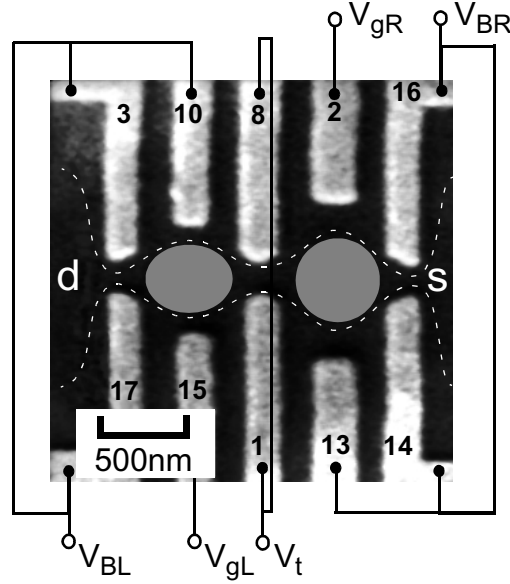


Figure 3.10: A double quantum dot is formed from the same sample shown in Fig. 3.3. The gate voltage $V_{BL} = -600$ mV and $V_{BR} = -670$ mV control the left and right tunnel barriers, respectively. The gate voltage $V_t > -605$ mV is for tuning the tunnel coupling between the dots. The gate voltage V_{gL} and V_{gR} are used for tuning the potentials on the left and the right dot, respectively. The white dashed lines schematically show the edge of 2DEG. $T = 170$ mK.

and the source contact.⁵ Accordingly, gates #1 and #8 are used to form the central tunnel barrier which couples the left and the right dot. The gates #15 and #2 serve as the plunger gates for the left and the right dot, varying the dot potentials, respectively. Each plunger gate has a crosstalk to the neighboring dot, i.e., a change in the left (right) plunger gate voltage will induce a slight potential change in the right (left) dot. The sample is cooled at a bath temperature of $T_b = 140$ mK, while the electron temperature is about $T = 170$ mK. No magnetic field is applied to the sample.

With the central gate voltage fixed at -590 mV and -580 mV, two dots are weakly and strongly coupled, respectively. As shown in Fig. 3.11, the tunnel current plotted in the $V_{gR} - V_{gL}$ plane forms the charging diagram, revealing the charge configurations on both dots. As discussed in Sec. 2.3 (see Fig. 2.7), the charging diagram at weak coupling consists of pairs of discrete peaks (p1 and p2) in a rhombic pattern. The distance between p1 and p2 reflects the electrostatic charging energy between the dots. In Fig. 3.11 (a), the peaks p1 and p2 are broadened and very close to each other.

⁵Since these two gates are bounded together with gate #13 which is used mainly to define the right dot, a change in the tunnel barrier is always accompanied with a change in the dot shape and the dot potential. However, the impact of the latter change on transport can be neglected.

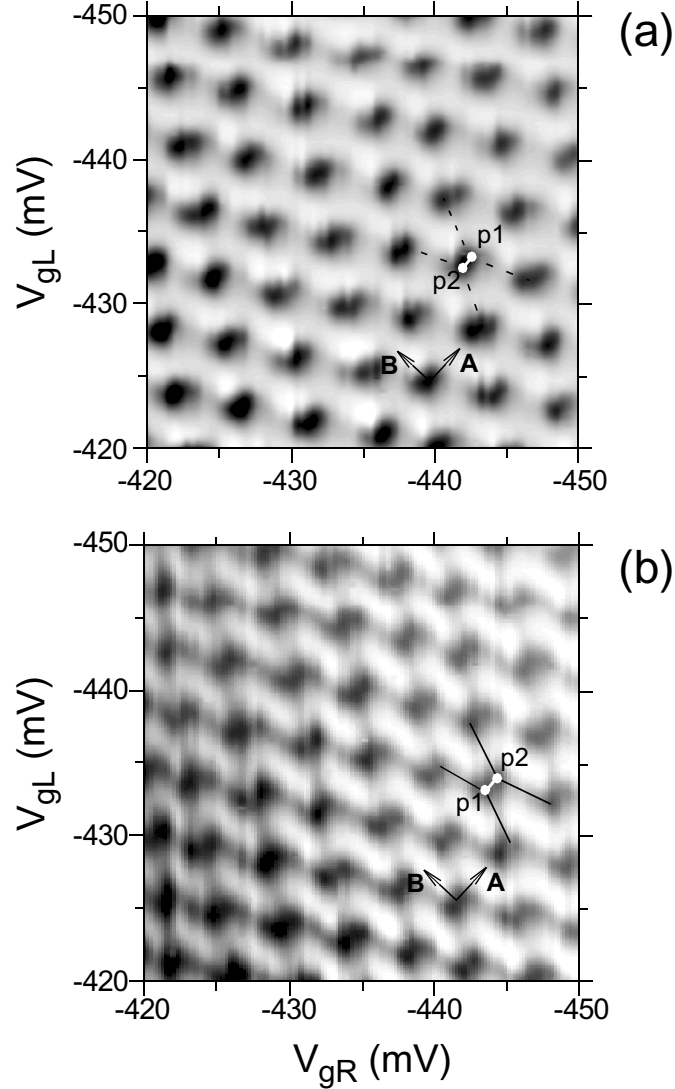


Figure 3.11: Charging diagrams (current) of the (a) weakly coupled and (b) strongly coupled double dot are shown in the linear grayscale presentation. In (a), black: $I_{ds} \geq -12$ pA, white: $I_{ds} \approx 0.5$ pA). In (b), black: $I_{ds} \geq -18$ pA, white: $I_{ds} \approx -1.5$ pA). Accordingly, the central gate voltage V_t is -590 mV and -580 mV. In both cases, the drain-source bias is less than 50 μ V and $T = 170$ mK.

In contrast, the charging diagram at stronger coupling shows a different pattern with peak p1 and p2 well separated (see Fig. 3.11 (b)). The finite tunnel current along the boundaries of hexagons are tunneling through the bonding molecular state, which is not observed in the weak coupling regime.

3.3.2 Characterization of the Double Quantum Dot

Measurement of charging diagrams is the most important method for characterizing double quantum dots [BHvKE96, FT97]. To calibrate the energy scale of the control gate voltages, the factor α_L and α_R (defined on page 28, relating the left and the right gate voltages to the chemical potential difference between the dots) have to be obtained. From transport under finite drain-source bias, however, it is difficult to reveal these values since transport through a double dot in the nonlinear regime is much more complicate than through a single quantum dot.⁶ In this thesis, the energy calibration is done by determining both sidepeaks from photon-assisted tunneling (PAT) (see Sec. 5.2) and the energy-to-voltage factors for each single dot without microwave radiation. We obtain the following factors (see Sec. 2.3.1 for the definition of these parameters):

$$\begin{aligned}\gamma_{gL} &\approx 8 \times 10^{-2}, \\ \gamma_{RL} &\approx 2 \times 10^{-2}, \\ \gamma_{gR} &\approx 7 \times 10^{-2}, \\ \gamma_{LR} &\approx 1 \times 10^{-2}.\end{aligned}$$

The effective coefficients are $\alpha_L \approx \alpha_R \approx 6 \times 10^{-2}$ for the left (V_{gL}) and the right (V_{gR}) gate voltage. The direction **A** and **B** have slopes of $k_A \approx 1$ and $k_B \approx -0.8$, respectively.

Under finite bias, the onset of tunneling through an excited state starts at $\Delta\epsilon^* \approx 120 \mu\text{eV}$ above the ground state, which is consistent with the excited states ($\Delta\epsilon_\beta^* = 110 \mu\text{eV}$, $\Delta\epsilon_\gamma^* = 250 \mu\text{eV}$, and $\Delta\epsilon_\delta^* = 170 \mu\text{eV}$) obtained for the single dots (see Sec. 3.2). The addition energies for the left (E_{addL}) and right (E_{addR}) dot are $351 \mu\text{eV}$ and $232 \mu\text{eV}$, respectively. Accordingly the total capacitance of the dots estimated are $C_{\Sigma L} \approx 693 \text{ aF}$ and $C_{\Sigma R} \approx 755 \text{ aF}$. From Eq. [2.50] or Eq. [2.51], the inter-dot capacitance is obtained as $C_t \approx 100 \text{ aF}$ and $C_t \approx 181 \text{ aF}$ from the charging diagrams shown in Fig. 3.11 (a) and (b), respectively. According to Eq. [2.52], the corresponding inter-dot electrostatic energies changed between p1 and p2 is estimated as $E_{el} \approx 50 \mu\text{eV}$ and $E_{el} \approx 91 \mu\text{eV}$ for the weak and strong coupling, respectively. The central gate voltage (V_t) changes both the inter-dot tunnel coupling (t) and the inter-dot capacitive coupling (C_t).

In Fig. 3.12 (a), a charging diagram of the dot's conductance (g) is obtained at $V_t = -560 \text{ mV}$. The crossing points p1 and p2 are well separated. Tunneling through

⁶It is still feasible to get α_L and α_R from transport in the nonlinear regime. For a weakly coupled double dot, the crossing point p1 (p2) will split into two in direction **A** under a finite bias. The magnitude of the splitting is proportional to the bias applied. For a very strongly coupled double dot, which can be treated as a large single dot, the charging diagram turns out to show parallel conductance lines.

the bonding state formed by two quantum states with a large detuning (alone the boundaries) is strong and comparable to that through a bonding state with a zero detuning (near the crossing points). With even higher gate voltage V_t , the central tunnel barrier diminishes and electrons' movement from dot to dot is classically allowed. The double dot acts as a large single dot, and parallel conductance lines are formed in the charging diagram. In Fig. 3.12 (c), five single traces extracted along the dashed lines around crossing points (p1 and p2) as show in Fig. 3.12 (a) are plotted. Between the crossing points, finite conductance is clearly resolved. The single trace shown in Fig. 3.12 (d) is approximated by four $\cosh^{-2}(\delta\bar{\mu}/2k_B T)$ -shaped peaks, where $\delta\bar{\mu} = \delta\mu_L$ since $\mu_{LR} = \mu_L - \mu_R \equiv 0$ (refer to Eq. [2.45]). These four peaks are divided into two pairs (s_{1-} , s_{1+}) and (s_{2+} , s_{2-}), respectively. Peak s_{1-} and s_{1+} locate on the right and left side of point p1, respectively. Similarly, s_{2-} and s_{2+} locate on the left and right side of crossing point p2. The results shown here fit into the picture of molecular states formed by two coupled quantum states (see Sec. 2.3.2). Peak s_{1+} and s_{2+} represent tunneling through the anti-bonding states and s_{1-} and s_{2-} stem from transport through bonding states. The difference in the energy of the double dot between p1 (p2) and $s_{1\pm}$ ($s_{2\pm}$) is half of the tunneling strength, i.e., t , as shown in Fig. 3.12 (d). Compared to the large electrostatic splitting $E_{el} \approx 95 \mu\text{eV}$ (the corresponding inter-dot capacitance is about 192 aF), the tunnel splitting $t \approx 45 \mu\text{eV}$ is comparable to the thermal broadening ($3.52k_B T \approx 52 \mu\text{eV}$) at $T = 170 \text{ mK}$. Under near-zero drain-source bias, the tunnel splitting in this double quantum dot is broadened by thermal excitation and the induced peaks are masked between p1 and p2. Transport through the anti-bonding states is indeed excited by thermal energy, otherwise only transport through the bonding states can be observed.

The bonding and anti-bonding molecular states formed by two quantum dots with a zero detuning ($\delta E = 0$) are hardly visible in the charging diagrams when the temperature is high. However, as will be shown in Sec. 5.2, temperature broadening is reduced in photon-induced resonances between two molecular states with a large detuning ($\delta E \neq 0$) since the (anti-) bonding state is (above) below the Fermi levels in the contacts. By minimizing the thermal excitation in this way, the formation of molecular states can thus be clearly resolved.

3.3.3 Interaction of Molecular States with Acoustic Phonons

By tuning the gate voltages V_{gL} and V_{gR} , the energy difference between the molecular states can be controlled. With a zero detuning of the two decoupling quantum states ($\delta E = 0$), strong resonant tunneling through the bonding state is enabled near the crossing points. With a non-zero detuning, no tunneling is allowed given the tunnel coupling between the dots is sufficiently small, i.e., electrons are localized in each dot. However, various excitations can induce transitions between two quantum states,

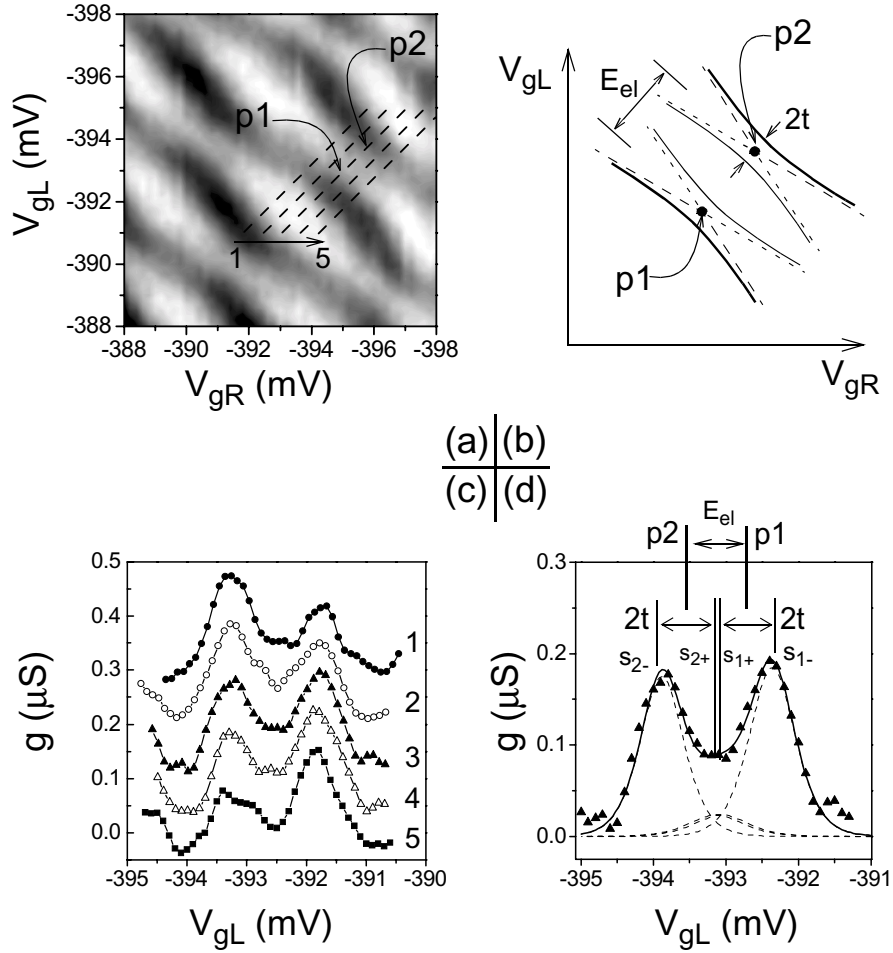


Figure 3.12: (a) The charging diagram (conductance) of the strongly coupled double quantum dot ($V_t = -560$ mV, black: $g < 0.5$ μS , white: $g \approx 0$ μS). (b) Schematic illustration of electrostatic splitting (E_{el}) and tunnel splitting ($2t$) around the crossing points $p1$ and $p2$. (c) Single traces are extracted along dashed lines shown in (a). (d) The fit of curve #3 in (c) reveals the formation of bonding and anti-bonding molecular states. $T = 170$ mK.

generating a finite tunnel current through the double dot. Hence, a double quantum dot can be used as a detector of excitations from the environment. Coupled quantum dots are proposed as quantum spectrometers [AK00, KR94]. Under excitation of microwave photons, photon-assisted tunneling is observed (see Sec. 5.2). One of the natural excitation is from phonons since quantum dots are fabricated in GaAs host crystal. Acoustic phonon energies fit into the energy scale in the double dot (< 350 μeV).

As shown in Fig. 3.13 (a), two neighboring resonant tunneling peaks are plotted. The coupling between the dots is weak ($V_{ds} = -10$ μV , $V_t = -600$ mV, $G_c \approx 0.08e^2/h$)

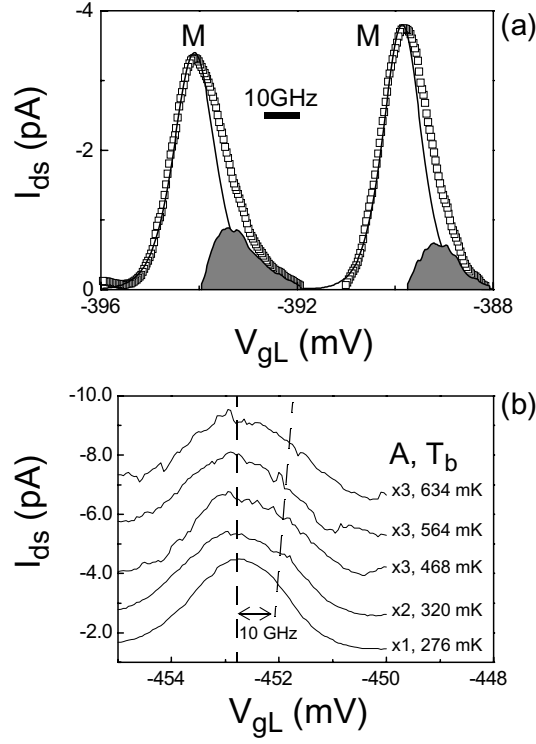


Figure 3.13: (a) A single trace reveals the main resonant tunneling (marked by M) through the double dot. On the right side of the peak, additional off-resonant tunneling current is resolved. The solid lines represent pure resonant tunneling. The dark areas are off-resonant parts. $T = 170$ mK, $G_c \approx 0.08e^2/h$. (b) The position of off-resonant tunneling versus the temperature.

so that the tunneling through the bonding state formed by two quantum states with a large detuning is suppressed. Only isolated peaks at crossing points in a rhombic pattern are presented in the charging diagrams. However, the off-resonance tunneling current is obviously visible, as shown in Fig. 3.13 (a), where the solid lines are main resonant tunneling peaks (M) ($\delta E \sim 0$) as described by $\cosh^{-2}(\delta E/wk_B T)$ with $\delta E = -e\alpha_L \delta V_{gL}$ and $w \approx 2.3$ (refer to Eq. [2.59] on page 33). On the right side of the resonant peaks, where $\delta E < 0$, electrons tunnel from the drain contact to the source contact under a small negative drain-source bias ($V_{ds} \approx -10 \mu\text{V}$). The distance from the main peak (M) to the maximum of off-resonance tunneling peak is about 10 GHz. By increasing the bath temperature with which the electron temperature is in equilibrium, the position of this maximum shifts slightly to the right side of the main peak, as shown in Fig. 3.13 (b).

Considering the possible excitation mechanisms responsible for the off-resonance cur-

rent observed: The 2D plasma excitations, excitons and optical phonons have much higher energy than 10 GHz, and hence can be excluded. The finite drain-source bias ($|V_{ds}| \approx 10 \mu\text{eV}$) is too small to provide the amount of energy, while the intrinsic excited states ($\Delta\epsilon^* \approx 120 \mu\text{eV}$) have higher energies. The observed off-resonance tunneling is attributed to acoustic phonon-assisted tunneling. Metallic Schottky gates on the surface of the piezoelectric GaAs crystal reduce the sound velocity near the gates. Thus two phonon cavities are formed by gates in the same area where the quantum dots are located. Each phonon cavity has a diameter about 800 nm (see the gate structures in Fig. 3.10). Electrons in the quantum dots which are only 90 nm below the surface are thus mainly coupled to local phonon modes in the cavities. In the absence of microwave radiation, a phonon mode in the cavities at about $f_{ph} \approx 10$ GHz is observed. This phonon mode slightly depends on the temperature, as shown in Fig. 3.13 (b), indicating that the phonon frequency is mainly determined by the size of the cavities although the phonons are thermally generated. Under microwave radiation with a constant bath temperature, the phonon mode in the cavities can be enhanced by external microwave field coupled to the piezoelectric GaAs crystal through the Schottky gates (see Sec. 5.2).

3. Transport Spectroscopy of Semiconductor Quantum Dots: Experiment

Chapter 4

Photon-Assisted Tunneling in Semiconductor Quantum Dots: Theory

Coulomb-blockade in quantum dots due to the charging effect can be overcome by tuning the gate voltage or the drain-source bias. Under the excitation of time-dependent electromagnetic fields, electrons in the contacts and in the dots can obtain an amount of energy compensating the Coulomb charging energy. The coupling between the electrons and the external field can be divided into two different regimes [KMM⁺97, Bue00]. One of the regimes is the low frequency regime, where the frequency of the external field is lower than the tunneling rate, i.e., $f \ll \Gamma$, so that electrons sense an rather static external field during the transport time which is mainly determined by the tunneling rates.¹ This is the so-called *adiabatic regime*, i.e., the external time-dependent field only shifts the electronic states adiabatically. When the field frequency is higher than the tunneling rate, $f \gg \Gamma$, electrons can feel the oscillating of the external field during the transport time. This is the so-called *non-adiabatic regime*, in which energy quanta ($n \times hf$) from the field can be absorbed or emitted by electrons, generating direct tunnel current (photocurrent). In this thesis, time-dependent transport in the non-adiabatic regime will be studied experimentally.

In quantum dots realized in AlGaAs/GaAs heterostructures, the relevant maximum energy is the charging energy (E_C) which is around 0.2 – 2 mV. The mean level spacing ($\bar{\Delta}$) is about 0.05 – 0.5 mV. The intrinsic level width ($\hbar\Gamma$) due to tunnel coupling with the contacts is tuned to be smaller than the mean level spacing so that discreteness of quantum states can be resolved. Especially in this thesis, the intrinsic level width

¹The net tunneling time spent by electrons to tunnel through a typical barrier is quite short (~ 2 ps) [BL82].

is even much lower than the temperature ($\hbar\Gamma \ll k_B T$). Hence, to observe the discrete quantum states, the temperature should be lower than the mean level spacing²: $3.52k_B T < \bar{\Delta}$. The discreteness of energy from the external electromagnetic field can be resolved in the non-adiabatic regime when $\hbar f > 3.52k_B T$. The involved photon energy is in the range from 0.05 mV to 2 mV, which corresponds to a frequency of 10 – 500 GHz. Hence, the external electromagnetic field with a millimeter-wavelength, i.e., microwave radiation, should be applied to quantum dots.

Under microwave radiation, both alternating (at high frequency) and direct tunnel current can be induced by time-dependent electric fields [Bue00]. In this thesis, only direct photocurrent will be considered, which can be measured experimentally. Photocurrent stems from inelastic electron tunneling induced by absorbing or emitting microwave photons. This non-linear transport is known as photon-assisted tunneling (PAT) [uJPG63, KMM⁺97]. Analogous to the light spectroscopy on real atoms, PAT is thought as *microwave spectroscopy* of “artificial atoms” by using microwave photons as the probe to reveal the internal excitation energy of quantum dots.

Theories on microwave spectroscopy of single quantum dots and coupled double quantum dots are briefly discussed in Sec. 4.1 and Sec. 4.2, respectively. The corresponding experimental results are shown in Chap. 5.

4.1 Photon-Assisted Tunneling through A Single Quantum Dot

When microwave radiation is applied to a single quantum dot, the resulting changes in phase coherence of electrons in the leads and dots have to be considered [WJM93, JWM94]. In practice, microwave excitation occurs in both the quantum dot and the contacts. Microwave induced ac-voltage drops across different tunnel barriers can be different in magnitude. Effectively, microwave excitation can be taken as it occurs only in the quantum dots and one of the contacts. Furthermore, Coulomb-blockade has to be taken into account. Different theoretical methods have been applied to understand PAT through single quantum dots, such as the master equation [BS94, OKK⁺96], and the nonequilibrium Green’s-function method [WJM93, SL97].

In 1960, Tien and Gordon studied the time-dependent tunneling between two superconductors separated by a tunnel barrier under microwave radiation [uJPG63]. The PAT picture developed by Tien and Gordon can be applied to explain many PAT experiments on quantum dots. This is mainly based on the fact that the nature of the

²The thermal energy can be characterized by the temperature broadening of a conductance peak, which is discussed in Sec. 2.2.

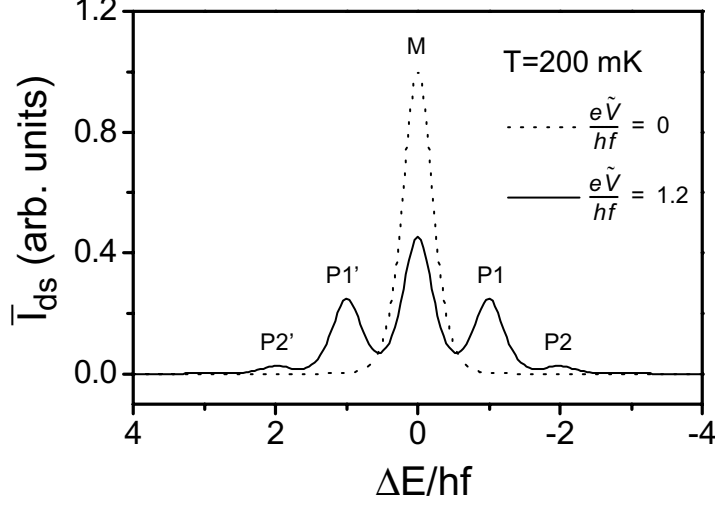


Figure 4.1: A simulation based on Eqs. [4.2, 4.3] shows the appearance of photon sidepeaks. The dotted line is the main resonant tunneling peak (M) in the absence of microwave radiation. Under microwave radiation ($e\tilde{V}/hf = 1.2$), the main peak (M) is reduced in magnitude and the photon sidepeaks (P1 (P1'), P2 (P2'), ...) at $\Delta E/hf = \pm 1, \pm 2 \dots$ appear on the left and right sides of the main peak (M).

transition between a discrete quantum state in the dot and the continuous states in the contacts can be described by *Fermi's golden rule* [Wal85]. The Tien-Gordon's PAT picture points out that the essential effect of the time-dependent ac-voltage drop across the tunnel barrier is to modify the static tunneling rate $\Gamma(E)$ according to

$$\tilde{\Gamma}(E) = \sum_{n=-\infty}^{+\infty} J_n^2(x) \Gamma(E + nhf), \quad (4.1)$$

where $J_n(x)$ is the n -th order Bessel function and $x = e\tilde{V}/hf$ with \tilde{V} the ac-voltage drop across the barrier. With $n = 0$, the tunneling corresponds to the elastic resonant tunneling. With positive (negative) n , electrons absorb (emit) $|n|$ photons, inducing photon sidebands at $E + nhf$. The Bessel function contribution to the PAT current can be understood in terms of "virtual states". The photon-induced virtual states at $E + nhf$ have the same spatial wave function as the unperturbed state at E , but have a different tunneling rate which is scaled by $J_n(x)$ as shown in Eq. [4.1]. Applying this picture to PAT through a single quantum state of a quantum dot in the linear regime ($e|V_{ds}| \ll \bar{\Delta}$), the photocurrent (\bar{I}_{ds}) can be obtained from the static $I_{ds}-V_g$ characteristic:

$$\bar{I}_{ds} = \sum_{n=-\infty}^{\infty} J_n^2\left(\frac{e\tilde{V}}{hf}\right) I_{ds}\left(V_g + \frac{nhf}{e\alpha}\right). \quad (4.2)$$

4. Photon-Assisted Tunneling in Semiconductor Quantum Dots: Theory

According to Eq. [2.24], the static $I_{ds}-V_g$ curve in the absence of microwave radiation is given by

$$I_{ds} = g_{max} V_{ds} \cosh^{-2} \left\{ \frac{-e\alpha(V_g - V_g^{\leftrightarrow})}{2k_B T} \right\}. \quad (4.3)$$

As shown in Fig. 4.1, a simulation of $\bar{I}_{ds}-V_g$ based on Eq. [4.2] is compared to the static curve based on Eq. [4.3], showing the photon sidepeaks (Pn') located at a distance of $\Delta E = -e\alpha(V_g - V_g^{\leftrightarrow}) = nhf$ to the main resonant tunneling peak (M).

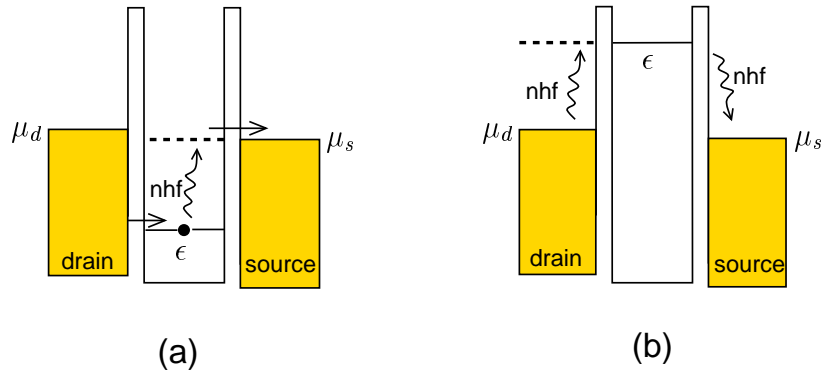


Figure 4.2: Level diagrams illustrate PAT through a single quantum dot. (a) A single photon is absorbed by an electron in the dot which is tunneling into the source contact, corresponding to P1 and P2 in Fig. 4.1. (b) A single photon is absorbed by an electron in the drain contact which is tunneling onto the dot, corresponding to P1' and P2' in Fig. 4.1. Both processes pump electrons from the drain to the source under a small negative drain-source bias.

Since the presence of Coulomb blockade and discrete quantum states in quantum dots, PAT through a quantum dot strongly depends on the charging energy and the level spectrum. The actual $\bar{I}_{ds}-V_g$ characteristic will be more complicated than that shown in Fig. 4.1. Usually, the charging energy is much larger than the applied microwave photon energy. But the photon energy can be comparable to the mean level spacing. When the photon energy absorbed is smaller than the excitation energy between the ground state and the lowest unoccupied excited state ($nhf < \Delta\epsilon^*$), only PAT through the ground state can be observed: Photon sidepeaks are located nhf from the main resonant tunneling peak, yielding the picture similar to that shown in Fig. 4.1. Photon-absorption processes induce the sidepeaks P1' and P2', which can be depicted in a level diagram shown in Fig. 4.2 (a). However, the pure photon emission process does not occur since the ground state is unoccupied when a near-zero bias is applied (see Fig. 4.2 (b)). Indeed, for example, the sidepeak (P1') observed stems from the tunneling of electrons in the drain contact by absorbing and re-emitting a single phonon³, as shown

³The electron can emit acoustic phonons as well.

in Fig. 4.2 (b). Only the quantum state is originally occupied, which requires a finite bias ($e|V_{ds}| > nhf$), pure photon-emission processes will happen.

Given the photon energy absorbed is larger than the first excitation energy ($nhf \geq \Delta\epsilon^*$), the excited state can participate in transport when it is empty and is aligned with the Fermi energies in the contacts, i.e., the ground state is $\Delta\epsilon^*$ below the Fermi energies and is occupied with an electron, as shown in Fig. 4.3. In the absence of microwave photons, electron tunneling is blocked due to the Coulomb blockade. However, as long as the ground state is depopulated by absorbing photons, tunneling through the excited state is enable, as shown in Fig. 4.3. This process is analogous to *photo-ionization*. Eq. [4.2] can not express this process since it is valid for the situations involving only one quantum state in transport. By applying the master equation method Oosterkamp *et al* well explained their experimental results of PAT through both the ground state and the excited state [OKK⁺96, OKAEAKH97]. Brune *et al* theoretically studied this process as well [BBS97]. This phenomenon will be discussed further in Sec. 5.1 and Sec. 5.3.

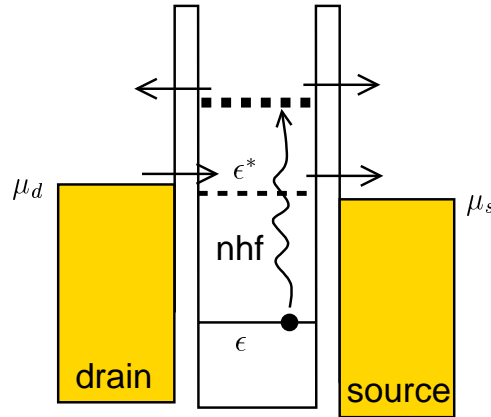


Figure 4.3: Tunneling through the excited state ϵ^* is enabled when the excited state is aligned with the Fermi energies μ_d or μ_s and the electron in the ground state ϵ is excited to a virtual state above the Fermi energies by photons. For this process, the photon energy absorbed should be larger than $\Delta\epsilon^* = \epsilon^* - \epsilon$.

In the linear transport regime, PAT reveals the ground state and excited states. In this sense, PAT is called as *microwave spectroscopy*, comparing to the *transport spectroscopy* by measuring the direct tunnel current or conductance in the absence of microwave radiation. A large drain-source bias will make the photocurrent peaks broadened and it becomes difficult to resolve PAT sidepeaks.

In the above discussion, only the microwave at a single frequency is applied to quantum dots. Two microwaves at different frequencies or broadband microwaves will be applied to quantum dots (see Sec. 5.3 and Sec. 5.4). In reality, broadband fluctuations can be black body radiation of the environment [HTL⁺94], electrical noise through the cables connecting the quantum dots with measurement setups [VOJ⁺95], and other excitations from the host crystal, e.g., phonons [FOvdW⁺00]. Taking into account the broadband fluctuations from the environment, the tunneling rate is modified according to

$$\tilde{\Gamma}(E) = \int_{-\infty}^{+\infty} d(hf) P(hf) \Gamma(E + hf), \quad (4.4)$$

where the weight function $P(hf)$ is the spectral density function for fluctuations in the environment [HO94]. In this thesis, both single microwave sources (see Sec. 5.1, Sec. 5.2, and Sec. 5.3) and broadband microwave sources (see Sec. 5.4) are applied to perform microwave spectroscopy on quantum dots.

4.2 Photon-Assisted Tunneling through A Double Quantum Dot

Given that microwave radiation is applied to a tunnel-coupled double quantum dot, transitions between the two quantum states (one in each dot) can be induced by microwave photons. Transport properties in this situation have been theoretically studied according to different tunnel coupling regimes. In the weak inter-dot tunneling regime, Stafford and Wingreen applied the Keldysh nonequilibrium Green function technique to reveal the coherent superpositions of quantum states under microwave radiation and the electron transport through the double dot [SW96]. Stoof and Nazarov studied both the weak and strong coupling regimes, however the results are restricted for double dots with large drain-source bias [SN96]. Sun *et al* considered the effects of both finite bias and the variation of tunnel coupling by using the nonequilibrium Green function method [SWL00]. Basic consistent results obtained from these works are briefly discussed below.

In this thesis, only the double quantum dot weakly coupled to the leads will be considered, as it has been discussed in Sec. 2.3. Two quantum states ϵ_L and ϵ_R form

the bonding and anti-bonding molecular states according to Eq. [2.56] and Eq. [2.57]. Only these two states participate in transport if the drain-source bias and the microwave photon energy is small comparing to the mean level spacing. Photon-induced transitions between the dot and the contacts are ignored and only the transitions between the dots are considered. The transition between two quantum states can not be described by Fermi's golden rule and hence the Tien-Gordon's PAT picture. Transitions are enabled by an electron in the bonding state absorbs microwave photons and is excited to the anti-bonding state.

The time-independent energy difference between the molecular states is

$$E_+ - E_- = \sqrt{(\delta E)^2 + 4t^2}, \quad (4.5)$$

where, $\delta E = \mu_L - \mu_R$ is the detuning between two decoupled quantum states of the two dots, t is the inter-dot tunneling matrix element. In the absence of microwave excitation, only when $\delta E = 0$ the wave functions on the two dots become completely delocalized. When a single electron is put on one of the dot, it will tunnel back and forth between the dots at the *Rabi frequency* of $\Omega_0 = 2t/h$. Tunneling through the double quantum dot is enabled when the bonding state is aligned with the Fermi levels in the drain and source contacts. For $\delta E \neq 0$, a single electron is mainly localized in one of the dot, e.g., in the left dot as shown in Fig. 4.4 (a) or in the right dot as shown in Fig. 4.4 (b). In this case, with the bonding state below the Fermi energies in the contacts electron transport through the double dot is not allowed. Only when the bonding state is aligned with the Fermi energies in the contacts, finite tunneling can be observed, which corresponds to the finite tunneling along the hexagon's boundaries in the charging diagrams, as shown in Fig. 2.9 and Fig. 3.11 (b).

With microwave radiation, transitions between the molecular states with $\delta E \neq 0$ can be realized if the photon energy is in resonance with the molecular states [SW96, SN96, SWL00]:

$$nhf = E_+ - E_- = \sqrt{(\delta E)^2 + 4t^2}. \quad (4.6)$$

At these n -photon resonance (schematically shown in Fig. 4.4) electron wave functions on two dots are completely delocalized, which is a result of the coherent superpositions of microwave photons and the two-level quantum system. With a near-zero bias applied, photon-assisted tunneling is induced by this coherent superposition (see Fig. 4.4 (a) and (b)), generating a positive and a negative tunnel current [SW96, SWL00]. Given a large bias is applied ($eV_{ds} > E_+ - E_-$), electrons can emit photons during tunneling through the double dot as well.

Stafford and Wingreen revealed the physics in a double quantum dot under microwave radiation in the weak tunnel coupling regime ($t \ll \delta E$, $E_+ - E_- \cong \delta E$). The state of the double dot at the n -photon resonance condition (defined by Eq. [4.6]) can be

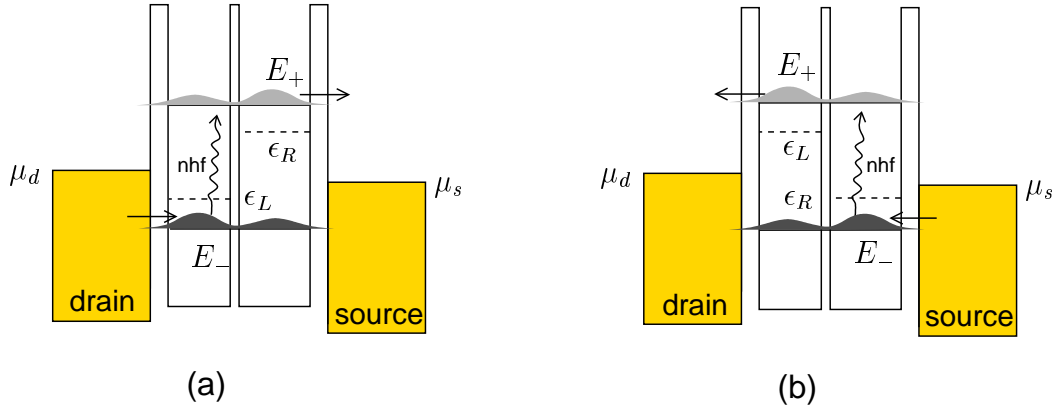


Figure 4.4: Level diagrams indicating the photon-assisted tunneling through a double dot in the linear transport regime. (a) a single photon is absorbed by an electron in the left dot which is tunneling into the right dot. (b) a single photon is absorbed by an electron in the right dot which is tunneling into the left dot. Both photon absorption processes occur in the quantum dots but not in the contacts. Electrons are pumped either from the drain to the source or vice versa.

described by a superposition of two quasi-eigenstates [SW96] which have an energy splitting of $2tJ_n(e\tilde{V}/hf)$. A single electron is completely delocalized between the quasi-eigenstates, oscillating at a Rabi frequency of $\Omega_R = 2tJ_n(e\tilde{V}/hf) \leq \Omega_0$. This behavior can be understood in terms of the hybridization of wavefunction on one dot with the wave function of the n -th photon sideband on the other dot. For example, when the n -th photon sideband of quantum state ϵ_L of the left dot matches the quantum state ϵ_R of the right dot, the inter-dot tunneling will hybridize the two states. The effective coupling between the wavefunctions is the product of t and the amplitude of the sideband $J_n(e\tilde{V}/hf)$. However, as pointed out before, the quasi-eigenstates are the coherent superpositions of the two-level system and the photons.

The average tunnel current induced by microwave photons has been obtained in different theoretical ways [SW96, SN96, SWL00]. The line shape of current peaks strongly depends on the relative magnitudes of three tunneling rates (Γ^L , Γ^t , and Γ^R). At low temperatures, the peaks usually have a Lorentzian line shape [SN96]. At higher temperature, under a near-zero bias, the main resonant tunneling peak (M) is temperature broadened. Given the photon-induced transitions occur only between the dots, the main peak measured in direction **A** in the $V_{gR} - V_{gL}$ plane can be approximated by $\cosh^{-2}(\delta\bar{\mu}/2k_B T)$. The main peak measured by varying only V_{gL} can be approximated by $\cosh^{-2}(\delta E/wk_B T)$ (refer to page 33). The photon sidepeaks should have smaller line width than that of the main peak, since the molecular states are located far below (above) the Fermi energies in the leads and hence the temperature broadening is suppressed [SN96, Kou95]. In this sense, it is easier to resolve PAT in a double dot

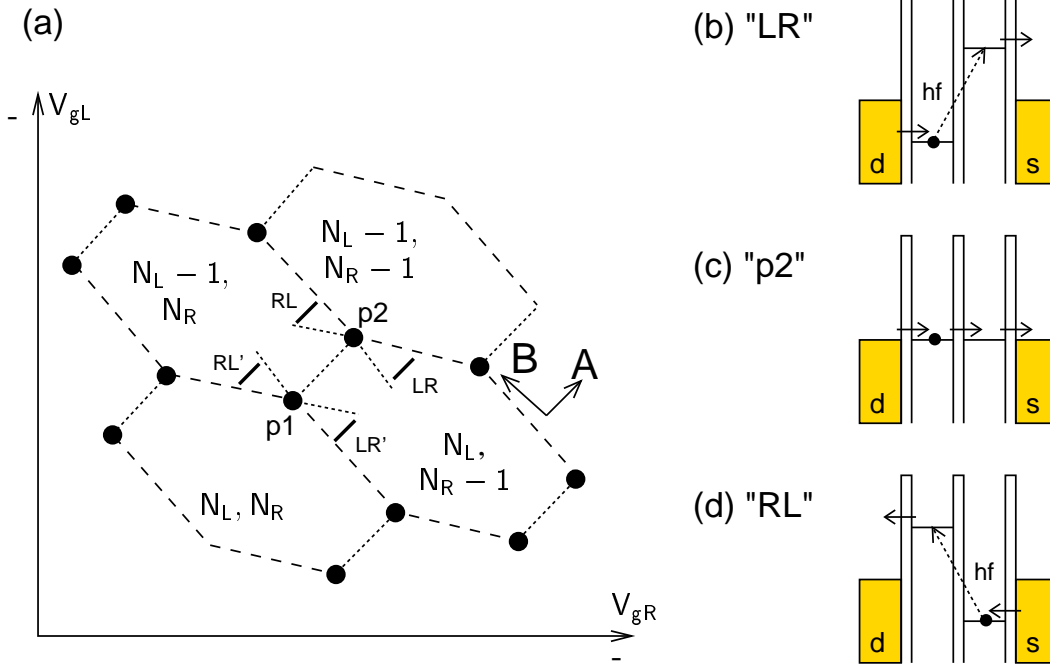


Figure 4.5: (a) Schematic charging diagrams of a double quantum dot in the weak tunnel coupling regime under microwave radiation. Peaks from the resonant tunneling through the double dot are those black dots at the crossing points ($p1$ and $p2$). Photon induced sidepeaks are solid lines labeled by "RL", "LR", "RL'", and "LR'". The level diagrams for the tunneling at "LR", "p2", and "RL" are illustrated in (b), (c), and (d), respectively.

rather than in a single quantum dot. However, microwave radiation normally increase the electron temperature and hence the peak broadening.

Experimentally, PAT through a double quantum dot can be observed by measuring the direct photocurrent. The most effective way is to map out a charging diagram from the photocurrent through the double dot under microwave radiation. Comparing to the charging diagram in the absence of microwave radiation (shown in Fig. 2.7 and Fig. 3.11 (a)), near the resonant tunneling peaks ($p1$ and $p2$), additional photon sidepeaks will appear when microwave radiation is applied to the double quantum dot (see Fig. 4.5).

Different to the resonant tunneling peaks ($p1$ and $p2$), photon sidepeaks have a smaller FWHM in the direction \mathbf{B} [SN96], but they are extended in direction \mathbf{A} , as shown in Fig. 4.5. As discussed before, a finite drain-source bias and temperature will increase the peak broadening in direction \mathbf{A} . At a certain high temperature, the crossing points $p1$ and $p2$ will be too close to each other to be distinguished. The photon sidepeaks "RL" ("LR") and "RL'" ("LR'") will overlap in the charging diagram. Transport

through double quantum dots have been studied earlier by Blick *et al* [BHvKE96] and by Fujisawa *et al* [FT97], where PAT sidepeaks are observed in charging diagrams.

In Sec. 5.2, microwave spectroscopy is applied to a tunnel-coupled double quantum dot which has been characterized in Sec. 3.3. PAT through coherent molecular states are observed. Furthermore, the interaction of molecular states with acoustic phonons are revealed.

Chapter 5

Microwave Spectroscopy of Semiconductor Quantum Dots: Experiment

Transport spectroscopy of quantum dots in the linear regime mainly reveals the ground states. Under microwave irradiation, Coulomb-blockade of electron transport through the ground state can be removed by electrons absorbing or emitting microwave photons, i.e., finite tunneling current can be observed within the CB regimes. Furthermore, even under a near-zero drain-source bias, transport through excited states assisted by microwave photons can be enabled. Measurements of PAT is what the microwave spectroscopy mainly performs. Microwave spectroscopy is an extension of transport spectroscopy in the linear regime. Most importantly, microwave spectroscopy allows to excite electrons from the ground state to excited states, and the resulting dynamic relaxations of electron within the dot or into the leads can be studied.

Under a large drain-source bias, straightforward microwave spectroscopy by measuring the direct tunnel current encounters the same difficulty as what the transport spectroscopy has: no clear PAT through ground states or excited states will be resolved since the peaks are broadened. To overcome this obstacle, new techniques are applied in this thesis. By coupling two coherent microwave sources with a slight frequency offset, a flux of microwave photons is generated, whose amplitude varies in time with the offset frequency. The resulting alternating tunnel current at the offset frequency can be detected using a lock-in amplifier. Since two microwave sources are phase locked, the time base for both the photon flux and the resulting tunnel current is known. This heterodyne scheme allows for detection of complex photocurrent: Both the amplitude and relative phase can be obtained. The amplitude reflects the tunneling strength. The relative phase between the incident photon flux and the induced tunnel current indicates

the time involved in the transport through the quantum dot, which reveals the dynamic relaxations of electrons. In comparison to straightforward microwave spectroscopy, this technique is called *heterodyne microwave spectroscopy* in this thesis.

In Sec. 5.1, microwave spectroscopy is performed on a small single quantum dot in the few electron limit by measuring the direct tunnel current under continuous microwave radiation. In Sec. 5.2, microwave spectroscopy on a double-dot molecule is presented. In Sec. 5.3, heterodyne microwave spectroscopy is applied on a few-electron single dot. Different to the above three sections where microwave spectroscopy is performed with only a single microwave source or two sources with a slight frequency offset, a broadband heterodyne microwave spectroscopy is performed on a small quantum dot in Sec. 5.4.

5.1 Photon-Assisted Tunneling in A Single Quantum Dot

As shown in Fig. 5.1, by properly applying negative voltage on the gates #10, #9, #8, #16, #18 and #13, a single quantum dot is realized from the structure (QD-sample#2) shown on page 114 in App. A. The 2DEG is about 45 nm below the surface. At 4.2 K, the sheet electron density and electron mobility are $n_s \approx 2 \times 10^{11} \text{ cm}^{-2}$ and $\mu_e \approx 8 \times 10^5 \text{ cm}^2/\text{Vs}$, respectively. The lithographic dot diameter is about 200 nm. The quantum dot is coupled to leads #1 and #4, which serve as the drain and source contacts. The other gates are not used and hence are grounded to reduce electronic noise. Keeping the voltage on the gate #13 fixed, the tunnel barriers coupling the dot to the source and drain are controlled by the gate voltages V_g on gate #10 and V_3 on gate #18. Additionally, V_g is also used as the plunger gate voltage to control the dot potential. Gate voltages V_1 and V_2 control the dot shape.

The measurements shown below are conducted at a bath temperature of $T_b = 200 \text{ mK}$. The electron temperature is found in equilibrium with the bath temperature: $T \approx T_b$. To improve the dot shape, a small magnetic field of 1 Tesla is applied perpendicular to the plane of 2DEG. From transport spectroscopy, basic electronic structure of the quantum dot is obtained (CB diamonds are not shown here). The dot exhibits an excited state at $\Delta\epsilon^* \approx 250 \text{ } \mu\text{eV} \approx 60 \text{ GHz}$ above the ground state. The addition energy is $E_{add} \approx 1.6 \text{ meV}$. Taking the charging energy $E_C = e^2/C_\Sigma \approx 1.35 \text{ } \mu\text{eV}$, the total dot capacitance is estimated as 120 aF. Given the dot is a disk, the dot diameter yields 260 nm. On the other hand, the dot diameter, estimated from $\Delta\epsilon^* \approx \bar{\Delta} \approx 2\hbar^2/m^*r^2 \approx 250 \text{ } \mu\text{eV}$, is about 140 nm. Both the above estimations have deviations from the lithographic size. An averaged diameter of about 200 nm can be obtained, corresponding to less than 60 electrons in the dot. The voltage-to-energy conversion factor for V_g

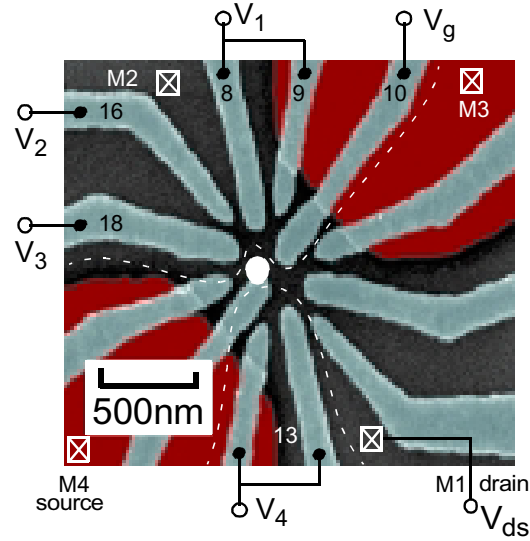


Figure 5.1: Formation of a single quantum dot from QD-sample#2 (see page 114 in App. A for details). The ohmic contacts #1 and #4 serve as the drain and source contact, respectively. The gate voltages V_1 , V_2 and V_4 are fixed at -500 mV, -450 mV and -460 mV, respectively. The tunnel barrier between the dot and the source contact is fixed by gate voltage $V_3 = -334$ mV. The gate voltage V_g tunes the dot potential and forms the tunnel barrier between the dot and the drain. The dashed lines sketch the edge of 2DEG. $T = 200$ mK, $B = 1$ T.

is $\alpha = 8 \times 10^{-2}$, by which the gate voltage is converted into the energy distance by $\Delta E = -e\alpha(V_g - V_g^{\leftrightarrow})$, where V_g^{\leftrightarrow} is the position of the zero-bias resonance.

To radiate the quantum dot, a microwave signal supplied by an AGILENT8360B synthesizer is fed through a coaxial line of the sample holder into the dilution refrigerator. The coaxial line is terminated by the antenna shown in Fig. B.3 (b) (see details on page 118 in App. B). In this setup, the quantum dot is located nearly in the center of the antenna. Under microwave radiation the electron temperature is increased from 200 mK to 270 mK (corresponding to a FWHM about $3.52k_B T \approx 80$ μ eV). Frequencies are carefully tuned from 20 GHz to 50 GHz so that heating and a rectified current are minimized. The simple antenna proved to be a good microwave source.

In Fig. 5.2 (a) and (b), the direct tunnel current is plotted versus the gate voltage under radiation of 35.8 GHz and 40.2 GHz, respectively. The applied drain-source bias is $+30$ μ eV, which is much smaller than $\Delta\epsilon^*$, $k_B T$ and E_C . Under such a small positive bias, electrons tunnel from the source to the drain. Beside the main resonant tunneling peak (M), additional sidepeaks (P1, P1', and P2) are clearly observed. On the right side of the main peak, the ground state is below both the Fermi energies of the drain and source contacts. On the left side of the main peak, however, the ground state is located above the Fermi levels. The sidepeaks P1(P1') and P2 correspond to

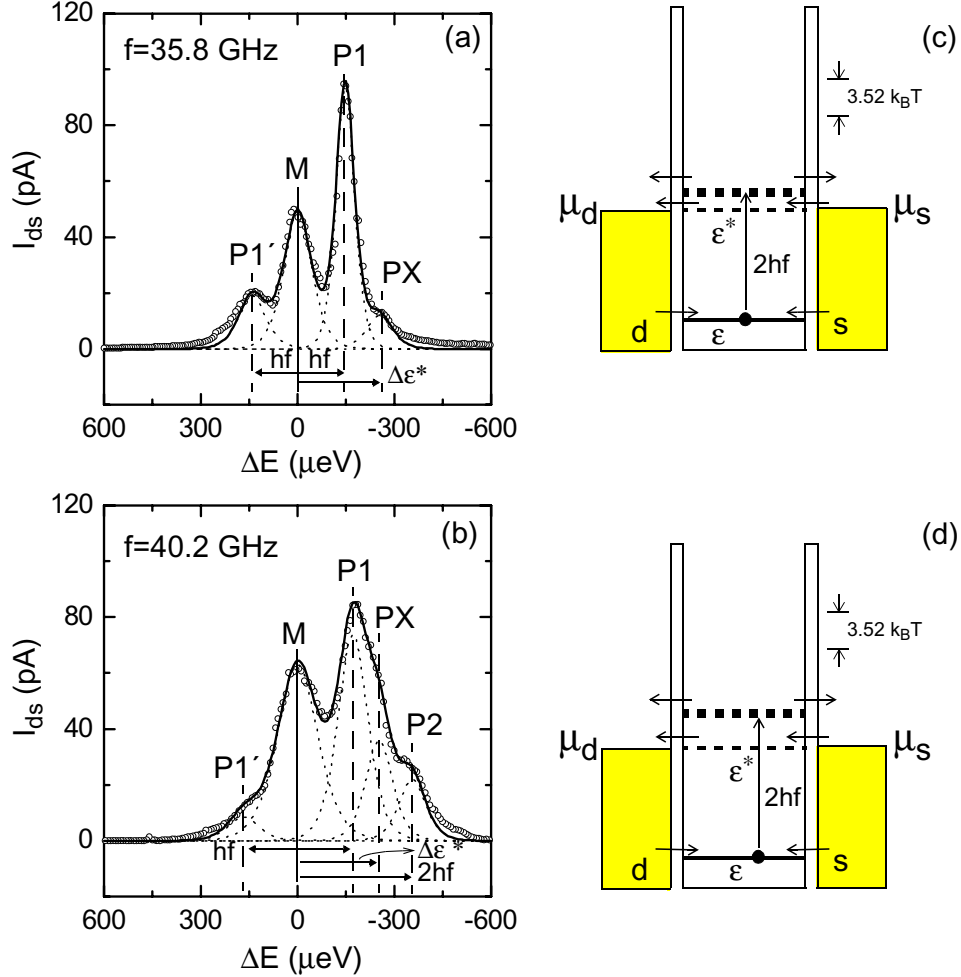


Figure 5.2: Direct tunnel current through the dot under microwave radiation of 35.8 GHz (a) and 40.2 GHz (b). The peaks labeled as M, P1(P1') and P2 are the main peak, one-photon sidepeak and two-photon sidepeak, respectively. The peaks marked by PX stem from resonant tunneling through an excited state, which is enabled by two-photon-assisted tunneling through the ground state. (c) and (d) correspond to the level diagrams for the sidepeak PX shown in (a) and (b), respectively. $T = 270$ mK, $B = 1$ T, $V_{ds} = +30$ μV .

the photon-assisted tunneling by absorbing one photon and two photons, respectively. More specifically, P1 (P2) results from electrons absorbing microwave photons in the dot and tunneling to the drain contact. Differently, P1' corresponds to electrons in the source contact absorbing one photon and tunneling onto the dot. Similar level diagrams are shown in Fig. 4.2 (a) and (b) where a small negative drain-source bias is

applied.

The sidepeaks (PX) shown in Fig. 5.2 stem from a more complicate process. The distance between the main peak and the sidepeak (PX) is constant ($\approx 250 \mu\text{eV}$) for both $f = 35.8 \text{ GHz}$ and $f = 40.2 \text{ GHz}$. This energy scale is in accordance with the energy of the excited state ($\Delta\epsilon^* \approx 250 \mu\text{eV} \approx 60 \text{ GHz}$). At the sidepeak (PX), the excited state is aligned with the Fermi levels, while the ground state is below the Fermi level, as illustrated by the level diagrams in Fig. 5.2 (c) and (d). Electrons in the ground state are excited to an intermediate virtual state by absorbing two photons and then leaking out of the dot. For both frequencies applied, the two-photon energies exceed the energy required for exciting an electron from the ground state to the excited state: For $f = 35.8 \text{ GHz}$, $2f = 71.6 \text{ GHz}$ is slightly higher than 60 GHz , while for $f = 40.2 \text{ GHz}$, $2f = 80.4 \text{ GHz}$ is about 20 GHz higher than 60 GHz . In both cases, the residual energy is comparable to the thermal broadening. This residual energy can be transferred in two ways: The electrons relax into the contacts by emitting phonons. On the other hand, the electrons can relax into the real excited state and then tunnel out into the contacts or simply relax into the ground state. In the former case, as long as the ground state is depopulated, tunneling through the excited state is enabled, which is otherwise blocked by Coulomb-blockade. Electron transport in this case consists of two parts: Inelastic two-photon absorption by an electron in the ground state and elastic resonant tunneling through the excited state. This phenomenon, in analogy to photo-ionization of real atoms by light, was observed earlier by Oosterkamp et al. [OKAEAKH97]. Electron transport through the dot is partly incoherent since relaxation processes are involved. Both relaxation processes discussed above are possible and can compete with each other. Partly due to this competition process, the relative amplitude between PX and P1 varies at different microwave frequencies, as shown in Fig. 5.2 (a) and (b).

In another small quantum dot in the few-electron limit (see Sec. 5.3), sidepeaks (PX) are observed and are much stronger than the one-photon sidepeaks (P1), indicating a much stronger coupling between the excited state and the contacts. Charge relaxations in this structure will be studied in detail using a new technique in Sec. 5.3.

To verify the non-adiabatic transport induced by photons, both the microwave-power-dependence and the frequency-dependence of the peak height and peak position are examined. As an example at $f = 35.8 \text{ GHz}$, the power-dependence of the sidepeaks are shown in Fig. 5.3. In Fig. 5.3 (a), the peak distances from P1, P1', and PX to M are independent from the microwave power applied. The power dependence of the peak heights of M, P1 and PX at 35.8 GHz are shown in Fig. 5.3 (b).

For the main peak, it is fitted with $A_0 J_0^2(x)$. Accordingly, $A_1 J_1^2(x)$ and $A_2 J_2^2(x) + A_2' J_0^2(x) J_2^2(x)$ are used to fit sidepeaks P1 and PX, respectively. The argument is $x = eV_{mw}/hf$ and V_{mw} stands for the amplitude of the oscillating field induced by

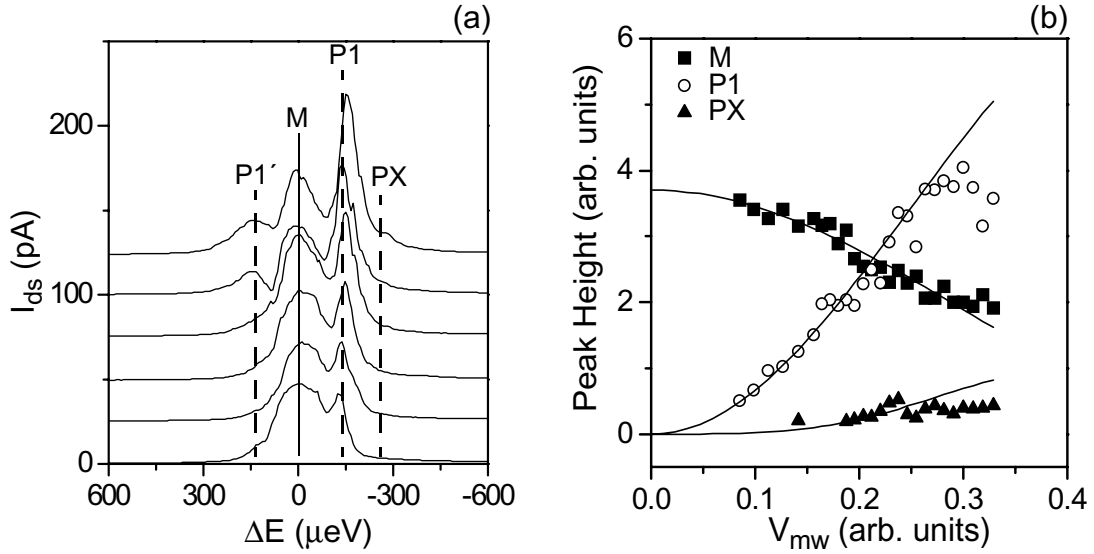


Figure 5.3: Under the microwave radiation at 35.8 GHz, (a) single traces revealing sidepeaks P1, P1' and PX are plotted at different microwave powers applied. From bottom to top, the microwave power increases from -15 dBm to -10 dBm in steps of 1 dBm. (b) The power dependence of the peak heights of sidepeaks M, P1, and PX. $T = 270$ mK, $B = 1$ T, $V_{ds} = +30$ μV .

microwave radiation.¹ The prefactors A_i (A'_i), $i = 0, 1, 2$, are different for different indices: $A_0 \approx 3.7$, $A_1/A_0 \approx 5.4$, $A_2/A_0 \approx 6.8$, and $A'_2/A_0 \approx 8.1$. The increase of the prefactor for higher index, indicates that a larger tunneling rate is involved for a photon sideband at higher energy. Such a power dependence is also found in another quantum dot presented in Sec. 5.3.

In Fig. 5.4, the distance between sidepeaks at different frequencies is plotted. The distance between M and P1(P1') fits into one photon energy:

$$\Delta E = -e\alpha\Delta V_g = hf. \quad (5.1)$$

Accordingly, the distance of sidepeak P2 is about the energy of two photons. The distance between M and PX is fixed around the energy of the excited state ($\Delta\epsilon^* \approx 250$ μeV). Clear sidepeaks PX are observed only at two frequencies. For frequencies lower than 30 GHz, two photons are not sufficient to induce transport through the excited state. For frequencies above 60 GHz, it is expected that it is sufficient to see the sidepeak PX with only one-photon excitation. Since the maximum frequency can be

¹ V_{mw} in arbitrary units is obtained from the microwave power (P_{mw}) in units of dBm according to $V_{mw} \propto 10^{P_{mw}/2}$.

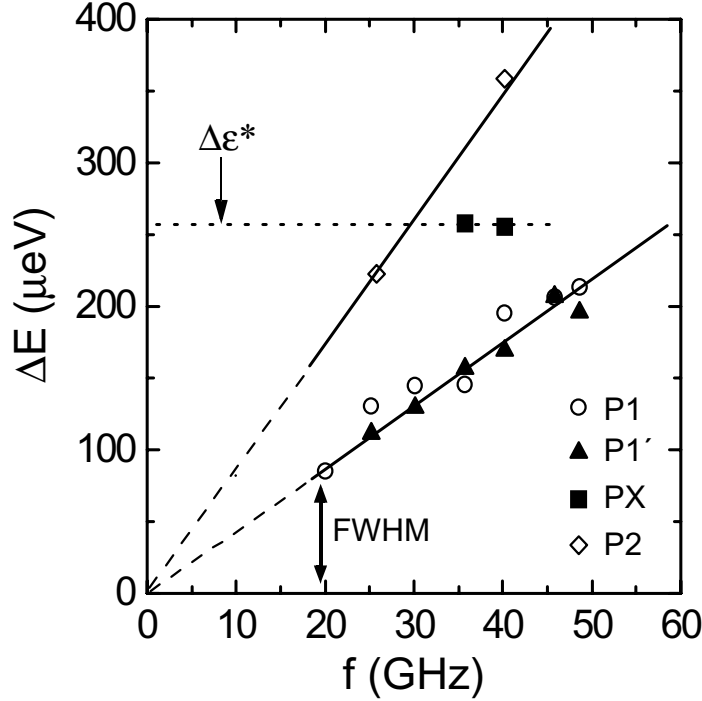


Figure 5.4: The peak distance between the main peak (M) and the sidepeaks ($P1$, $P1'$, PX and $P2$) is evaluated at different microwave frequencies applied. The FWHM ($\approx 3.52k_B T$) is the full-width-at-half-maximum of the resonant tunneling peak (M). This energy scale marks the lower limit for the applied microwave frequency (~ 20 GHz) below which PAT can not be resolved. $T = 270$ mK, $B = 1$ T, $V_{ds} = +30$ μ V.

reached with an AGILENT8360B synthesizer is 50 GHz, transport above $f = 50$ GHz is not studied for this quantum dot. As discussed above, other possible microwave-induced transport, e.g., adiabatic pumping and rectification, can be ruled out.

5.2 Microwave Spectroscopy of A Double Quantum Dot

In this section, microwave radiation is applied to a double quantum dot which has been characterized by transport spectroscopy in Sec. 3.3. The double dot is weakly coupled to the drain and source contacts and hence the dephasing due to the contacts is minimized. Microwave photons become resonant with the bonding and anti-bonding molecular states when $nhf = E_+ - E_-$. According to Eq. [2.58], under a fixed

microwave frequency this resonance can be reached by varying the detuning between two decoupled quantum states (ϵ_L and ϵ_R) of the left and right dot: $\delta E = \mu_L - \mu_R \propto V_{gL}$ (see Eq. [2.47]).

The experiments are conducted in a $^3\text{He}/^4\text{He}$ dilution refrigerator with a bath temperature of $T_b = 140$ mK, while the electron temperature saturates at $T = 170$ mK. No external magnetic field is applied. The microwave radiation is supplied by a microwave synthesizer (HP83711A) and fed through the coaxial cable of the sample holder to a Hertzian wire-loop antenna (shown in Fig. B.3 (a) on page 119), which is about 1 cm above the double quantum dot. Microwave frequencies in the range from 1 GHz to 20 GHz are chosen in a way so that the microwave-induced heating and rectification current are minimized.

As discussed in Sec. 3.3, acoustic phonons in the phonon cavities induce off-resonance tunneling, i.e., acoustic phonon-assisted tunneling. The phonon cavity is formed by Schottky gates which introduce boundaries for acoustic phonons since the sound velocity in piezoelectrical GaAs crystal below the gates is reduced. The phonon mode observed without microwave radiation in Sec. 3.3 is thermally activated. However, the phonon frequency ($f_{ph} \approx 10$ GHz) is mainly determined by the cavity size and boundary conditions of the cavity. The Schottky gates not only confine electrons in the quantum dots but also confine acoustic phonons in the phonon cavities. Under microwave radiation, oscillating microwave field can be coupled to these Schottky gates and excite nonequilibrium phonons, i.e., the Schottky gates form a piezoelectrical resonator. One of the possible mechanisms for generating phonons by microwave radiation is as follows: The gates serve as interdigitated transducers (IDTs), which are commonly used to launch surface acoustic waves [WSW⁺89]. Assuming a 2D sound velocity of $v_{2D} \approx 2800$ m/s and the corresponding phonon wavelength $\lambda_{IDT} \sim 800$ nm (about two times the gate period [WSW⁺89], see Fig. 3.10), the phonon frequency at resonance is about $f = v_{2D}/\lambda_{IDT} \approx 3.5$ GHz. Due to the limited number of gates in comparison to conventional IDTs this ‘‘Schottky-gate’’ transducer possesses a large bandwidth. Hence, exciting this transducer at resonance will also generate phonons at $f_{ph} \approx 10$ GHz in the cavity. However, this mechanism requires that the parity of electrical field on the gates are modulated by the gates themselves. Given that the electrical field is uniformly distributed among the gates, the surface potential of the GaAs crystal is oscillating driven by microwave radiation. It is still possible to generate nonequilibrium phonons. As long as microwave field is effectively coupled to GaAs host crystal by Schottky gates, the confined phonon mode in the cavity is enhanced. As will be shown below, strong photon-sidepeaks shifted by $f_{ph} = 10$ GHz are observed in the microwave frequency range from 1 to 6 GHz.

Most importantly, the phonons generated by microwave field are naturally coherent with the microwave photons. With the excitation of both acoustic phonons and microwave photons, coherent transition between the bonding and anti-bonding molecular

states will be studied below.

The tunnel coupling between the dots is characterized by the tunnel conductance (G_c) of the central tunneling barrier which can be measured directly. Strictly speaking, the exact tunnel conductance of the central barrier is difficult to obtain since it is always influenced by the bias on neighboring gates. A simple approach to get a crude value for G_c is to measure the influences from the other gates separately and then take a sum of them. Also, the tunnel coupling can be characterized by the tunneling strength t , which is proportional to the conductance G_c .

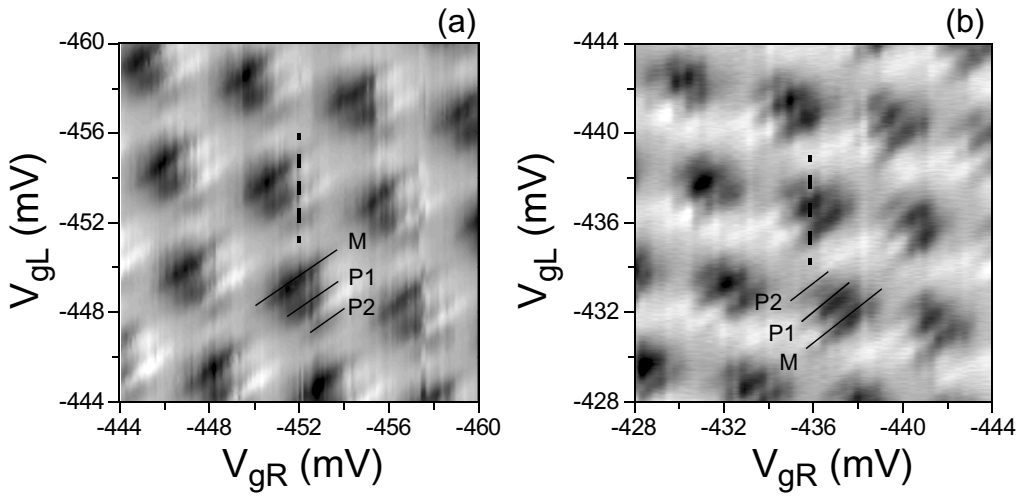


Figure 5.5: Under microwave radiation of $f = 20$ GHz, the charging diagrams (current) are measured with small (a) negative ($V_{ds} = -30 \mu\text{eV}$, black: $I_{ds} < 1.3 \text{ pA}$, white: $I_{ds} > -0.6 \text{ pA}$) and (b) positive ($V_{ds} = +30 \mu\text{eV}$, black: $I_{ds} > -1.9 \text{ pA}$, white: $I_{ds} < -0.5 \text{ pA}$) drain-source bias. The one-photon sidepeak (P1) and two-photon sidepeak (P2) are located beside the main peak (M). $G_c \approx 0.08e^2/h$, $T = 170 \text{ mK}$.

PAT under a weak inter-dot coupling

As a starting point, PAT through the double dot with a weak inter-dot tunnel coupling ($G_c \approx 0.08e^2/h$) is studied. Under such a weak tunnel coupling, the hybridization of two quantum states is weak: $E_+ - E_- \cong \delta E$, and the wavefunctions of two states are localized in the respective dots. As shown in Fig. 5.5 (a) and (b), two charging diagrams are obtained under microwave radiation at 20 GHz. In the charging diagrams, the main resonant tunneling peak at $\delta E = 0$ is marked as M, the one- ($\delta E = hf$) and two-photon ($\delta E = 2hf$) absorption sidepeaks are labeled as P1 and P2, respectively.

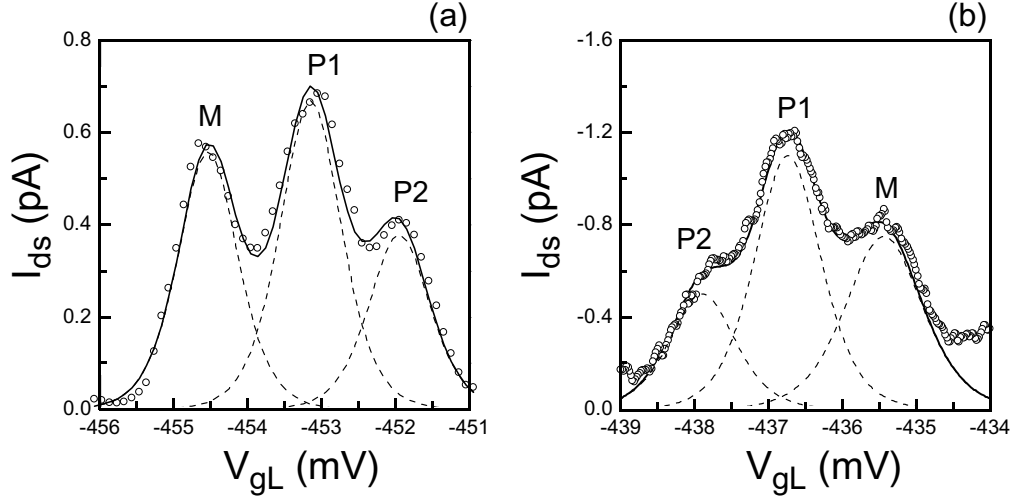


Figure 5.6: Single traces (a) and (b) are extracted from the charging diagrams, at constant V_{gR} marked by the dashed lines as shown in Fig. 5.5 (a) and (b), respectively. The solid curve is a fit with three $\cosh^{-2}((\delta E - nhf)/wk_B T)$ -shaped peaks with $w \approx 2.3$ (as shown by the dashed curves), where $n = 0, 1, 2$ corresponds to M, P1 and P2, respectively.

The charging diagrams (a) and (b) are measured under the same circumstances except that the respective drain-source bias² are $V_{ds} = -30 \mu\text{eV}$ and $V_{ds} = +30 \mu\text{eV}$. When the opposite bias is applied, photon sidepeaks are located on the opposite side of the main peak, as shown in the diagrams. Under a negative bias, electrons tunnel from the drain to source contact, i.e., the left quantum state is lower than the Fermi level in the drain reservoir and the right quantum state is located above the Fermi level in the source contact, as shown in Fig. 4.4 (a). Viceversa, under a positive bias the left (right) quantum state is located above (below) the Fermi level in the drain (source) reservoir.

To clarify the photon-induced transitions between the dots, single traces are extracted from the diagrams (see Fig. 5.6). The single traces are approximated by three peaks, i.e., $\sum_{n=1}^3 \cosh^{-2}[(\delta E - nhf)/wk_B T]$ with $w \approx 2.3$. Peaks with $n = 0$, $n = 1$, and $n = 2$ are the main peak, the side peak P1 and P2, respectively. A similar charging diagram is obtained under microwave radiation of 15 GHz, as shown in Fig. 5.7. The fit shows a good agreement with the experimental data.

Since the FWHM of the main peak corresponds to a detuning of around 14 GHz, for microwave radiation below $f = 10$ GHz one-photon induced sidepeaks will not be well resolved. However, very strong sidepeaks with much larger peak distances than

²With such a small but finite bias applied, no strong opposite pumping current is observed in this double quantum dot.

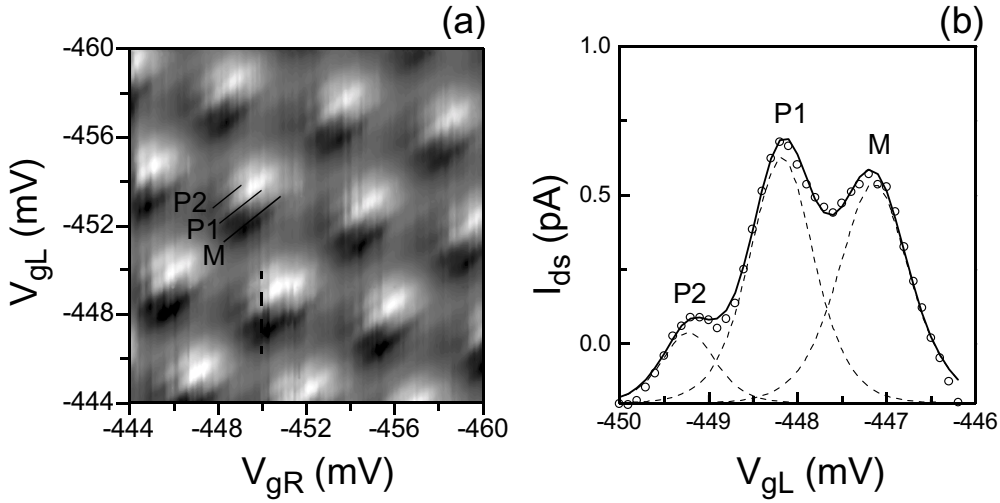


Figure 5.7: (a) The charging diagram (black: $I_{ds} < 2.8$ pA, white: $I_{ds} > -1.8$ pA) obtained under the microwave radiation of $f = 15$ GHz. (b) A single trace extracted from (a) at the position marked by a dashed line shows the details of the main peak (M), one-photon (P1) and two-photon (P2) sidepeaks. The solid curve is a fit with three $\cosh^{-2}((\delta E - nhf)/wk_B T)$ peaks with $w \approx 2.3$ (as shown by the dashed curves), where $n = 0, 1, 2$ corresponds to M, P1 and P2, respectively. $G_c \approx 0.08e^2/h$, $V_{ds} \approx +10$ μeV , $T = 170$ mK.

the one-photon energy are indeed observed with microwave radiation below 10 GHz. In Fig. 5.8, charging diagrams are obtained under (a) 5.9 GHz, (b) 4.5 GHz and (c) 3 GHz, and (d) 1.9 GHz. The power dependence of peak distances shows that the observed sidepeaks result from non-adiabatic absorption of photons rather than other adiabatic effects or rectification of microwave field. By extracting single traces from the diagrams, details are revealed: As shown in the right panels of Fig. 5.8, clear sidepeaks labeled as S2 are observed for all frequencies. The “hidden” sidepeaks S1 can be revealed by approximating the data with $\cosh^{-2}(\delta E/wk_B T)$ -shaped peaks for all frequencies as shown in Fig. 5.8.

In Fig. 5.9, the energy difference (δE) between the two decoupled quantum states at the sidepeaks is plotted versus the microwave frequency applied. Three different regions are classified: The regions above 10 GHz, between 8 GHz and 10 GHz, and below 8 GHz. Above 10 GHz, where two sidepeaks corresponding to the one-photon (P1) and two-photon (P2) absorption processes are observed, the detuning is approximated by the relevant photon energy:

$$\delta E^{P1} = hf, \quad (5.2)$$

$$\delta E^{P2} = 2 \times hf, \quad (5.3)$$

for the sidepeak P1 and P2, respectively. This dependence is well understood within

5. Microwave Spectroscopy of Semiconductor Quantum Dots: Experiment

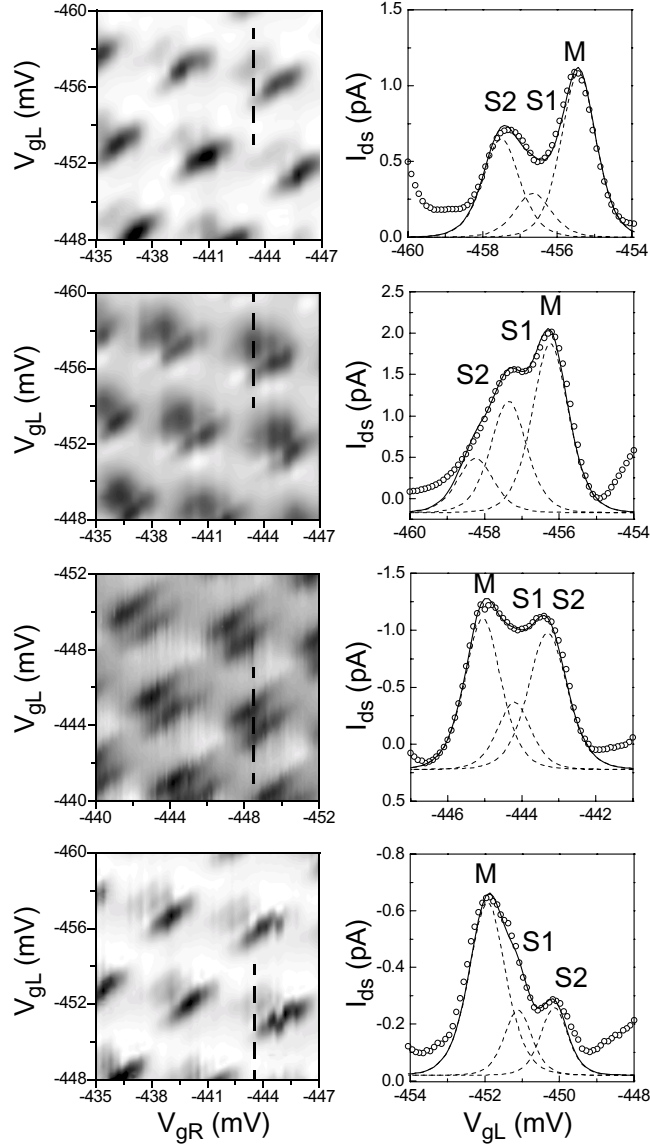


Figure 5.8: Charging diagrams (current) obtained under microwave radiation of 5.9 GHz (a, black: -3 pA, white: -0.05 pA), 4.5 GHz (b, black: -2.8 pA, white: $+0.3$ pA), 3 GHz (c, black: $+1.6$ pA, white: -0.7 pA) and 1.9 GHz (d, black: $+2.7$ pA, white: $+0.02$ pA). Single traces are extracted from respective charging diagrams at a constant V_{gR} marked by dashed lines in the charging diagrams. The solid curves are a sum of three $\cosh^{-2}(\delta E/wk_B T)$ -shaped peaks with $w \approx 2.3$, as shown by the dashed curves corresponding to M, S1 and S2. The relative position of sidepeaks to the main peak is determined by the parity of the applied drain-source bias ($|V_{ds}| \sim 10$ μ V): For a positive (negative) bias, the sidepeaks are on the right (left) side of M. $G_c \approx 0.08e^2/h$, $T = 170$ mK.

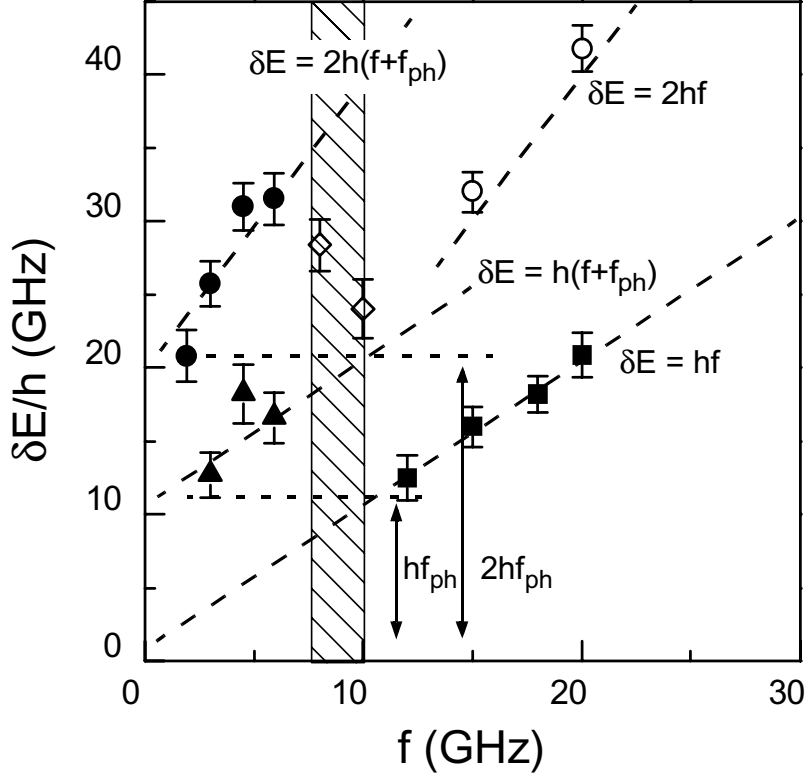


Figure 5.9: The detuning of two quantum states at sidepeaks P1, P2, S1 and S2 versus microwave frequency in the weak tunnel coupling regime ($G_c \approx 0.08 e^2/h$) at a temperature of $T = 170$ mK. $f > 10$ GHz: Solid squares and open circles are for sidepeaks P1 and P2, respectively. $f < 8$ GHz: Solid triangles and solid circles stand for sidepeaks S1 and S2, respectively. In the hatched region (8 GHz – 10 GHz), the open diamonds correspond to sidepeaks S2.

the picture of PAT through two decoupled quantum states. Below 8 GHz, the detuning at the sidepeaks S1 and S2 follows,

$$\delta E^{S1} = hf + hf_0, \quad (5.4)$$

$$\delta E^{S2} = 2 \times (hf + hf_0), \quad (5.5)$$

respectively, with a constant offset $f_0 \approx 10$ GHz. The slopes of the above relations correspond to absorption of one and two photons. The offset, however, indicates that transport through the dots involves not only pure photon absorption processes but also another absorption process of hf_0 or $2hf_0$. Both electronic excitations from the drain

and source leads ($eV_{ds} \approx -10 \mu\text{eV} < 3 \text{ GHz}$) and the intrinsic excitations in the dots ($\Delta\epsilon^* \approx 120 \mu\text{eV} \approx 30 \text{ GHz}$) can be excluded from inducing this offset energy. The offset energy quanta in Eqs. [5.4,5.5] is attributed to be acoustic phonons at $f_{ph} \approx f_0 \approx 10 \text{ GHz}$ as has been discussed earlier in this section and has been observed in Sec. 3.3. Generated by microwave radiation and are confined in phonon cavities, the phonons are coherent with microwave photons.

PAT under strong inter-dot couplings

Under excitation of both microwave photons and acoustic phonons, it is of great interest to verify the formation and persistence of coherent molecular states, since a long lifetime for coherent states is essentially important for quantum computation in quantum dots [LD98, Lan96]. For this purpose, charging diagrams under microwave radiation are measured at different tunnel coupling strengths. From these charging diagrams, the coupling dependence of the detuning of two quantum states at the photon sidepeaks is obtained. As shown in Fig. 5.10 (a), we find that at $f = 20 \text{ GHz}$ and $f = 15 \text{ GHz}$ the detuning at sidepeak P_1 follows the well-known relation (refer to Eq. [4.6])

$$\delta E^{P_1} = \sqrt{(hf)^2 - 4t^2}. \quad (5.6)$$

Eq. [5.6] is a signature of a coherently coupled two-level system as studied before [OFvdW⁺98, SW96, SN96], indicating that the superpositions of the molecular states are realized in the double dot.

Commonly, one expects no coherent superposition of the molecular states below $f = 8 \text{ GHz}$ since the thermal fluctuation is comparable to the photon energy. Nevertheless, the coupling dependence obtained at $f = 3 \text{ GHz}$ turns out to be quite different: Due to the participation of both photons and phonons the detuning at resonance is larger than without phonons, i.e., the influence of thermal fluctuation can be suppressed. Furthermore, the detuning at resonance decreases as the coupling of the two dots is enhanced (see Fig. 5.10 (a)), behaving like Eq. 5.6.

Considering the dynamics of electron transport at 3 GHz , the processes of phonon and photon absorption between the dots could be coherent as well as sequential. The first sequential process to be considered is the following: Phonon absorption occurs within the single dots exciting an electron into an intermediate state, while photon absorption couples the two dots, i.e.,

$$\delta E^{S_2} = \sqrt{(2hf)^2 - 4t^2} + 2hf_{ph}, \quad (5.7)$$

depicted by the dashed curve in Fig. 5.10 (a), which is obviously not observed.³ The

³Here we only show the coupling dependence of the detuning at sidepeak S_2 , since it has smaller error than that at sidepeak S_1 .

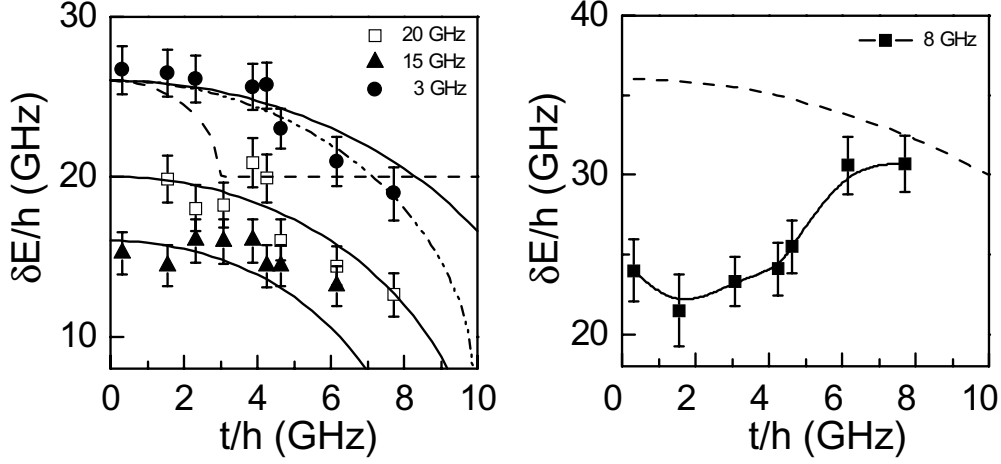


Figure 5.10: (a) The coupling dependence of the detuning at sidepeaks P1 and S2 at 20 GHz, 15 GHz, and 3 GHz. For 20 GHz and 15 GHz, the solid lines corresponds to Eq. [5.6]. For 3 GHz, the dashed line is from Eq. [5.7], the dashed/dotted line is fitted with Eq. [5.8], and the solid line is based on Eq. [5.9]. (b) At 8 GHz, the dashed curve is calculated from Eq. [5.9]. $T = 170$ mK.

other sequential process is given by the absorption of photons in the dots but the dots are coupled by phonon absorption. The corresponding coupling dependence follows

$$\delta E^{S_2} = \sqrt{(2hf_{ph})^2 - 4t^2} + 2hf, \quad (5.8)$$

depicted by the dashed/dotted trace in Fig. 5.10 (a), which is in reasonable agreement with the experimental data. On the other hand, assuming coherent photon and phonon generation by the microwave source, an electron tunneling coherently between the dots can absorb both photons *and* phonons. The coupling dependence is then written as

$$\delta E^{S_2} = \sqrt{[2hf + 2hf_{ph}]^2 - 4t^2}, \quad (5.9)$$

illustrated by the solid curve for $f = 3$ GHz in Fig. 5.10 (a). Within the error bars also this process can be assumed. The coherent absorption of both two-phonons and two-photons by an electron can be viewed as a two-quanta absorption process, while the sequential absorption is a four-quanta process, which has an even smaller probability. The observed strong sidepeaks S_1 and S_2 at 3 GHz, 4.5 GHz, and 5.9 GHz imply coherent absorption of both microwave photons and acoustic phonons. In other words, the coherent superposition of two molecular states are not demolished by ab-

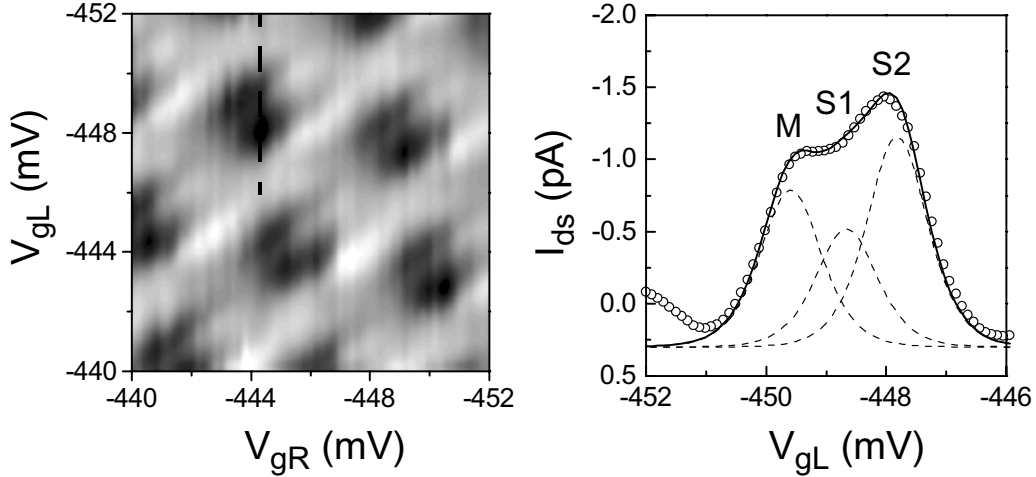


Figure 5.11: Charging diagrams (black: $I_{ds} < 1.5$ pA, white: $I_{ds} > -0.7$ pA) obtained under microwave of $f = 8$ GHz. The solid curves is a fit by three $\cosh^{-2}(\delta E/2k_B T)$ -shaped peaks, as shown by the dashed curves corresponding to M, S1, and S2. $V_{ds} \sim -10$ μ V, $G_c \approx 0.08e^2/h$, $T = 170$ mK.

sorbing acoustic phonons, which is in agreement with the recent theoretical prediction by Smirnov *et al.* [SHM00].

The hatched area in Fig. 5.9, marks a transition region between 8 GHz and 10 GHz. An increase of the coupling at $f = 8$ GHz requires a larger detuning for resonance (see Fig. 5.10 (b)). Probably due to the complexity of the phonon generation in the cavities by the external microwave, no simple superposition of photon and phonon exists in this region.

Recently, Fujisawa *et al.* found that at low temperatures vacuum fluctuations induce pronounced transitions between energetically well-separated quantum states, generating discrete phonon modes in a tunnel-coupled double quantum dot under a large bias [FOvdW⁺00, FvdWK00]. The emitted phonons belong to confined phonon modes in phonon cavities as well. The limitation of an applied large bias, however, is that no coherent molecular states can be probed by pure transport spectroscopy.

In summary for this section, we connect two quantum dots of medium size and probe the coherent superpositions of two molecular states under near-zero bias by using microwave spectroscopy. The applied microwave radiation introduces coherent microwave photons and acoustic phonons. Apart from conventional photon-assisted tunneling (PAT) observed above $f = 10$ GHz, we find a coherent superposition of photon- and phonon-assisted tunneling below $f = 8$ GHz. These induced tunneling processes

stem from the superposition of molecular states by both microwave photon and acoustic phonon excitation.

5.3 Heterodyne Detection of Photon-Assisted Tunneling in A Single Quantum Dot

As shown in Sec. 5.1, clear PAT through ground states and excited states can be found in microwave spectroscopy in the linear regime. Microwave spectroscopy is a complementary tool for transport spectroscopy. However, when the quantum dot is probed in nonlinear transport, photon-induced features in direct tunnel current or conductance are masked by broadened resonances. In this section, heterodyne detection of PAT is applied to study the dynamics of electron transport through single quantum dots. It further allows to resolve photon-induced features in both the nonlinear regime.

As the term “heterodyne” suggests, two microwave sources are tuned to have a frequency offset (intermediate frequency). The setup is schematically shown in Fig. 5.12 (a): Two microwave synthesizers (HP83711A) are phase locked and tuned at f_1 and $f_2 = f_1 + \delta f$ with $\delta f \ll f_1, f_2$, respectively. The microwaves are added with a power combiner. Then the output from the combiner is fed to a frequency multiplier.⁴ The frequency multiplier generates microwaves with frequencies $2f_1$, $f_1 + f_2$ and $2f_2$, which can be passed through the band-pass filter. Since these frequency components have a rigid phase relation, their superposition leads to a modulated microwave signal with the modulation frequency at δf . The microwave signal is finally fed through the coaxial line of the sample holder and irradiated onto the sample using a Hertzian wire-loop antenna (see Fig. B.3 (a) on page 119) located at a distance about 1 cm from the sample. The coupling of microwaves is proved to be best at the chosen frequency $f \cong 2f_1$, while at other available frequencies a considerable heating is observed.

We have thus produced a flux of photons with a one-photon energy $hf \cong 2hf_1$ whose intensity varies periodically in time with the frequency of δf , as shown in Fig. 5.12 (b). The alternating tunnel current (photocurrent) induced by these photons is recorded using a lock-in amplifier. Thus, the detected signal is solely due to the irradiation and contains no dc contribution. It is therefore possible to observe PAT even in the nonlinear regime. Furthermore, since the microwave sources are phase locked, i.e., coherent, the microwave radiation at f and the flux signal at only δf are strictly synchronized with a stable time base. For a normal amplitude-modulated microwave source, e.g., by a PIN-diode, no such synchronization can be obtained. As a result, another

⁴It is not necessary for this technique to have the frequency multiplied. Since no clear PAT is observed below $f = 20$ GHz and the microwave synthesizer (HP83711A) has a maximum frequency output at 20 GHz, we double the microwave frequency.

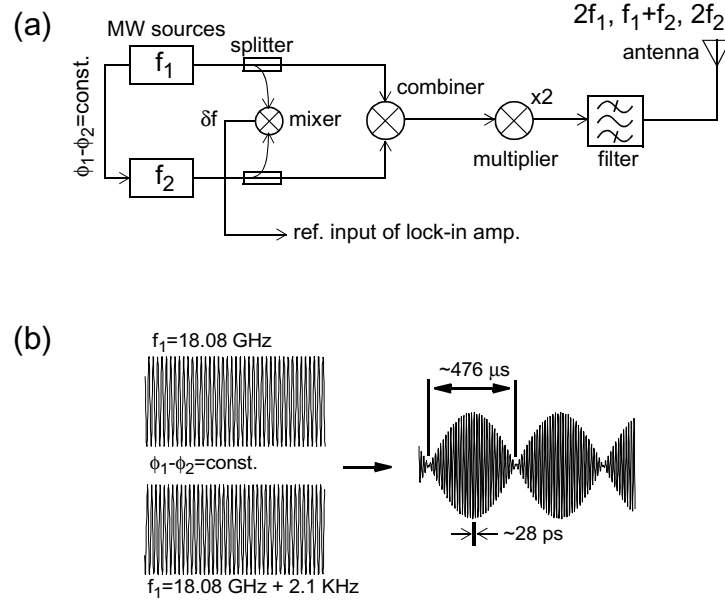


Figure 5.12: (a) A schematic setup for generating a microwave flux from two phase-locked microwave sources. (b) The wave forms illustrate the formation of microwave flux.

advantage of this heterodyne technique is that it allows to determine the relative phase between the photocurrent signal and the incident photon flux [QBK⁺01]. The relative phase is a measure of the time spent by electrons to tunnel through the dot, which provides information on the dynamics of electron transport. The full measurement setup is described in Fig. B.5 (a) on page 122. In the experiment shown below, two lock-in amplifiers are used to detect the in-phase (γ_0) and out-of-phase ($\gamma_{\pi/2}$) components of the photocurrent, from which the amplitude (A) and the relative phase (Φ) of the photocurrent are deduced: $A = \sqrt{\gamma_0^2 + \gamma_{\pi/2}^2}$, $\Phi = \arctan(\gamma_{\pi/2}/\gamma_0)$ for $\gamma_0 \geq 0$ and $\Phi = \pi + \arctan(\gamma_{\pi/2}/\gamma_0)$ for $\gamma_0 < 0$, respectively.

The single quantum dot under study is realized from QD-sample#3 described on page 115 in App. A.⁵ As shown in Fig. 5.13, patterned split gates are adopted to selectively deplete the 2DEG below the gates. A small island of 2DEG is formed and connected to the left (drain) and right (source) large areas of 2DEG only via tunnel barriers. With the gate #2 biased at -41 mV, the dot is mainly defined by gate #1. The gate #1 is used as the plunger gate to tune the dot's potential as well. From the geometry, the dot diameter is estimated to be about 140 nm. At a low temperature of 4.2 K, the

⁵With different gate voltages confining the quantum dot, Kondo resonances were observed in this sample by Simmel *et al* [SBK⁺99].

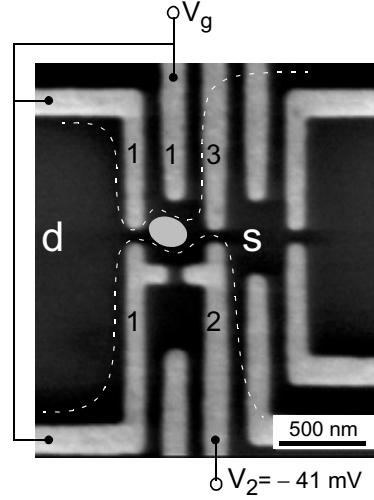


Figure 5.13: Gates labeled as #1 are connected together to serve as the plunger gate. Gate #2 is biased at -41 mV. The other gates are grounded. The dashed lines schematically show the edge of 2DEG, forming a small quantum dot with a diameter of about 140 nm. $T = 140$ mK, $B = 1$ T.

heterostructure used has a sheet electron density of $n_s \approx 1.6 \times 10^{11} \text{ cm}^{-2}$ and an electron mobility of $\mu_e \approx 8 \times 10^5 \text{ cm}^2/\text{V s}$. In order to improve the dot shape, a magnetic field of 1 T is applied perpendicular to the plane of 2DEG. The sample is located in a dilution refrigerator with a bath temperature of 140 mK. The dot radius is thus estimated to be $r = 70$ nm, i.e., the quantum dot contains only about 20 electrons.

The electronic structure of the dot is first characterized by transport spectroscopy, i.e., by measuring the Coulomb-blockade oscillations in conductance and forming CB diamonds in the absence of microwave radiation. As shown in Fig. 5.14, the quantum dot conductance in the vicinity of a resonance is plotted as a function of the drain-source bias V_{ds} and plunger gate voltage V_g . For convenience, the plunger gate voltage is rescaled into $\Delta E = -e\alpha\Delta V_g$, which is the energetic distance to the ground state resonance at $V_{ds} = 0$. The factor α can be obtained from the boundary slopes of the CB diamond (refer to Eq. [2.20]). The transformation of V_g to ΔE allows for a direct extraction of excitation energies from the conductance plot as shown in Fig. 5.14. At zero bias, a positive (negative) ΔE means that the ground state is located above (below) the Fermi levels in the drain and source contacts.

From the zero-bias distance between two adjacent conductance peaks the total capacitance of the quantum dot is estimated to be $C_\Sigma = 85$ aF, which corresponds to a charging energy of $E_C \approx 1.9$ meV $\gg k_B T$. As shown in Fig. 5.14, the ground-state resonance splits by $e|V_{ds}|$ at a finite bias (marked by “gd” and “gs”, standing

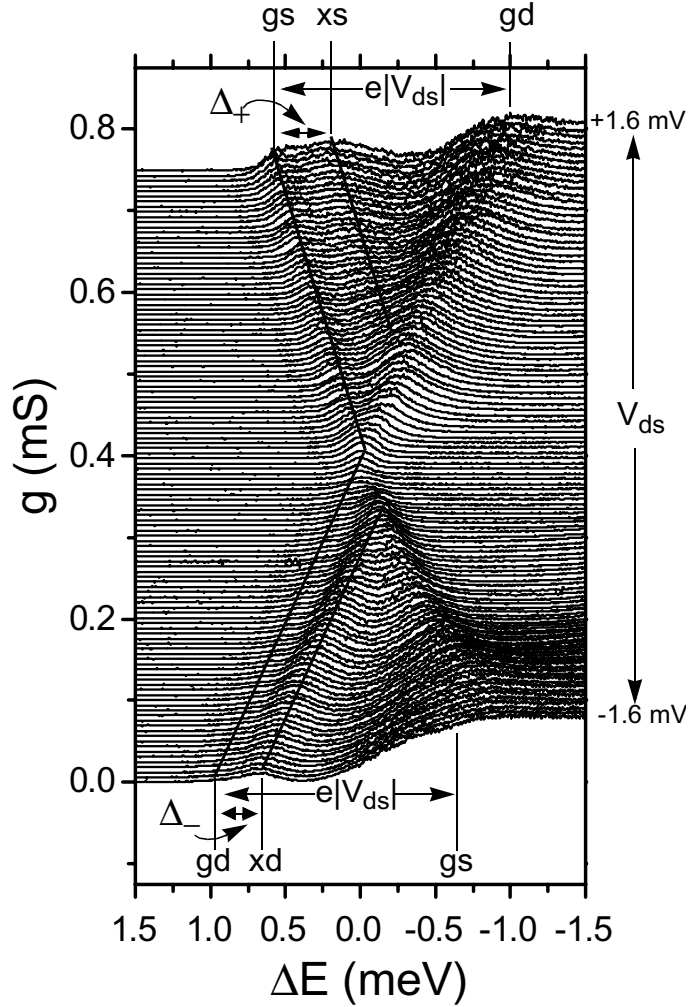


Figure 5.14: The dot's conductance in the vicinity of a single resonance: The drain-source bias is varied from $V_{ds} = -1.6$ mV (bottom) to $V_{ds} = +1.6$ mV (top) in 120 steps. The horizontal axis is the distance $\Delta E = -e\alpha\Delta V_g$ from the zero-bias ground state resonance (see text). The single resonance at $V_{ds} = 0$ splits into two resonances ("gd" and "gs") separated by $e|V_{ds}|$. Additional resonances ("xs" and "xd") stem from excited states of the quantum dot Δ_+ and Δ_- above the ground state, respectively. The symbols are defined in the text. $T = 140$ mK, $B = 1$ T.

for the drain- and source-related resonance of the ground state, respectively.). For $V_{ds} > 0$, an excited state located $\Delta_+ = 390$ μeV above the ground state is found. For $V_{ds} < 0$, an excited-state resonance is found at a distance $\Delta_- = 280$ μeV above the ground state. These excitation energies are comparable to the mean level spacing $\bar{\Delta} \approx 2\hbar^2/m^*r^2 \approx 470$ μeV . Hence, two different excited states take part in transport

5.3. Heterodyne Detection of Photon-Assisted Tunneling in A Single Quantum Dot

for $V_{ds} > 0$ and $V_{ds} < 0$. Furthermore, the drain-related ground state resonance “gd” is almost suppressed for $V_{ds} < 0$, whereas the excited-state resonance “xd” is much stronger. The strength of these resonances are related to the spatial overlap between the wavefunction of the corresponding quantum state and the wavefunctions in the contacts. Hence, the variation in conductance indicates that the coupling of the ground state to the drain contact is much smaller than that of the excited state for $V_{ds} < 0$. This phenomenon was also observed by Weis et al [WHvKP93] and is observed in Fig. 3.8 (d) on page 46. In this case, it is found that the coupling of the excited state to contacts is about 5.3 times the coupling of the ground state.

The CB diamond shown in Fig. 5.14 reveals the basic electronic structure of the dot. The following characteristic properties of transport are identified. The charging energy is much larger than the mean level spacing ($E_C = e^2/C_\Sigma \gg \bar{\Delta}$). The temperature is low so that $k_B T \ll \bar{\Delta}$. Single-electron tunneling through single discrete quantum levels is observed and the conductance resonances show temperature broadened peaks, indicating that the quantum levels have an intrinsic level broadening much lower than the temperature ($\hbar\Gamma \ll k_B T \ll \bar{\Delta}$). The excited states (Δ_+ and Δ_-) can be attained by electrons absorbing one or a few photons if the microwave frequency f is chosen so that $n\hbar f \sim \bar{\Delta} \approx \hbar \times 70$ GHz.

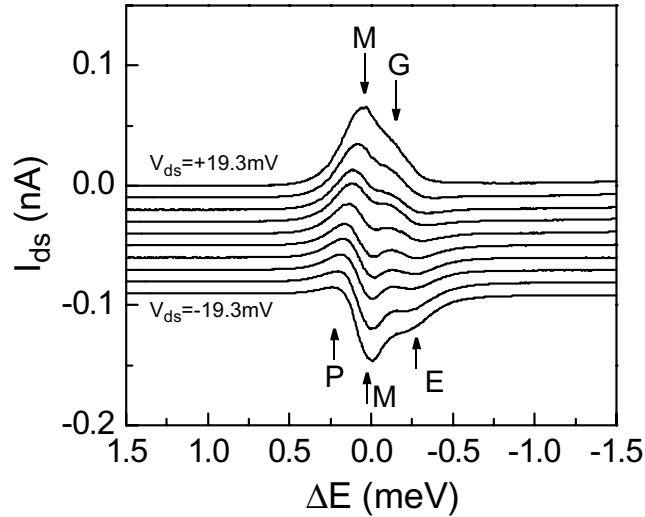


Figure 5.15: Direct current through the quantum dot for small bias values under irradiation with microwaves at $f = 36.16$ GHz and a power of -12 dBm. The drain-source bias is varied from $+19.3 \mu\text{V}$ to $-19.3 \mu\text{V}$ in nine equal steps. Next to the main ground state resonance (M) additional features (G, P, E) appear which can be ascribed to PAT through the ground state, photon-induced pumping and tunneling through an excited state (see text). $T = 140$ mK, $B = 1$ T.

5. Microwave Spectroscopy of Semiconductor Quantum Dots: Experiment

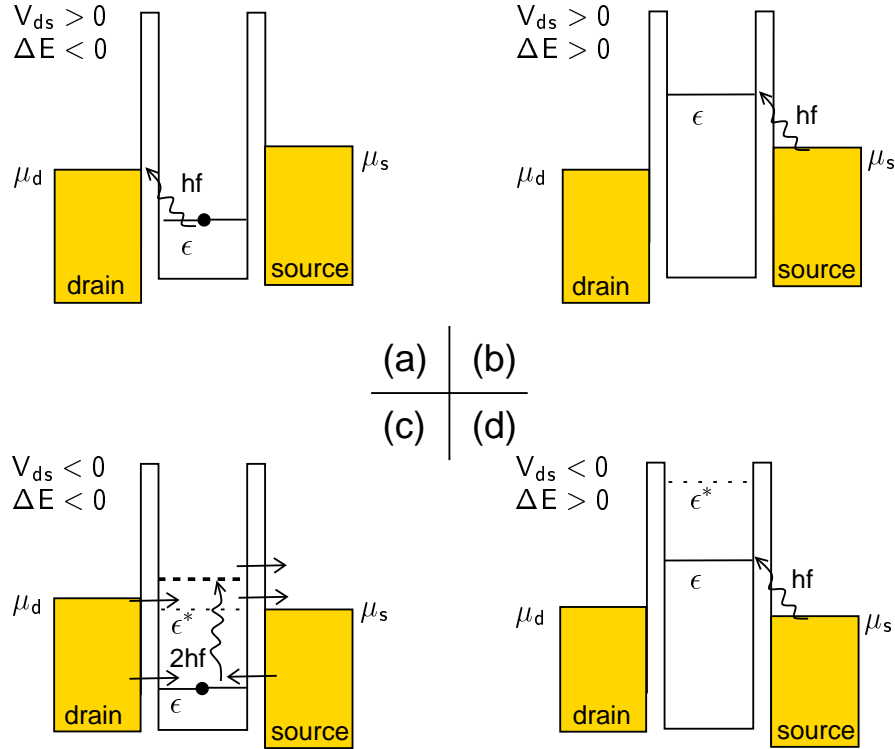


Figure 5.16: Schematic representation of the photon-induced processes involved in Fig. 5.15: In the case of positive bias (a, b), only PAT through the ground state is possible. For $V_{ds} < 0$, the excited state is approximately two photon energies above the ground state and tunneling through which can be enabled by absorption of two photons (c). Furthermore, due to the asymmetry in microwave absorption across the tunneling barriers, a pumping current can occur (d) for $V_{ds} < 0$ (see text).

Before we apply the heterodyne detection of photocurrent, the straightforward microwave spectroscopy is used, i.e., direct current through the dot with a near-zero bias $V_{ds} \sim 0$ is measured under the radiation from a single microwave source. The microwave radiation is originally generated using the same setup as shown in Fig. 5.12 (a), but the second microwave source is switched off: The microwave signal from a single microwave synthesizer ($f_1 = 18.08$ GHz) is frequency-doubled ($f = 36.16$ GHz) and filtered using a band pass filter with center frequency at 32 GHz. The induced direct tunnel current is recorded. The result is shown in Fig. 5.15, where the current through the quantum dot is displayed for small bias ranging from $-19.3 \mu\text{V}$ to $+19.3 \mu\text{V}$.

For small positive bias the original main peak from the ground state resonance (M) as well as a sidepeak (G) in a distance $hf \approx 0.15$ meV are detected. This sidepeak in the current signal is due to PAT through the ground state, which is illustrated in Fig. 5.16

(a): At low positive bias only the ground state transition occurs. The first excited state ($\Delta_+ = 390 \mu\text{eV} \approx 94 \text{ GHz}$) for this bias direction is too far above the ground state to be accessible by a one- or two-photon process ($\Delta_+ > 2hf$). The other possible photon-induced ground state transition ($\Delta E > 0$) shown in Fig. 5.16 (b) is not detected in the low-bias current signal. However, it is resolved for larger bias values applying the heterodyne detection scheme (see below). Quite differently, for negative bias different features (marked by P and E) in the current signal are induced by the microwave radiation. These features can be attributed to resonant tunneling through the excited quantum state (E) and photon-induced pumping (P) through the ground state, which are schematically depicted in Fig. 5.16 (c) and (d), respectively. The excited state at $\Delta_- = 280 \mu\text{eV} \approx 67.6 \text{ GHz}$ above the ground state can participate in transport when the ground state is depopulated by a two-photon absorption process ($2hf \gtrsim \Delta_-$), a process analogous to photo-ionization [OKAEAKH97]. This phenomenon is also observed in the sample QD-sample#2 as shown on page 70 in Sec. 5.1. A few charge relaxation processes are possibly involved in this process: Excited by two photons to an intermediate virtual state slightly higher than the excited state, a single electron can tunnel and relax directly from the virtual state into the contacts. As long as the ground state is depopulated, electron in the drain contact can tunnel through the excited state. On the other hand, the single electron in the virtual state has the possibility to decay to the excited state or relax back to the ground state, i.e., relaxation within the dot. Electrons in the contacts can refill the ground state as well. Different processes involve a different relaxation time. Since tunneling through the excited state is correlated to the two-photon absorption process, the tunnel current through the excited state might have a much smaller probability than a pure two-photon process: According to the Tien-Gordon picture [uJPG63], the probability of a pure two-photon process is proportional to $A_2 J_2^2(x)$ and the probability of a correlated excited state resonance and a two-photon process is proportional to $A'_2 J_0^2(x) J_2^2(x)$, where $x = eV_{mw}/hf$ and V_{mw} is the microwave amplitude across the tunnel barriers.⁶ However, since the coupling of the excited state to the contacts is more than four times stronger than the coupling of the ground state, the correlated process might turn out to be comparable to the pure two-photon PAT in amplitude. A pumping current flows opposite to the bias direction for $\Delta E > 0$, where the ground state is hf above the Fermi level in the source contact (see Fig. 5.16 (d)). This only happens when the microwave absorption across the right tunnel barrier is larger than that of the left tunneling barrier [SL97]. In this case, the ground state is permanently populated with electrons from the source contact which then partly decays into the drain region.

Photon-induced features similar to our results have been reported before [OKAEAKH97] and explained theoretically using, e.g., nonequilibrium

⁶ V_{mw} in arbitrary units is obtained from the microwave power (P_{mw}) in units of dBm according to $V_{mw} \propto 10^{P_{mw}/2}$.

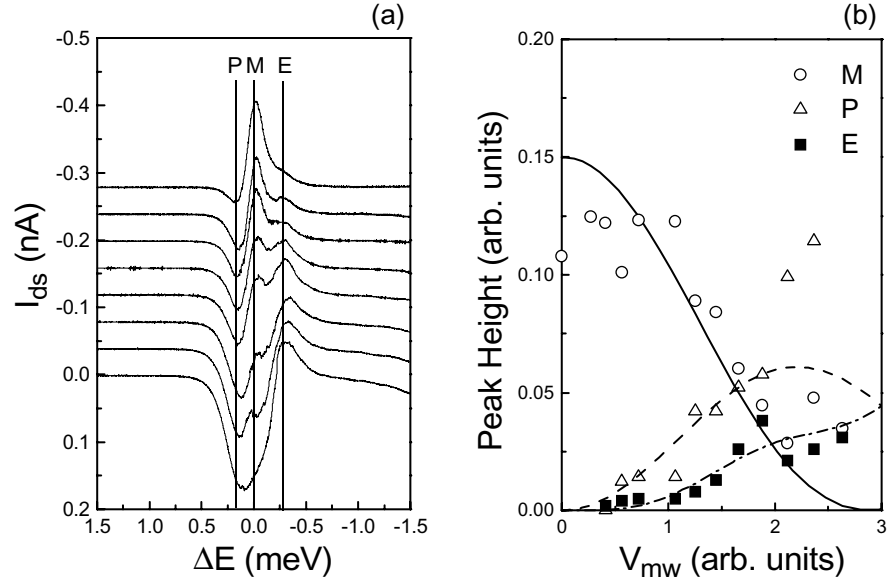


Figure 5.17: (a) Single traces are measured at $V_{ds} = -5.1 \mu\text{V}$ under different microwave power. The output power of the microwave source is increased from top to bottom in a step of 0.5 dBm. The main resonant tunneling (M), pumping through the ground state (P) and the resonant tunneling through the excited state (E) are marked, respectively. (b) The power dependence of tunneling amplitude of M, P and E. For the resonant tunneling through the ground state (M), it is fitted with $A_0 J_0^2(x)$ (solid curve), where $x = eV_{mw}/hf$ and V_{mw} is the microwave amplitude across the tunnel barriers. For the pumping current through the ground state (P), it is fitted with $A_1 J_1^2(x)$ (dashed curve). For the sidepeak E, it is fitted with $A_2 J_2^2(x) + A_2' J_0^2(x) J_2^2(x)$.

Green-function techniques [SL98]. However, to ensure that the observed features are not adiabatic effects of the microwave irradiation (e.g., rectification effects) [WHvKE95] commonly both their frequency and power dependence should be determined. From the power dependence, we confirm that the pumping current results from PAT. Fig. 5.17 shows the power dependence of the photon-induced features for $V_{ds} = -5.1 \mu\text{V}$. The output power of the microwave synthesizers is increased for curves from top to bottom in a step of 0.5 dBm. Over this wide power range the photon-induced features do not change in position, indicating that they are indeed induced by single photons. We find that the observed dependence of peak heights on microwave power roughly agrees with the Bessel function behavior: For the main resonant tunneling peak (M), the amplitude is fitted by $A_0 J_0^2(x)$ (the solid curve in Fig. 5.17 (b)); For the pumping current through the ground state (P), it is approximated by $A_1 J_1^2(x)$ (the dashed curve in Fig. 5.17 (b)). This behavior is experimentally observed in section 5.1 and earlier by Oosterkamp [OKAEAKH97, OFvdW⁺98]. For

even higher microwave powers the PAT features considerably broaden due to heating effects until they are finally completely washed out. For the sidepeak (E) where the excited state participates in transport enabled by two-photon absorption in the ground state, the amplitude is fitted by a linear combination of the pure two-photon assisted tunneling through the ground state and the correlated two-photon-assisted tunneling with resonant tunneling through the excited state ($A_2 J_2^2(x) + A'_2 J_0^2(x) J_2^2(x)$). In the fitting shown in Fig. 5.17 (b), the parameters are $A_0 = 0.15$, $A_1/A_0 = 1.2$, $A_2/A_0 = 1.5$, and $A'_2/A_0 = 6.3$. Due to the limited bandwidth of our high frequency setup, no frequency dependence can be studied to identify the photon-induced peaks. Studying the power dependence only is not sufficient to reveal the origin of peak (E). However, the out-of-phase component of the complex photocurrent indicates some aspects of the origin (see below).

Having obtained the above basic transport properties of the dot by transport and straightforward microwave spectroscopy, heterodyne detection of photocurrent is applied. Two microwave synthesizers are phase-locked and tuned to slightly different frequencies $f_1 = 18.08$ GHz and $f_2 = 18.08$ GHz + δf with $\delta f = 2.1$ kHz. The two signals are added, frequency-doubled and filtered with a band pass as described before. We have thus produced a flux of photons with energy $hf \approx 2hf_1 = 0.15$ meV whose intensity varies periodically in time with frequency $\delta f = 2.1$ kHz. With two lock-in amplifiers the in-phase and out-of-phase photocurrent signals ($\gamma_0, \gamma_{\pi/2}$) with respect to the reference are measured. Then γ_0 and $\gamma_{\pi/2}$ follow the total photocurrent amplitude A and the relative phase Φ . In Fig. 5.18 the photocurrent amplitude is displayed for the same parameter region as the dc measurement shown in Fig. 5.14. With respect to Fig. 5.14, for $V_{ds} > 0$ the energetic window (between “gs” and “gd”) is enlarged by $2hf$. The resonances are each shifted by the photon energy hf which can readily be explained by PAT processes as in Fig. 5.16 (a) and (b). This is also the case for the drain-related resonances under negative bias. However, the source-related resonance under small negative bias is clearly shifted by Δ_- , thus enlarging the total energetic window (between “gd” and “gs”) to $eV_{ds} + hf + \Delta_-$. The process involved is taken as the finite bias version of the transition depicted in Fig. 5.16 (c): An electron leaves the quantum dot’s ground state for the source contact via absorption of two photons. Now, electrons can either refill the ground state or tunnel through the excited state as long as the ground state is empty. Transport through the excited state stops when an electron decays to the ground state, or an electron enters the quantum dot’s ground state from the leads. With $\Delta E < 0$ and larger negative bias, the photocurrent peak is apparently broadened. The broadening is partly due to other tunneling processes possible at large bias, e.g., one-photon PAT through the ground state. In fact, even at small negative bias there is small tunneling current in between the peak (M) and (E), which is most probably the one-photon PAT. In a different quantum dot as presented in Sec. 5.1, the one-photon sidepeak is much stronger than the excited-state involved sidepeak since

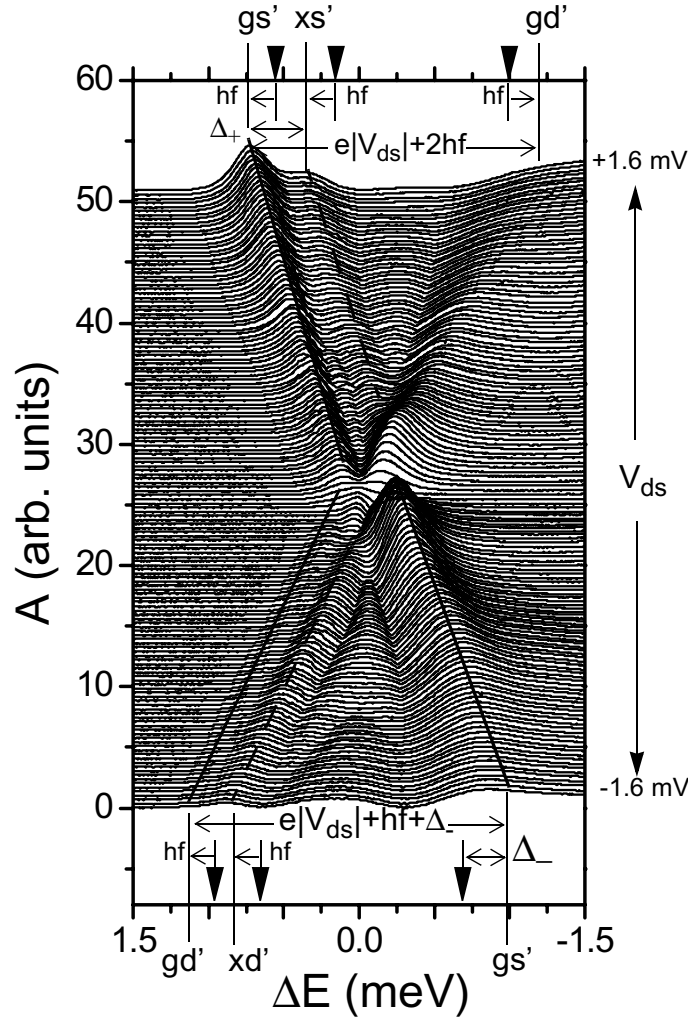


Figure 5.18: Amplitude A of the photocurrent obtained with the heterodyne setup (Frequencies are $f_1 = 18.08$ GHz, $f_2 = f_1 + \delta f$ with $\delta f = 2.1$ kHz. The corresponding microwave powers from the sources are -22.7 dBm and -24.8 dBm. The drain-source bias is varied as in Fig. 5.14. The positions of the resonances found in the quasi-static measurement of Fig. 5.14 are indicated with triangles. With respect to the quasi-static resonances, most photocurrent resonances are shifted by the photon energy hf , as can be expected for photon-assisted processes. The resonance for $V_{ds} < 0$ and $\Delta E < 0$, however, is shifted by Δ_- (see text for details).

the coupling of the excited state to contacts is weaker than the ground state.

In Fig. 5.19 (a) and (b), phase traces as well as their respective amplitude signals are displayed for small positive ($V_{ds} = +10$ μ V) and negative ($V_{ds} = -30$ μ V) bias, re-

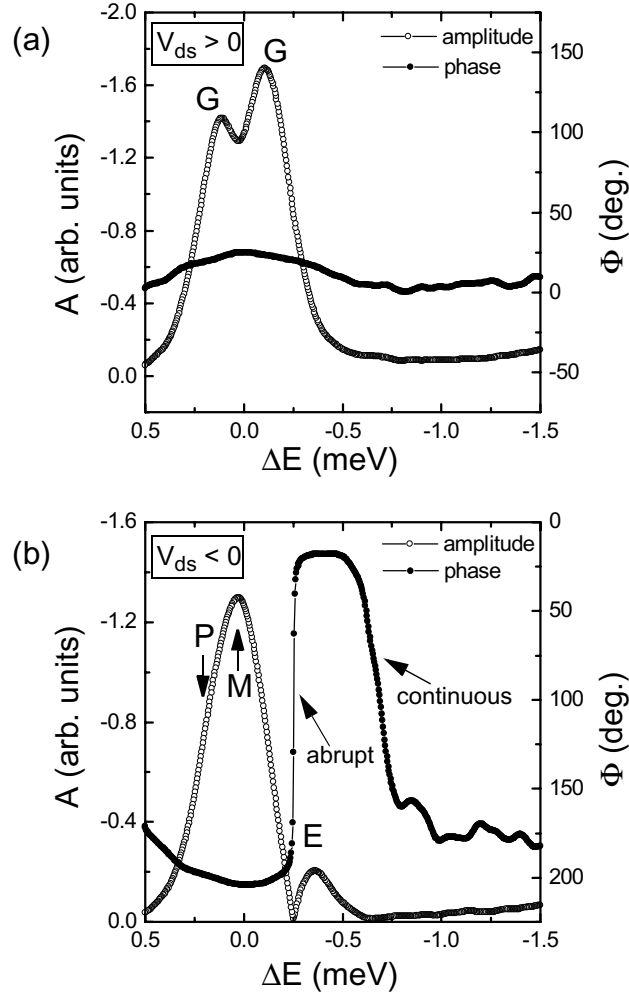


Figure 5.19: The phase and amplitude of the photocurrent signal for (a) $V_{ds} = +10 \mu\text{V}$ and (b) $V_{ds} = -30 \mu\text{V}$. For positive bias, PAT through the ground state (G) is observed, as schematically depicted in Fig. 5.16 (a) and (b). The phase signal remains constant on either side of the resonances. For negative bias, tunneling through an excited state (E) and pumping (P) through the ground state are induced (cf. Fig. 5.16 (c) and (d)). Vanishing of the amplitude signal between (P) and (E) is accompanied by a trivial jump of π in the phase signal. Finally, for more negative values of ΔE the phase signal continuously falls back to its original value.

spectively. For $V_{ds} > 0$ the phase signal remains approximately constant at $\Phi = 0$ which means that the out-of-phase photocurrent $\gamma_{\pi/2}$ is equal to zero. The response of the quantum dot to the microwaves is similar for both of the tunneling processes (G). In fact, the two peaks (G) in the amplitude signal stem from ground state resonances as depicted in Fig. 5.16 (a) and (b). The situation is considerably different for

$V_{ds} < 0$ where a strong pumping signal (P) is observed which is caused by a process as in Fig. 5.16 (d). At the position where the photocurrent changes its direction, the amplitude drops to zero and the phase changes trivially by π (this corresponds to crossing zero in the $\gamma_0 - \gamma_{\pi/2}$ plane). The second peak (E) stems from the photon-induced tunneling through the excited state as in Fig. 5.16 (c). Moving away from this second resonance to more negative ΔE , the phase continuously returns to its original value.

This continuous phase change shows that this transport process results in a finite out-of-phase signal $\gamma_{\pi/2}$. In contrast to the other transport scenarios described above (only the ground state is involved), photon-induced tunneling through the excited state is not a purely conductive transport process but also has capacitive and inductive contributions. This behavior is due to the complicated charging dynamics of the quantum dot for this particular process. The processes involved are PAT from the ground state to the source reservoir, resonant tunneling through the excited state, recharging of the ground state by the drain reservoir and relaxation from the excited state to the ground state. All these processes have different time constants which additionally depend on the gate voltage (i.e., ΔE). The interplay of these processes results in the observed phase lag. Thus one has a method at hand to determine the admittance of a mesoscopic system [FD93, BPT93a, BPT93b] in the PAT regime which is related to the average relaxation time of the system. In the current setup, for $V_{ds} < 0$ the ground state broadening, due to the coupling to the drain contact, is about 400 MHz, while the level broadening from the coupling to the source contact is around 2 GHz. The broadening of the excited state coupling to the contacts is found to be of the same width of 2 GHz. Hence, the bare tunneling time through the ground state, excluding other time constants, would be less than 2.5 ns. This time scale is comparable to the phase coherence time in such an almost-isolated quantum dot [BSH⁺98]. However, the inverse modulation frequency $1/\delta f \approx 500 \mu s$, which is the time separation between two microwave flux minima, is much larger than the tunneling time. This indicates that it takes the electron a much longer time to relax within the dot than to tunnel through the dot directly.⁷ An extension of the measurements to modulation frequencies on the order of 10 – 100 MHz corresponding to a time scale of 10 – 100 ns would therefore be desirable. With a shorter microwave beat period it allows to probe the fast tunneling event. However, since the limitation in the bandwidth of current preamplifier and of the cables for measuring the tunnel current, no signal can be detected with higher modulation frequency. In the future experiments, coaxial cables and high frequency preamplifier will be used to reveal the exact relaxation time. In summary for this section, with the frequency f the photon energy hf for the photon-induced process can be adjusted, whereas the modulation frequency δf determines the time scale on which

⁷Similar long relaxation time (longer than a few μs) between the excited state and the ground state is also observed recently by Fujisawa *et al* using a different technique [FTH01], which is attributed to the slow spin-flip occurred during the relaxation from the excited state to the ground state.

the electronic dynamics of the quantum dot is probed. In a single quantum dot, the excited state possesses a long life time which is much longer than the phase coherence time. No superposition of the ground state and the excited state can be achieved if the relaxation process is slow.

5.4 Broadband Microwave Spectroscopy of A Single Quantum Dot

As discussed in the previous section, two continuous microwave sources with a slight frequency offset form a heterodyne detection of the induced complex photocurrent. In this section, two coherent picosecond-pulsed – hence broadband – millimeter waves are combined and irradiate a single small quantum dot. The detailed description on the whole setup for this broadband microwave spectroscopy is presented on page 122 in App. B.

The generation of the pulsed microwave radiation is schematically shown in Fig. 5.20, where the spectrometer itself consists of two nonlinear transmission lines (NLTLs) [vdWK, vdW92, vdW94, vdWBAB93]. The meander-shaped NLTL coplanar waveguide (Fig. B.4 (a) on page 120) is intersected by contacts forming Schottky diodes that act as voltage-variable capacitors in reverse bias, leading to the circuit's pulse-forming response [vdWBAB93]. The two NLTLs are driven by two stable and phased-locked microwave sources (HP83711A), whose output is amplified to ≈ 0.5 W. The frequencies are tuned at $f_1 = 7.8$ GHz and $f_2 = f_1 + \delta f$ ($\delta f = 21$ Hz), respectively. Driven by a sinusoidal microwave source at frequency of $f = 7.8$ GHz, the output of an NLTL contains harmonic frequency contents from 20 GHz to 400 GHz, which is a train of short pulses with the pulse repetition rate of $f = 7.8$ GHz, see Fig. 5.20 (b). Then, the outputs from the NLTLs are combined and sent to a bowtie antenna (see Fig. B.4 (b)). The combiner and antenna circuit are defined by evaporating gold onto a high-resistivity silicon substrate (see Fig. B.4 (b) and (c)). In contrast to an earlier version of the spectrometer [BvdWHE98] both NLTLs, the combiner and the bowtie antenna are integrated in a single brass box at room temperature (see Fig. B.4 (c) and (d)), which is mounted *in-situ* on the entry of a cylindrical waveguide (the lower cutoff is ~ 80 GHz) of the sample holder. Infrared radiation is blocked by a black polyethylene window. Finally, the superimposed pulse trains of the NLTLs are radiated into the cylindrical waveguide through a silicon hemisphere attached to the antenna on the back side of the combiner and antenna circuit (Fig. B.4 (d)) [vdW94]. The quantum dot sample is mounted on the sample holder in a way so that the surface of the sample is in face of the opening of the waveguide and the distance between them is less than 2 mm. This allows us to probe the complex photocurrent in the 80 – 400 GHz range,

5. Microwave Spectroscopy of Semiconductor Quantum Dots: Experiment

corresponding to energies of $320 \mu\text{eV} - 1.6 \text{ meV}$. The typical charging energies of small dots are of the order of $500 \mu\text{eV} - 1.5 \text{ meV}$, while the energies of the excited states in these dots are around $100 \mu\text{eV} - 0.5 \text{ meV}$.

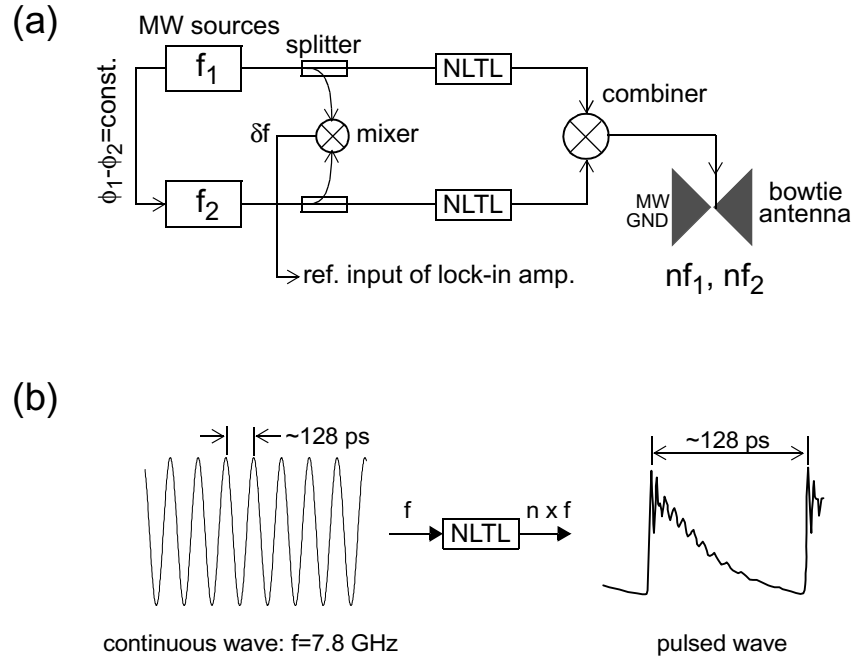


Figure 5.20: (a) A schematic setup for generating a pulsed microwave radiation by two NLTLs. (b) A continuous sinusoidal microwave signal at the input of an NLTL. The output is a train of pulses which has a repetition rate of the input frequency.

Since the output of this spectrometer is coherent with a known time base, it allows for the heterodyne detection of both the amplitude (A) and the phase (Φ) of induced photocurrent in a wide frequency range, from which electron dynamics can be deduced. In the experiments, the γ_0 - and $\gamma_{\pi/2}$ -components of the photocurrent ($\tilde{I} = Ae^{i\Phi} = \gamma_0 + i\gamma_{\pi/2}$) are monitored by lock-in amplifiers. Another advantage of applying this spectrometer is that during the broadband spectroscopy the quantum dot system is always in a constant thermal environment induced by microwaves, in contrast to conventional tuned sources, such as Gunn diodes, whose power variation with frequency complicates broadband spectroscopy.

The quantum dot used in this particular experiment is realized from the sample QD-sample#1 described on page 115 in App. A. The 2DEG is 90 nm below the surface and has an electron density of $n_s = 1.7 \times 10^{11} \text{ cm}^{-2}$ and a mobility of $8 \times 10^5 \text{ cm}^2/\text{Vs}$.

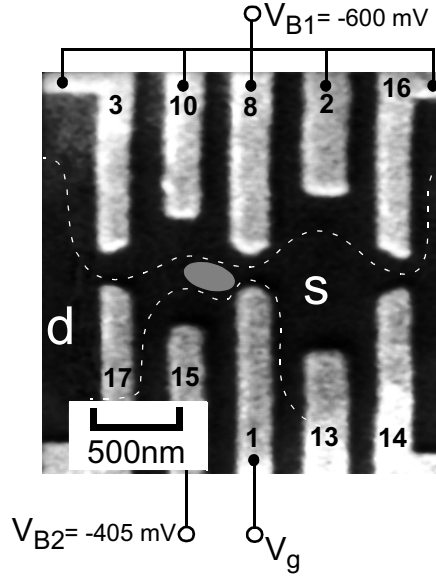


Figure 5.21: The formation of a single dot from the sample QD-sample#1 (see Sec. A). $T = 150$ mK.

In comparison to Sec. 3.2 and Sec. 5.2, different gate configurations and gate voltages are applied to form a single dot, as shown in Fig. 5.21. A quantum dot with a radius (r) around 100 nm is formed containing about 20 – 50 electrons. The operating temperature of the $^3\text{He}/^4\text{He}$ mixture in the dilution refrigerator is $T_b = 35$ mK, while the electron temperature in these measurements remains at about $T = 150$ mK under irradiation with the spectrometer.

Both the direct tunnel current (I_{ds}) (Fig. 5.22) and the differential conductance ($g = dI_{ds}/dV_{ds}$) of the quantum dot are measured; the dashed lines obtained from the conductance measurement reveal CB diamonds. There is finite tunneling current within the CB diamonds, evidence of strong cotunneling [AN90, OBS92, FSE⁺01] in the CB regime, indicating that the quantum dot is strongly coupled to the contacts. This is reinforced by the observation that in the SET regime there is strong inelastic tunneling, such that hardly any fine structure indicating electron transmission through excited states is found in the SET regime. Furthermore, the right tunnel barrier connecting the dot the source contact is thinner than the left barrier, as schematically shown in the level diagrams of Fig. 5.23 and Fig. 5.24. Consequently the upper-right and the lower-left Coulomb diamond boundaries (along which the dot energy is aligned with the Fermi level in the drain) are sharper and higher than the upper-left and the lower-right source-related boundaries. The varying size of the diamonds indicates that the dot's total capacitance ($C_\Sigma = C_L + C_R + C_g$) changes upon adding or removing a single

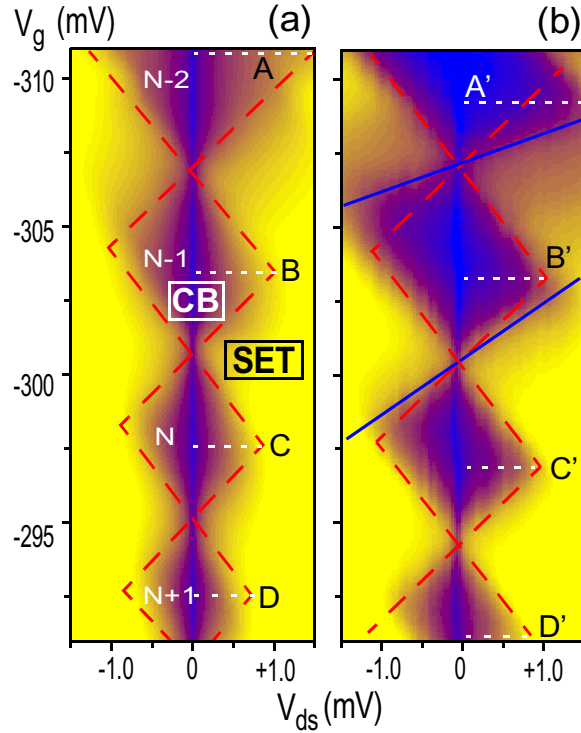


Figure 5.22: (a) Logarithmic plot of the absolute direct tunnel current ($|I_{ds}|$) in the V_{ds} - V_g plane, (yellow: $I_{ds} \geq 3$ nA, blue: $I_{ds} \leq 1$ pA). The red dashed lines for the enclosed diamonds are obtained from the conductance (not shown), where the diamond boundaries are easier to determine. The number of electrons in the dot is indicated by $N + 1$, N , $N - 1$, etc. (b) Logarithmic plot of the absolute direct tunnel current measured under millimeter-wave radiation from the NLTLs (yellow: $I_{ds} \geq 0.7$ nA, blue: $I_{ds} \leq 0.1$ pA). The dashed diamonds have the same slopes for respective boundaries. The blue solid lines indicate the boundaries that have smaller slopes. In both plots, the horizontal white dashed lines labeled with A(A'), B(B'), C(C') and D(D') mark the positions at which I_{ds} - V_{ds} curves shown in Fig. 5.23 are extracted. $T = 150$ mK.

electron. The slopes of the diamond are $s_1 = \delta V_g / \delta V_{ds} = (C_R + C_g) / C_g = 3.66$ and $s_2 = \delta V_g / \delta V_{ds} = -C_L / C_g = -3.93$, yielding a ratio $\alpha = C_g / C_\Sigma = 1.3 \times 10^{-1}$, where α converts the gate voltage (V_g) to an energy distance $\Delta E = -e\alpha\Delta V_g$; the capacitance of the dot to the left (C_L) and the right (C_R) contact and to the gate ($C_g \approx 25$ aF) are denoted respectively. An average charging energy of $E_C = e^2 / C_\Sigma \approx 0.8$ meV for the two Coulomb diamonds in the center of Fig. 2(a) is estimated. Although no transport through excited states is resolved in the SET regime (Fig. 5.22 (a)), we determine the average energy scale ($\Delta\epsilon^*$) of the dot's excited states using transport measurements under millimeter-wave radiation (see below).

Fig. 5.22 (b) shows the absolute current through the quantum dot under this broadband

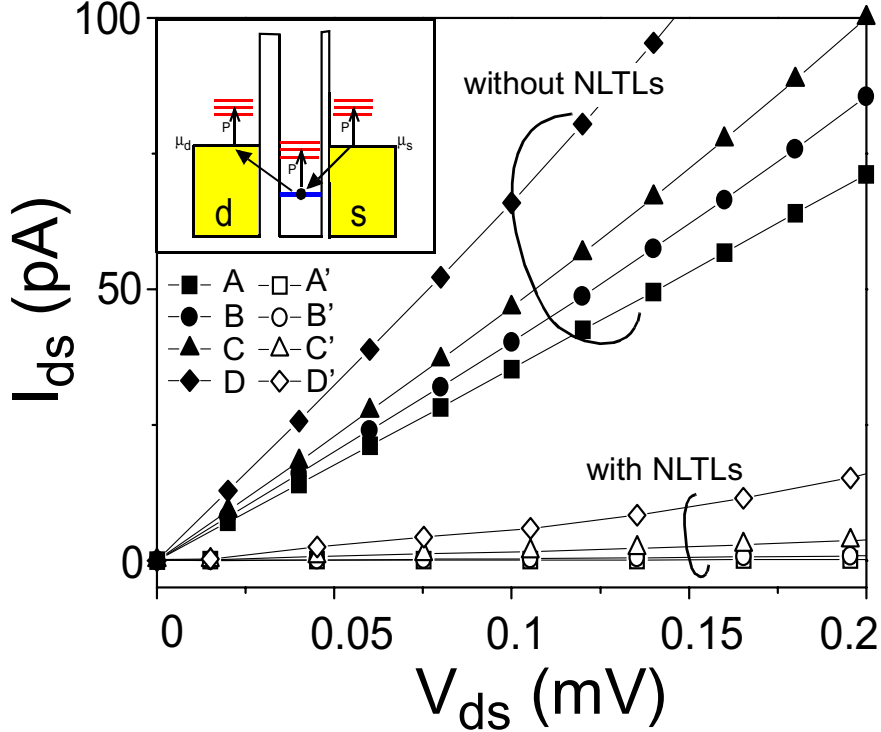


Figure 5.23: The $I_{ds} - V_{ds}$ curves in CB regimes at positions labeled with A(A'), B(B'), C(C') and D(D') as shown in Fig. 5.22. The range of V_{ds} is from $0 \mu\text{V}$ to $200 \mu\text{V}$, in which $e|V_{ds}| < \Delta\epsilon^*$, i.e., elastic cotunneling dominates. Inset: The level diagram for $V_{ds} \approx 0 \mu\text{V}$. The electrons in the contacts are promoted to virtual states by microwave photons; elastic cotunneling of electrons is strongly suppressed. $T = 150 \text{ mK}$.

millimeter wave radiation having harmonics $f = n \times 7.8 \text{ GHz}$, with integer n such that $10 \leq n \leq 50$. Compared to the current without radiation (Fig. 5.22 (a)), finite cotunneling current is strongly suppressed within the CB diamonds. To quantitatively determine the suppression, $I_{ds} - V_{ds}$ curves within the CB diamond are extracted from Fig. 5.22 and shown in Fig. 5.23. Every curve is selected at specific gate voltage (V_g) so that the curve has a maximum threshold of V_{ds} . In Fig. 5.23, the symbols labeled with A (A'), B (B'), C (C') and D (D') correspond to the same labels of the horizontal dashed lines in Fig. 5.22. Both with and without radiation the finite tunneling current is proportional to the small bias V_{ds} within the CB regime, indicating elastic cotunneling in which only one quantum state participates (inset Fig. 5.23). The net elastic cotunneling current I_{ds}^{el-co} is approximately (refer to Eq. [2.29]) $I_{ds}^{el-co} \approx \frac{\hbar G_L G_R \Delta\epsilon^*}{\pi e^2 E_C} V_{ds}$, where G_L and G_R are the independent conductance of the left and right tunnel barriers, respectively [AN90]. Elastic cotunneling dominates when $e|V_{ds}| < \Delta\epsilon^* \sim 0.2 \text{ meV}$

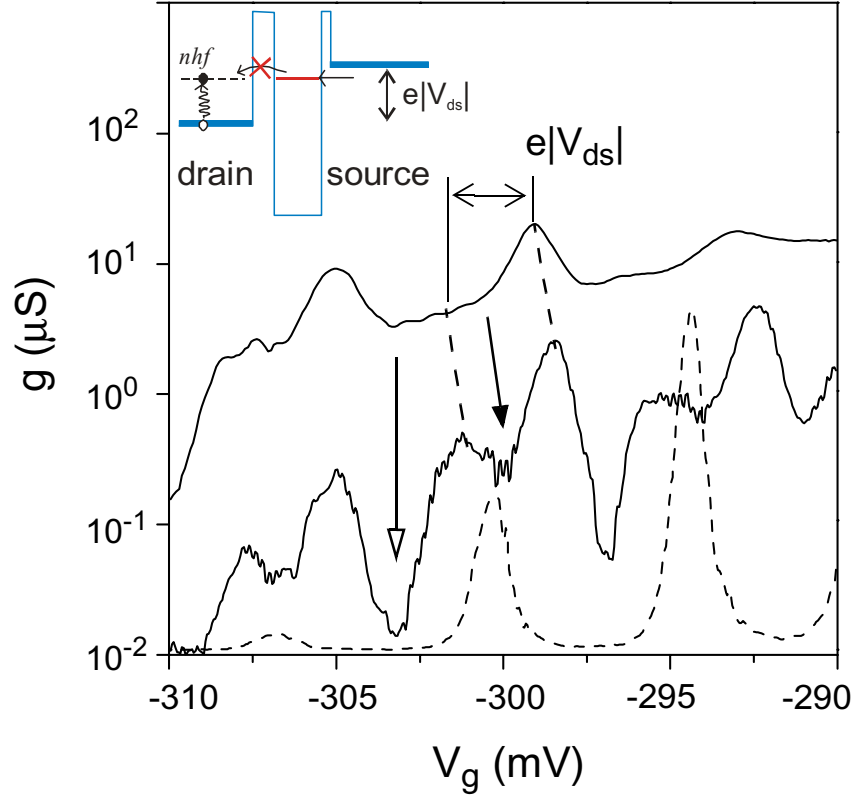


Figure 5.24: The dashed linear plot is the conductance measured at $V_{ds} \approx 0 \mu\text{V}$ under radiation. The peaks represent ground state resonances. The upper and lower solid logarithmic plots correspond to the conductance measured at $V_{ds} = +0.75 \text{ mV}$ without and with millimeter-wave radiation, respectively. At finite bias, the ground-state resonance splits by $e|V_{ds}|$. Inelastic tunneling of electrons contributes to the measured finite current between the splittings. With millimeter-wave radiation, inelastic tunneling is suppressed as indicated by a downward solid arrow. In CB regimes, i.e., the valley of two adjacent ground state resonances, the reduction of tunneling current (indicated by a downward open arrow) is due to the suppression of cotunneling of electrons. Inset: The level diagram of inelastic tunneling at finite bias. The inelastic tunneling process is blocked when virtual states are occupied by electrons in the leads absorbing photons. $T = 150 \text{ mK}$.

and $T < \sqrt{E_c \Delta \epsilon^*} / k_B \sim 4.6 \text{ K}$ [AN90, OBS92, FSE⁺01]; given the $\Delta \epsilon^*$ found below, these conditions are fulfilled in this experiment, and the radiation suppresses the cotunneling current by about one order of magnitude, as shown in Fig. 5.23. This suppression is due to the *in-phase* modulation of the tunneling rates for both the left and right tunnel barriers [Eto01], as schematically shown in the inset of Fig. 5.23.

In Fig. 5.24 we compare the conductance (g) with and without radiation at $V_{ds} = +0.75$ mV; the finite bias splits the ground state resonance. With radiation, the valley between these resonances is deeper than without it, a suppression of inelastic tunneling. It follows that excited electrons in the drain contact occupy virtual states through which electrons tunnel from the dot to the drain contact (see the inset of Fig. 5.24). Inelastic tunneling depends strongly on the density of states $D(E)$ above the Fermi level in the leads, which is reduced under radiation.

Since more than 40 harmonics of the fundamental microwave frequency are radiated simultaneously to the quantum dot, some thermal broadening and extensive overlap of PAT sidebands occur. Individual sidepeaks are not resolvable in Fig. 5.22 (b) as single-frequency PAT on quantum dots [BHvdW⁺95, OKAEAKH97, OFvdW⁺98, QBK⁺01]. However, the dot's response to a given millimeter-wave harmonic can be selected and filtered using a phase sensitive detection method in this thesis, given linear response, which is verified by checking the dot's proportional response to slight changes in spectrometer power [BvdWHE98].

The dual-source spectrometer emits picosecond pulses that overlap at an offset frequency $f_b = n \times \delta f = n \times |f_2 - f_1| = n \times 21$ Hz (Fig. 5.20), since it is driven by two phase-locked synthesizers. This allows filtering of the corresponding harmonics with a digital lock-in amplifier whose reference is δf . The millimeter-wave radiation at $n \times f$ introduces a small voltage modulation $\delta V_{ds}(f_b) \exp(-i2\pi f_b t)$ and $\delta V_g(f_b) \exp(-i2\pi f_b t)$ in the drain-source bias V_{ds} and in the gate voltage V_g , respectively. Taking into account all of the harmonics, the corresponding voltage modulation is $\tilde{V}_{ds} = \sum \delta V_{ds}(f_b) \exp(-i2\pi f_b t)$ and $\tilde{V}_g = \sum \delta V_g(f_b) \exp(-i2\pi f_b t)$. At small V_{ds} , the photocurrent signal $\tilde{I} = A e^{i\Phi} = \gamma_0 + i\gamma_{\pi/2}$ yields $A \propto (g + V_{ds} \frac{\partial g}{\partial V_{ds}}) \tilde{V}_{ds} + V_{ds} \frac{\partial g}{\partial V_g} \tilde{V}_g$. A two-channel lock-in amplifier is used to monitor the γ_0 - and $\gamma_{\pi/2}$ -components of the photocurrent resulting from the corresponding millimeter-wave harmonics ($n \times f$).

Thus in contrast to the total induced current under radiation (Fig. 5.22 (b)), two photocurrent spectra (of the $\gamma_{\pi/2}$ component)⁸ taken at the 12th harmonic of the offset frequency (corresponding to $f_\alpha = 93.6$ GHz (a)) and the 18th harmonic (corresponding to $f_\beta = 140.4$ GHz (b)) are given in Fig. 5.25. The diamond shaped Coulomb blockade regions resemble those observed in Fig. 5.22 (b). Furthermore, additional features are observed in the SET regime. Single traces are extracted from Fig. 5.25 (a) and (b) and shown in Fig. 5.25 (c) and (d), respectively. The blue solid lines indicate the ground-state resonances corresponding to the CB diamond boundaries in Fig. 5.25 (a) and (b). The dashed lines reveal fine structure from excited-state resonances in the SET region. An average excited states energy is found $\Delta\epsilon^* \approx \frac{\hbar^2}{m^* r^2} \sim 200 \mu\text{eV}$, which

⁸The $\gamma_{\pi/2}$ component reveals features similar to that of the γ_0 component and that of the amplitude $A = \sqrt{\gamma_0^2 + \gamma_{\pi/2}^2}$, but in this case has better resolution.

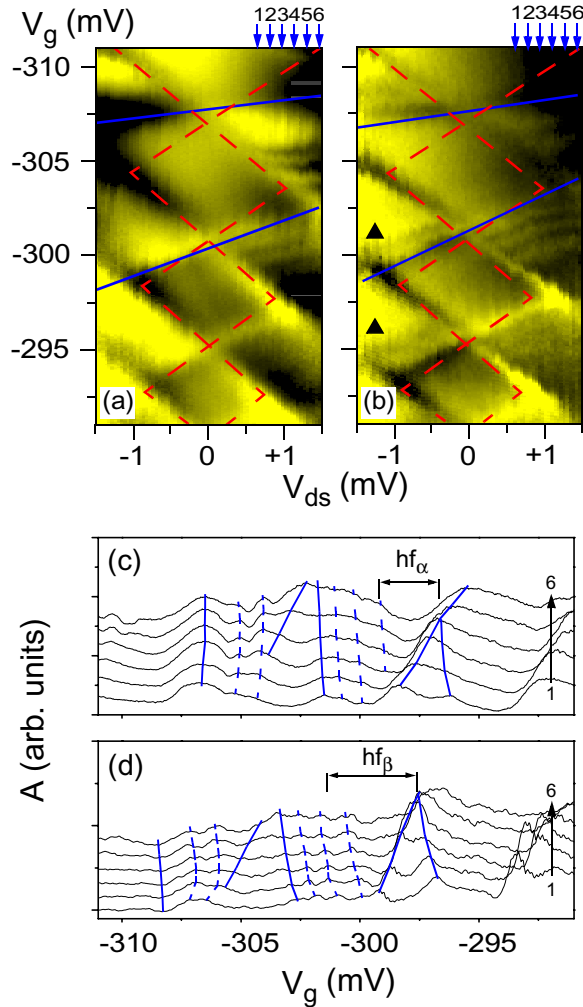


Figure 5.25: (a) Linear plot of the $\gamma_{\pi/2}$ component of the photocurrent at the 12th harmonic, $f_\alpha = 93.6$ GHz. The drain-source bias is varied from -1.5 mV to $+1.5$ mV. (b) Linear plot of the $\gamma_{\pi/2}$ component of the photocurrent at the 18th harmonic, an excitation frequency of $f_\beta = 140.4$ GHz. In (a) and (b), the $\gamma_{\pi/2}$ component is in arbitrary units: yellow represents negative values and black is positive. The red dashed lines indicate the diamonds as shown in Fig. 5.22 (a). The blue solid lines show the diamond boundaries with reduced slopes. In the SET region, fine structures corresponding to excited state resonances are clearly visible. The excited state resonances in the SET regime with negative bias are marked with solid triangles. Traces extracted from (a) and (b) at six specific gate voltages are shown in (c) and (d), respectively. In (c) and (d), the blue solid lines trace the ground state resonances, while the dashed lines represent the excited state resonances as shown in (a) and (b). $T = 150$ mK.

follows an estimated “electronic” dot radius (r) about 80 nm. This dot’s radius coincides with the estimation (≈ 100 nm) based on the dot’s geometry. Although PAT

sidepeaks are weakly evident in Fig. 5.25, strong frequency dependent features are observed (marked by two solid triangles), such as two excited-state resonances at the 18th harmonic f_β (Fig. 5.25 (a)), while these resonances are not found at the 12th harmonic f_α in the SET regime with negative bias (Fig. 5.25 (b)). In Fig. 5.26, the amplitude A of photocurrent at the 18th harmonic f_β and the quasi-static conductance under radiation are compared. The dashed curve in Fig. 5.26 (b) is a simulation based on the above discussion taking $\delta V_{ds}(18 \times \delta f) \sim 10 \mu\text{V}$ and $\delta V_g(18 \times \delta f) \sim 0.8 \text{ mV}$. The low frequency modulation of V_g changes the dot potential by less than 50% of $\Delta\epsilon^*$, and no strong broadening of the ground state resonance due to heating by radiation is observed.

Millimeter-wave radiation changes the slopes of the diamond boundaries in Figs. 5.22 (b), 5.25 (a) and 5.25 (b) compared to those in Fig. 5.22 (a). We find s_1 is decreased to 3.30, and s_2 to about -0.45 (corresponding to the upper-most diamond in Fig. 5.25 (a)). Correspondingly, the tunnel barrier capacitances C_L and C_R are reduced by 89 % and 18 %, respectively. The reduction of C_g is only 3%. Similar values are evident at 140.4 GHz (Fig. 5.25 (b)). Although the slopes under higher gate voltages are closer to the ones in the static limit, the capacitance of the left contact C_L maintains a clearly different response under radiation.

This reduction in slopes arises from two effects: First, the capacitance C of a nanometer sized tunnel barrier is the geometrical capacitance C_0 in series with a “quantum capacitance” C_q , i.e.,

$$C = \frac{C_0 C_q}{C_0 + C_q}. \quad (5.10)$$

The “quantum capacitance” C_q exists between the total density of states $D(E)$ in the dot and one of the contacts at the Fermi level E_F , $C_q = e^2 D(E_F)$ [Bue00]. As noted above, the tunneling rate is reduced since radiation reduces the local effective density of states $D(E_F)$, reducing the capacitance of the tunnel barrier. Second, since electrons not only tunnel but are also pumped from the contacts into the dot, the competition between the pumping rate and the relaxation rate of electrons also affects the slopes. During the window of pulse overlap in the spectrometer, which occurs every $1/f_b$ seconds, a burst of picosecond pulses with repetition time $t_{rep} \approx 128 \text{ ps}$ ($= 1/7.8 \text{ GHz}$) is emitted. The radiation at f_α and f_β excite electrons into energetically higher states at an effective pumping rate of the spectrometer’s fundamental of 7.8 GHz. The relaxation time of electrons tunneling from the dot to the contacts increases since relaxation processes (e.g., inelastic tunneling) are suppressed by millimeter-wave radiation. We approximate this long relaxation time with an effective time constant $\tau \sim RC$: Assuming $C = C_\Sigma \approx 90 \text{ aF}$ ⁹ and a dc resistance $R \approx 2.5 \text{ M}\Omega$ of the tunnel barriers at

⁹The total capacitance C_Σ is reduced from about 191 aF to 90 aF under millimeter-wave radiation.

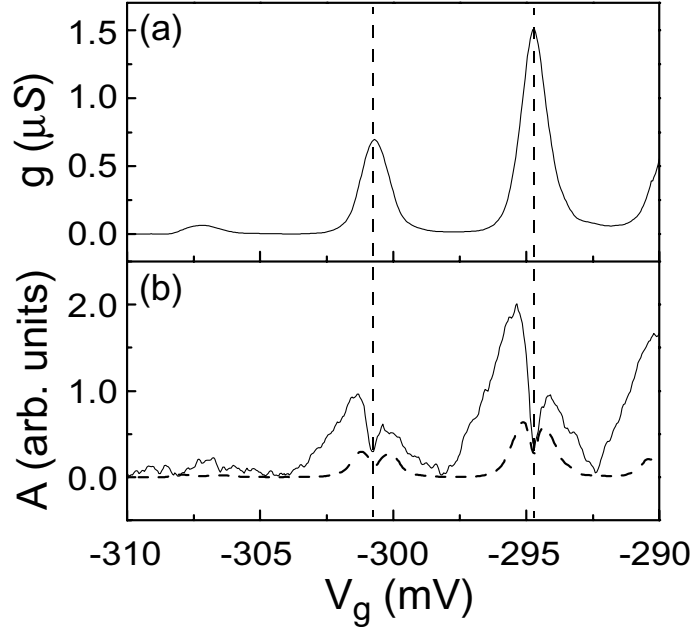


Figure 5.26: (a) The CB oscillations as seen in conductance (g) under radiation from NLTs. (b) The amplitude (A) of the photocurrent measured at $f_b = 18 \times \delta f$ (corresponding to $f_b = 140.4$ GHz). Both are at a bias value of $V_{ds} = -25 \mu\text{V}$. The dashed curve in (b) is a simulation based on the measured data from (a) and with parameters $\delta V_{ds}(f_b) \sim 10 \mu\text{V}$ and $\delta V_g(f_b) \sim 0.8$ mV.

resonance, $1/\tau \sim 4.4$ GHz, which is lower than the pumping frequency. The Coulomb blockade prevents additional electrons from tunneling into the dot before the previous electron relaxes into the contacts. The measured capacitance of the barriers is thus lower than the static value without radiation. For CB diamonds at higher gate voltages than the first one, the tunnel coupling between the dot and the contacts increases, the electrons in the dot are less tightly confined, and radiation does not affect the dot-to-lead capacitance as much, resulting in closer correspondence to the static measurements. Furthermore, since the right tunnel barrier is more transparent than the left one, it experiences a smaller reduction in capacitance by millimeter-wave radiation. By contrast, the study on a similar single quantum dot discussed in the previous section [QBK⁺01] shows that the slopes of the diamond boundaries are not affected when the applied millimeter-wave radiation is continuous rather than pulsed.

In summary for this broadband microwave spectroscopy, charge relaxation plays an important role in transport through a single quantum dot. Pulsed microwave radiation allows for probing the slow relaxation process. At the same time, microwave pulse it-

self modifies the relaxation processes by changing the density-of-states of the quantum dot.

In this quantum dot, the phase coherence time might be larger than the charge relaxation time (~ 0.2 ns). However, the lifetime of the quantum state becomes shorter as the relaxation time decreases by increasing the dot-contact coupling. Superpositions of the ground state and the excited state can hardly be realized in a single quantum dot due to the above contradictory of the lifetime and the relaxation time. This is in agreement with the result obtained in Sec. 5.3. In comparison, coherent superpositions of molecular states can be realized by microwave photons in a double quantum dot which is almost isolated from the contacts to minimize the dephasing.

With even more intensive frequency components applied to the quantum dot, the broadband microwave radiation is a good analogy to the continuum spectrum of the electromagnetic environment. The impact of the whole frequency band can be sampled by detecting the photocurrent resulted from a certain number of single frequencies. The dissipation of electron transport can be studied. Given two microwave sources with large frequency offset applied to the quantum dot, the photocurrent at different microwave frequencies could be linearly superimposed. On the other hand competitions might be induced between two sources. Also, nonlinear effects, such as mixing will occur.

5. Microwave Spectroscopy of Semiconductor Quantum Dots: Experiment

Chapter 6

Conclusion and Outlook

In this thesis, electron transport through confined electronic states in quantum dots at low temperatures is studied using both *transport spectroscopy* and *microwave spectroscopy*. By transport spectroscopy, the basic electronic structure of quantum dots is obtained. Microwave spectroscopy reveals the dynamic properties of transport through confined quantum states.

The samples being studied are cooled in a $^3\text{He}/^4\text{He}$ dilution refrigerator. The quantum dots are formed by electrostatic confinement potentials: By applying proper negative gate voltages to the Schottky gates patterned on the surface of an AlGaAs/GaAs heterostructure, a puddle of electrons is separated from the whole high-mobility two-dimensional-electron-gas (2DEG) of the heterostructure. Plunger gates are capacitively coupled to quantum dots for tuning the dot's potential. For transport studies, quantum dot circuits are connected to drain and source contacts via tunnel barriers formed by *quantum point contacts* (QPCs), which can be continuously tuned to be pinched-off. The diameter of such planar quantum dots studied in this thesis is in the range from 140 nm to 600 nm, corresponding to about 20 to 200 electrons on one dot.

A large single quantum dot containing about 200 electrons is well confined. Under zero drain-source bias, more than 200 Coulomb-blockade oscillations are observed in the dot's conductance: Each conductance peak corresponds to single-electron tunneling through a ground state with a certain number of electrons on the dot (Fig. 3.4). Excited states are revealed by measuring the dot's conductance in the $V_{ds} - V_g$ plane, forming the Coulomb-blockade diamonds (Fig. 3.5). Furthermore, the lifetime of quantum states can be controlled by tuning the tunnel barriers which couple the quantum dot to the external electron reservoirs (Fig. 3.9). This kind of semiconductor quantum dots are proved to be well controlled *artificial atoms*.

A double-dot *artificial molecule* is formed by coupling two single quantum dots with a tunnel barrier. The double dot is weakly connected to the drain and source leads and

is operated under near-zero drain-source bias to minimize the dephasing by contacts. This double-dot molecule is tuned to be “ionic” and “covalent” depending on the tunnel coupling set by a central gate voltage. When the inter-dot tunneling is small, an “ionic” double-dot molecule is formed, where electrons are localized on each dot. The *charging diagrams* reveal the electrostatic properties of the double dot, e.g., the inter-dot Coulomb interaction (Fig. 3.11). In an ionic double-dot molecule, a single electron tunnels through the molecule only when two quantum states are aligned to each other and are aligned to the Fermi levels in the contacts. When the inter-dot tunnel coupling is strong, the finite tunneling strength couples the two quantum states and forms the bonding and anti-bonding molecular states (Eq. [2.58]). When the detuning between the two quantum states is zero, an electron on the bonding state is completely delocalized and tunnels back and forth between two dots at a Rabi frequency of $\Omega_0 = 2t/h$, where t is the inter-dot tunneling strength. With a nonzero detuning, an electron is localized in one of the dots whose quantum state has a lower energy. The formation of bonding and anti-bonding molecular states is observed directly in the charging diagrams (Fig. 3.12). As a two-level system, this double quantum dot is sensitive to the excitation from the environment. Finite off-resonance tunneling through the double dot, which is induced by acoustic phonon-assisted tunneling (Fig. 3.13), is observed. The phonons stem from a confined phonon mode of a phonon cavity which is formed by Schottky gates on the surface of the piezoelectrical GaAs crystal and is driven by either thermal energy or microwave radiation. It is found that the phonon mode effectively interacting with electrons in the double-dot molecule has a frequency of 10 GHz. This phonon mode is slightly influenced by the temperature.

Under microwave radiation, photon-assisted tunneling (PAT) is observed in both single quantum dots and double quantum dots. In a small quantum dot with only about 20 electrons, photon-induced nonadiabatic pumping of electrons is observed (Fig. 5.15). Photon-induced tunneling through an excited state is observed when the ground state is depopulated by two photons, a process analogous to *photo-ionization* (Fig. 5.2 and Fig. 5.15). Since the two photon energy is only slightly larger than the excitation energy of the excited state, the ground state and the excited state are coupled by two microwave photons. The dynamics of this process is studied by applying a heterodyne detection technique. A long relaxation time around 500 μs is observed when the excited states is coupled to the ground state by microwave photons (Fig. 5.19). A much smaller relaxation time is measured without the excited state participating in transport.

In another small single quantum dot containing about 20 to 50 electrons, strong elastic cotunneling is observed in the Coulomb-blockade regime. By applying pulsed microwave radiation to this quantum dot (the pulse repetition rate is 7.8 GHz), the dynamics of electron transport is revealed. Due to electrons involved in elastic cotunneling processes can stay in the quantum dot for an additional time interval about the pulse period, elastic cotunneling is strongly suppressed (Fig. 5.23). which is due to

electrons involved in elastic cotunneling processes stay in the quantum dot for a longer time (Fig. 5.23). Under pulsed irradiation the dot's total capacitance is found to be reduced by about 53 %, which is a result of a reduction of the *quantum capacitance* of the quantum dot. This also implies that the electron relaxation in the dot is slower than the pumping by the pulsed microwave radiation. Furthermore, a strong suppression of inelastic tunneling in the nonlinear transport regime with finite drain-source bias is observed (Fig. 5.24). Inelastic tunneling channels are blocked by broadband microwave excitation of electrons in the contacts. Again, slow charge relaxation processes in a single quantum dot are found.

Under microwave radiation, the bonding and anti-bonding molecular states of a double-dot molecule are coupled by n -microwave photons, inducing photon-assisted tunneling which is clearly resolved in the charging diagrams (Fig. 5.6, Fig. 5.7). A single electron tunnels between the two dots at a Rabi frequency of $\Omega_R = 2tJ_n(e\tilde{V}/hf)$. Applying microwave radiation above 10 GHz, coherent superpositions of molecular states by one and two photons are confirmed by tuning the inter-dot tunnel coupling (Fig. 5.10). Below 8 GHz, superpositions of molecular states by both microwave photons and acoustic phonons are observed (Fig. 5.10). The microwave field coupled to the piezoelectrical GaAs crystal by Schottky gates effectively generates non-equilibrium acoustic phonons in the phonon cavity. The phonon frequency is mainly determined by the cavity size but not the frequency of the driving microwave field: A phonon mode at 10 GHz, which is in agreement with the phonons observed in the absence of microwave radiation. However, the phonon intensity does depend on the intensity of the microwave photons. Induced by microwave radiation, the acoustic phonons generated in the cavity are coherent with acoustic phonons. Although acoustic phonons induce transitions between the molecular states, the coherent molecular states are well preserved. Qubits can be formed in a double-dot molecule. The ground state and an excited state in a single quantum dot could also be coherently coupled by microwave photons. However, no superposition is probed in this thesis since other transitions based on the Fermi golden rule induce transport through the dot and it is difficult to achieve a good coupling between electrons and microwave, which always changes greatly with a slight frequency shift (the energy difference between the excited and ground states can not be tuned practically).

In future studies, the spin effect, e.g., *spin-blockade* [Hue01], in charge relaxation processes will be monitored using heterodyne detection techniques in a wide frequency range. Pulsed microwave excitation will be applied to double-dot molecules to monitor time-resolved coherent superposition of molecular states.

6. Conclusion and Outlook

Appendix A

Fabrication Details and Quantum Dot Samples

Detailed Steps for Quantum Dot Fabrication

To fabricate quantum dots from AlGaAs/GaAs heterostructures, the following steps are processed in the following order.

- Cleave the wafer
A piece of sample with an area about $5 \times 5 \text{ mm}^2$ is cleaved from the AlGaAs/GaAs heterostructure wafer. The sample is cleaned with deionized water, acetone, and isopropanol. Supersonic sounds can be applied in cleaning for a short time at low power level.
- Form the mesa
 - Optical lithography
Photoresist: S1805.
Two step spinning of photoresist: 3 sec at 800 rpm and 10 sec at 5000 rpm.
Baking: 30 minutes at 90°C .
Exposure time: 10 sec with Microposit-Entwickler.
Developing time: less than 20 sec, cleaned with deionized water.
 - Etch the mesa
The etchant is $\text{H}_2\text{O}:\text{H}_2\text{SO}_4 (96\%):\text{H}_2\text{O}_2 (30\%) = 100:3:1$ in volume. After the etching, the sample is firstly washed by deionized water followed by cleaning with acetone and isopropanol to remove the residual photoresist.
- Make Ohmic contacts

A. Fabrication Details and Quantum Dot Samples

- Optical lithography
Photoresist: S1818.
Two step spinning of photoresist: 3 sec at 800 rpm and 10 sec at 5000 rpm.
Baking: 30 minutes at 90 °C.
Exposure time: 9 sec with Microposit-Entwickler.
Developing time: less than 20 sec, cleaned with deionized water.
- Evaporation of AuGe/Ni/AuGe layers
Evaporation with e-gun includes three steps:
600 Å AuGe (88:12) + 100 Å Ni + 600 Å AuGe (88:12).
- Lift-off
The lift-off is processed in a hot acetone bath (40 °C). Afterwards, the sample is cleaned using acetone and isopropanol, removing the residual photoresist.
- Anneal to make Ohmic contacts
The sample is annealed with argon protection gas in three steps:
5 min at 110 °C, 2 min at 360 °C, and 0.5 min at 420 °C.
- Make gate contacts
 - Optical lithography
Photoresist: S1813.
Two step spinning of photoresist: 3 sec at 800 rpm and 10 sec at 5000 rpm.
Baking: 30 minutes at 90 °C.
Exposure time: 9 sec with Microposit-Entwickler.
Developing time: less than 20 sec, cleaned with deionized water.
 - Evaporation of gold
50 Å NiCr (50:50) and 1500 Å Au are evaporated from two heat boats, respectively.
 - Lift-off
The lift-off is processed in a hot acetone bath (40 °C). Afterwards, the sample is cleaned using acetone and isopropanol, removing the residual photoresist.
- E-beam lithography: define the quantum dot
 - Spin the e-beam resist PMMA
Two layers PMMA are spun on the sample surface. The first layer is from the 4 % PMMA with a molecular weight of 150000. The Second layer is from the 4 % PMMA with the molecular weight of 500000. Two steps in the spinning are 3 sec at 800 rpm and 30 sec at 6000 rpm. Between the above two steps, the sample is baked at 120 °C at least for 60 min.

-
- E-beam lithography
SEM: JEOL JSM-6400.
Program: Elphy FE plus
E-beam current: 50 pA.
Dose: 250 – 290 $\mu\text{C}/\text{cm}^2$.
Developing: 30 – 40 sec with MIBK:Isopropanol=1:3.
Cleaning: with isopropanol.
 - Evaporation of nanometer sized gold gates
Evaporate 50 Å Ni (rate < 0.3) and 350 Å Au (rate < 0.5) from thermal heat boats.
 - lift-off
The lift-off is processed in a hot acetone bath (40 °C). Afterwards, the sample is cleaned using acetone and isopropanol, removing the residual PMMA.
 - Install the sample into a chip carrier
The sample is first glued into the chip carrier with silver glue (see Fig. A.3). Then the circuits are connected to the pins on the chip carrier by a bonding machine using aluminum wires. Cautions are taken to protect the destructive electrostatic charging.

List of Samples

Samples studied in this thesis are described below.

MOSFET-type Single-Electron Memory

This silicon-based device was fabricated in the group of Prof. Chen in Nanjing University. The structure is the same as that of a conventional floating-gate-MOSFET memory except that the floating gate is made up of a layer of silicon nanocrystals embedded in SiO_2 matrix.

In the fabrication, the layer of nanocrystalline silicon with a thickness of 20 nm was firstly deposited on a p-type silicon substrate by the plasma enhanced chemical vapor deposition (PECVD) using a high hydrogen diluted silane (SiH_4). Then it was thermally annealed in a gas mixture of N_2 and O_2 at 800 °C: A 13 nm thick layer of nanocrystals is sandwiched between two layers of silicon oxide each with a thickness about 2 nm. Above this thermally annealed layer, 500 nm of polysilicon was deposited as the control gate. In the device, the electron channel has a length of 5 μm and a width of 10 μm . Fig. A.1 (b) shows the high-resolution-transmission-electron-microscopy graph (HRTEM) of the layer of nanocrystals. Nanocrystals have a cylindrical shape: It is about 13 nm high along the long axis. The diameter along the short axis is about 5 nm. The characteristics of this device are presented in Sec. 3.1.

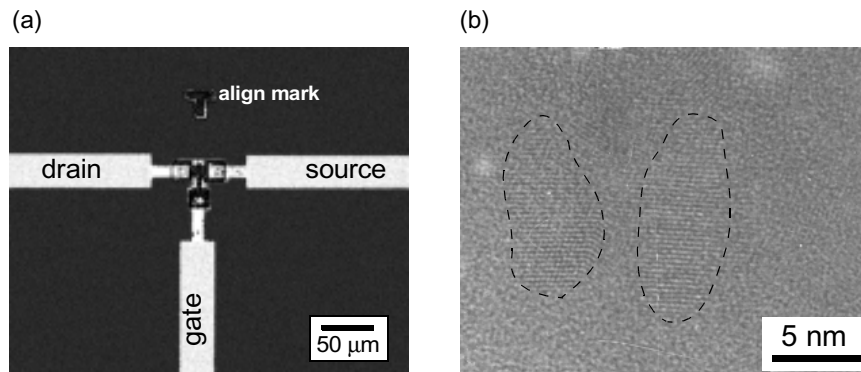


Figure A.1: (a) The top view of a MOSFET memory unit. (b) The High-Resolution-Transmission-Electron-Microscopy (HRTEM) graph of the SiO_x matrix layer between the n -channel and the polysilicon gate (see Fig. 3.1). Isolated nanometer sized silicon crystals are embedded in the matrix.

AlGaAs/GaAs Quantum Dot Samples

- QD-sample#1: The nanometer sized gate structure is shown in Fig. A.2 (a). The basic properties of the AlGaAs/GaAs heterostructure are listed below:
 Type: modulation doped heterostructure from K. Eberl¹
 Depth of 2DEG: 90 nm
 Sheet density: $n_e \approx 1.7 \times 10^{11} \text{ cm}^{-2}$ at 4.2 K
 Electron mobility: $8 \times 10^5 \text{ cm}^2/\text{Vs}$ at 4.2 K

This sample allows for formation of two single dots or a tunnel coupled double dot. In Sec. 3.2, transport spectroscopy of the left single dot is discussed. In Sec. 5.4, broadband microwave spectroscopy of a single dot realized in this sample is presented. The transport and the microwave spectroscopies of a double quantum dot are presented in Sec. 3.3 and Sec. 5.2, respectively.

- QD-sample#2:
 This sample is fabricated by C. Decker [Dec01]. The basic properties of the Al-GaAs/GaAs heterostructure are listed below:
 Type: silicon δ -doped heterostructure from W. Wegscheider² and M. Bichler³
 Depth of 2DEG: 45 nm
 Sheet density: $\approx 2 \times 10^{11} \text{ cm}^{-2}$ at 4.2 K

¹Max-Planck-Institut für Festkörperforschung, Heisenbergstr. 1, D-70569 Stuttgart, Germany.

²Universität Regensburg, Universitätsstr. 31, D-93040 Regensburg, Germany.

³Walter-Schottky-Institut der Technischen Universität München, Am Coulombwall, D-85748 München, Germany.

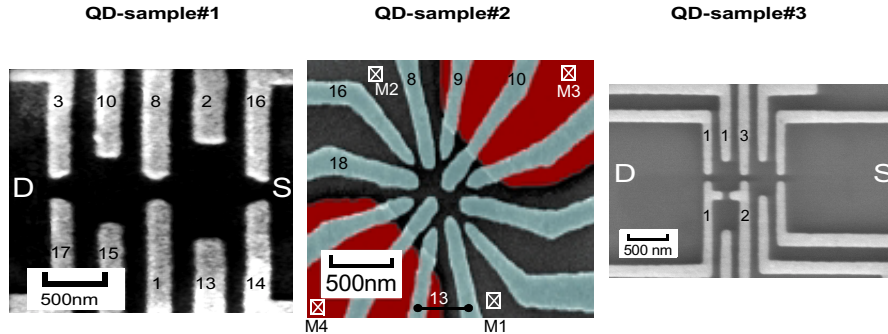


Figure A.2: Three quantum dot samples studied in this thesis. (a) QD-sample#1: A double quantum dot. (b) QD-sample#2: A double quantum dot [Dec01]. The red regions are a layer of Calixarene [TVS⁺99] below the gates, which is about 500 nm thick. The dielectric constant for Calixarene is about 7.1. (c) QD-sample#3: A triple quantum dot [Sim99].

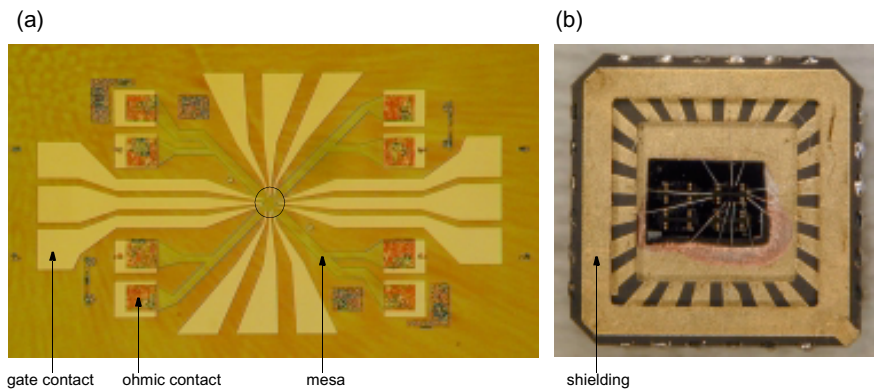


Figure A.3: (a) A chip covered with PMMA before the electron-beam-lithography. (b) A chip is mounted in a chip carrier.

Electron mobility: $8 \times 10^5 \text{ cm}^2/\text{Vs}$ at 4.2 K

In Sec. 5.1, microwave spectroscopy on a single dot realized in this sample is shown.

- QD-sample#3:

This sample is fabricated by F. Simmel [Sim99]. The heterostructure is the same as that used for QD-sample#2. A small quantum dot in the few electron limit is realized in this sample. In Sec. 5.3, photon-assisted tunneling is studied. Kondo effect at finite bias was studied by Simmel *et al* in this sample [Sim99, SBK⁺99].

Appendix B

Measurement Setup

Transport Spectroscopy

Cooled in an OXFORD TLM 400 $^3\text{He}/^4\text{He}$ dilution refrigerator (a cooling power of $400\ \mu\text{W}$ at 100 mK), dc gate voltages and dc drain-source bias are filtered by a low-pass filter (see details in Fig. B.2) and are applied to the quantum dot circuit. Dc sources are supplied by KNICK voltage supplier or YOKOGAWA 7651 voltage/current supplier. The current through the quantum dots is amplified by a current-to-voltage preamplifier (ITHACO 1211) and then is read by a digital multimeter (HP 34401A). For measuring the differential conductance, an ac sinuoidal signal ($V_{p-p} \approx 6\ \mu\text{V}$, $f < 5\ \text{kHz}$) supplied by the reference output of an analog lock-in amplifier (EG&G 124A) is added to the dc drain-source bias (see Fig. B.1). The resulting alternating current is amplified and converted into ac voltage signal by ITHACO 1211. This amplified ac voltage is then detected by the lock-in amplifier EG&G 124A, the output of which is finally read by a HP 34401A.

B. Measurement Setup

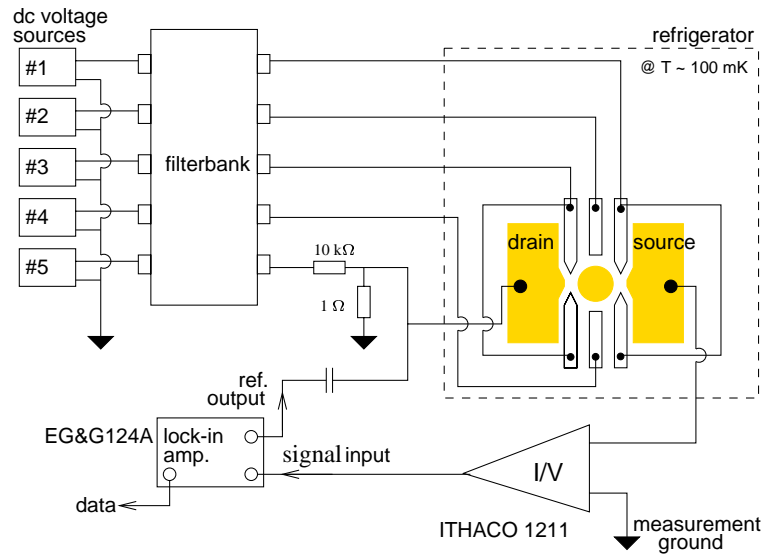


Figure B.1: The setup for measuring the direct current or the differential conductance.

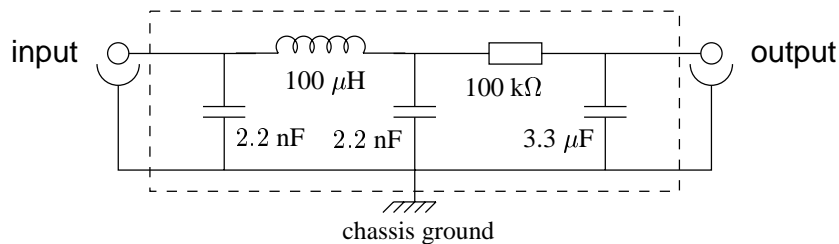


Figure B.2: A unit of the low-pass filter bank as shown in Fig. B.1. The upper pass frequency is 5 Hz.

Microwave Spectroscopy

Microwave antennas

Hertzian wire loop antennas

Two types of Hertzian wire-loop microwave antennas are used for microwave spectroscopy. Both antennas, as shown in Fig. B.3, consist of a loop of metallic wire, which has a diameter around 7 mm. The antennas are electrically separated from the quantum dot circuit. To some extent, the whole heterostructure are uniformly radiated by microwave. This kind of rather simple Hertzian wire-loop antenna is proved to has a wide bandwidth from 1 GHz to 50 GHz (the upper limit is usually determined by the bandwidth of coaxial cables).

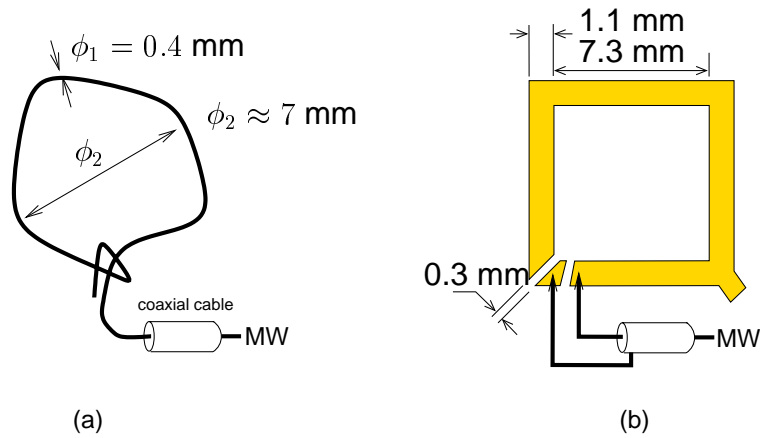


Figure B.3: Two types of Hertzian wire-loop microwave antenna used in this thesis. (a) a wire-loop antenna made of high frequency coaxial cable without the shielding. (b) a wire-loop antenna made of the shielding of the chip carrier.

Nonlinear transmission lines and the bowtie antenna

Nonlinear transmission lines (NLTLs) (see Fig. B.4 (a)) are applied as broadband microwave sources. The details on the NLTLs are described in references [vdW92, vdWBAB93, vdW94, vdWK]. A single input frequency generates short pulses at the output of a NLTL, i.e., a wide-band spectrum is obtained. The typical input frequency is around 8 GHz, the output frequency components are in the range of 20 to 400 GHz (up to the 50-th harmonic). In the experiment setup, the radiation is sent by a bowtie antenna (see Fig. B.4 (b)) through a cylindrical wave guide, which has a lower cut-off at about 80 GHz. Hence, a broadband radiation from 80 GHz to 400 GHz is finally obtained for the microwave spectroscopy of quantum dots.

As shown in Fig. B.4 (c), microwave circuits are assembled in a brass box. In the center, a high-resistive silicon wafer serves as the substrate. On the surface, planar wave guide, power combiner and bowtie antenna are integrated, as shown in Fig. B.4 (b, c). Two NLTLs are glued on the surface and the input and output ports are bounded to the planar wave guides and to the power combiner, respectively (see Fig. B.4 (b)). The broadband microwave is transmitted through the silicon substrate, since it has a high relative static dielectric constant ($\epsilon_r \approx 11.8$) and low dissipation at high resistivity. On the backside of the silicon substrate, a semi-spherical silicon lens is attached (Fig. B.4 (d)), focusing and conducting the radiation into the wave guide of the sample holder. The quantum dot sample is located at the other end of the wave guide at low temperatures.

B. Measurement Setup

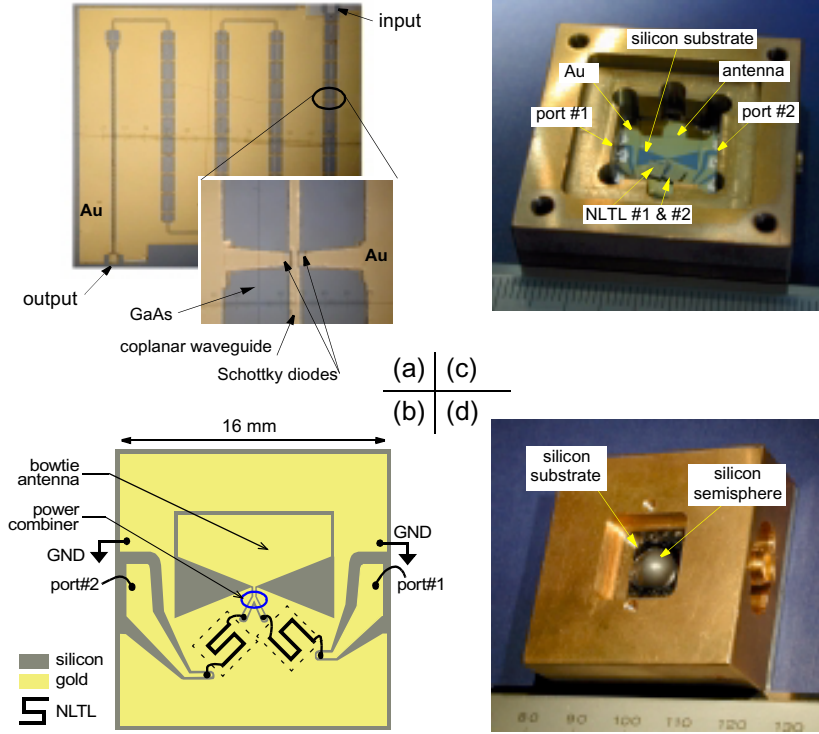


Figure B.4: (a) A nonlinear transmission line. (b) The lithographical layout of the power combiner and bowtie antenna. (c) The front side of the brass box integrating the NLTLs, power combiners, and bowtie antenna on the surface of a high-resistivity silicon substrate. (d) The backside of the box, a silicon hemisphere is attached to the silicon substrate.

Heterodyne Detection Setups

Single band heterodyne detection

As shown in Fig. B.5 (a), in this heterodyne setup, two microwave sources (HP 83711A) are applied to generate microwave beat. Two HP 83711A synthesizers are phased locked. The frequencies are offset slightly, i.e., $\delta f = |f_1 - f_2| = 2.1 \text{ kHz} \ll f_1, f_2 \approx 18.08 \text{ GHz}$. A sinoidal signal at δf is obtained by a mixer and amplified by a voltage preamplifier to serve as the reference signal for a lock-in amplifier (EG&G 124A). Then, the two microwave signals are added with a power combiner (HP part 0955-450 KRYTAR), frequency doubled by a frequency multiplier (MITEQ MX 2V260400), and filtered by a band pass filter (QUINSTAR QFA-3715-BA) which has a center frequency around 32 GHz. Finally the microwave is fed to a coaxial line, at the end of which a Hertzian wire-loop antenna (see page 118) is attached. The

microwave-induced complex current is detected by the lock-in amplifier at δf .

Broadband heterodyne setup

Similar to the scheme shown in Fig. B.5 (a), broadband heterodyne detection of microwave-induced complex current are realized, as shown in Fig. B.5 (b). Two coherent broadband microwave sources, instead of two single microwave sources, are combined. The broadband microwaves are generated by two NLTLs which are coherently driven by two microwave synthesizers, respectively. The combined microwave signal is transmitted by a bowtie antenna through a wave guide in the sample holder to the quantum dot sample. The frequencies applied are $f_1 = 7.8$ GHz, $f_2 = f_1 + \delta f$, and $\delta f = 21$ Hz.

Measurement Program

The program used for automatic measurements is *GPplus*, which is written by myself for Windows systems (ver. 9x). GPplus itself is used as a measurement task generator and the real-time data viewer. Once the measurement is planned and the task is formatted into single task files, GPplus send these tasks to an executor, i.e., a *virtual instrument* written with Labview language (ver. 5.0), which controls the instruments, gathers the data, and sends the data to GPplus. Finally, GPplus plots and save the measured data.

GPplus is capable of controlling various instruments via IEEE-488 GPIB bus or RS232 serial ports. By trying to find out the exact commands for controlling the instruments and write simple Labview programs, one has the tool at hand to make complicated measurement tasks. This program is available on demand (hua_qin72@yahoo.com).

B. Measurement Setup

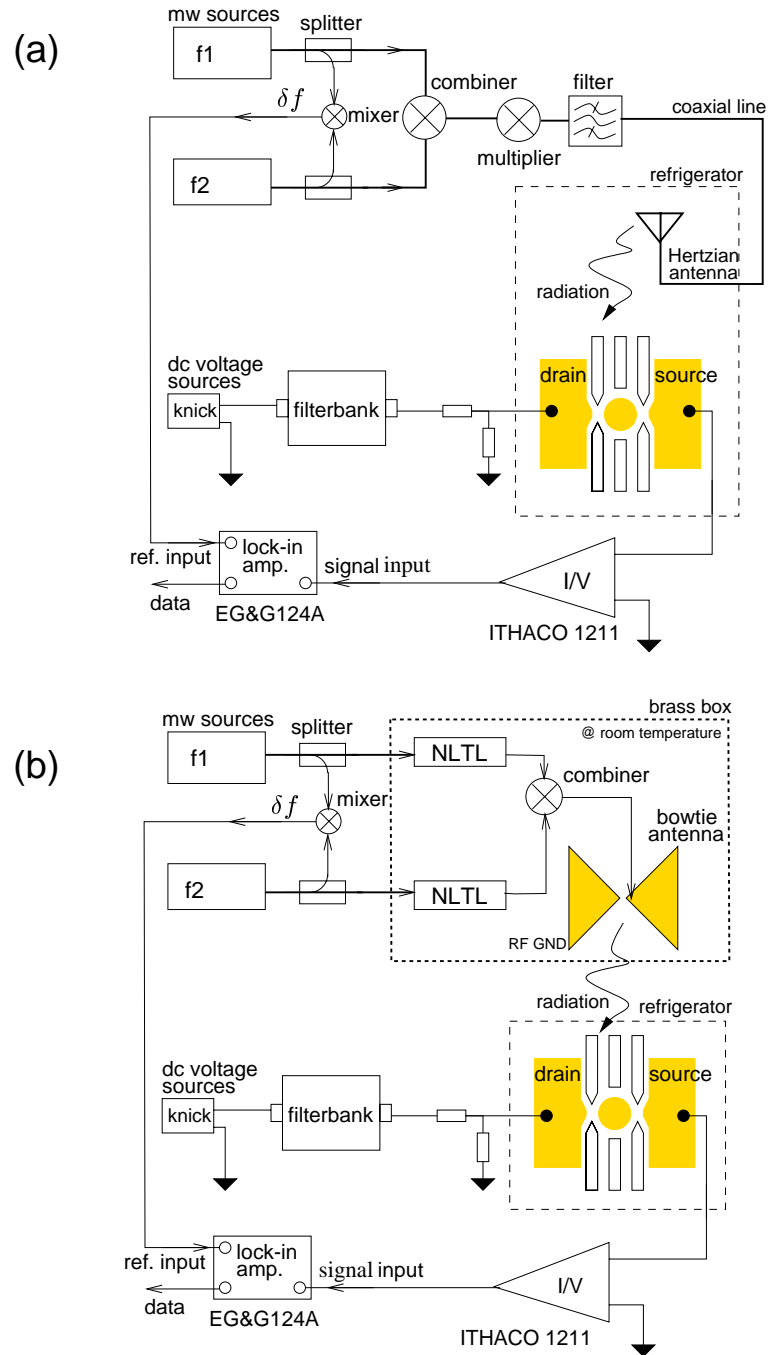


Figure B.5: (a) Single-band heterodyne detection. (b) Broad-band heterodyne detection.

Appendix C

Equivalent Circuit of A Double Dot

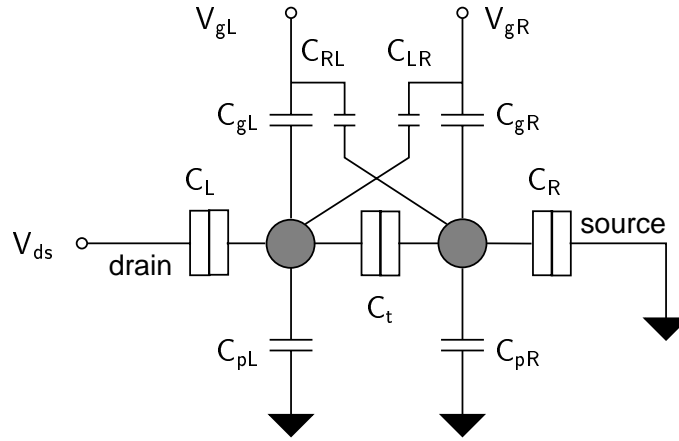


Figure C.1: The equivalent circuit of a tunnel-coupled double quantum dot according to the constant interaction model, i.e., electron-electron interactions are described with relevant capacitances.

The equivalent circuit is similar to that shown in Fig. 2.6 (on page 24). Here, the parasitic capacitance C_{pL} and C_{pR} for the left and right dot are included as well. The factors defined in Eqs. [2.32,2.33,2.34] are evaluated as the following:

$$\begin{aligned}\gamma_{gL} &= \frac{C_t C_{RL} + C_{gL}(C_{gR} + C_R + C_{RL} + C_{pR} + C_t)}{(C_{gL} + C_L + C_{LR} + C_{pL} + C_t)(C_{gR} + C_R + C_{RL} + C_{pR} + C_t)}, \\ \gamma_{gR} &= \frac{C_t C_{LR} + C_{gR}(C_{gL} + C_L + C_{LR} + C_{pL} + C_t)}{(C_{gL} + C_L + C_{LR} + C_{pL} + C_t)(C_{gR} + C_R + C_{RL} + C_{pR} + C_t)}, \\ \gamma_{RL} &= \frac{C_t C_{gL} + C_{RL}(C_{gL} + C_L + C_{LR} + C_{pL} + C_t)}{(C_{gL} + C_L + C_{LR} + C_{pL} + C_t)(C_{gR} + C_R + C_{RL} + C_{pR} + C_t)},\end{aligned}$$

C. Equivalent Circuit of A Double Dot

$$\begin{aligned}\gamma_{LR} &= \frac{C_t C_{gR} + C_{LR}(C_{gR} + C_R + C_{RL} + C_{pR} + C_t)}{(C_{gL} + C_L + C_{LR} + C_{pL} + C_t)(C_{gR} + C_R + C_{RL} + C_{pR} + C_t)}, \\ \gamma_{dL} &= \frac{C_t}{C_{\Sigma L}}, \\ \gamma_{dR} &= \gamma_{dL} \gamma_{QL}, \\ \gamma_{QL} &= \frac{C_t}{C_{gR} + C_R + C_{RL} + C_{pR} + C_t}, \\ \gamma_{QR} &= \frac{C_t}{C_{gL} + C_L + C_{LR} + C_{pL} + C_t}, \\ C_{\Sigma L} &= C_{gL} + C_L + C_{LR} + C_{pL} + \frac{C_t(C_{gR} + C_R + C_{RL} + C_{pR})}{C_{gR} + C_R + C_{RL} + C_{pR} + C_t}, \\ C_{\Sigma R} &= C_{gR} + C_R + C_{RL} + C_{pR} + \frac{C_t(C_{gL} + C_L + C_{LR} + C_{pL})}{C_{gL} + C_L + C_{LR} + C_{pL} + C_t}.\end{aligned}$$

Bibliography

- [AGKL97] B. L. Altshuler, Y. Gefen, A. Kamenev, and L. S. Levitov, Phys. Rev. Lett. **78** (1997), 2803.
- [AK00] R. Aguado and L. P. Kouwenhoven, Phys. Rev. Lett. **84** (2000), 1986.
- [AL91] D. V. Averin and K. K. Likharev, *Mesoscopic phenomena in solids*, p. 173, North-Holland, Amsterdam, 1991.
- [Alh00] Y. Alhassid, Rev. Mod. Phys. **72** (2000), 895.
- [AN90] D. V. Averin and Yu. N. Nazarov, Phys. Rev. Lett. **65** (1990), 2446.
- [AN92] D. V. Averin and Yu. V. Nazarov, in *Single charge tunneling: Coulomb blockade phenomena in nanostructures*, see Chap. 6 in Ref. [GD92].
- [Ash96] R. C. Ashoori, Nature **379** (1996), 413.
- [ASW⁺93] R. C. Ashoori, H. L. Stoermer, J. S. Weiner, L. N. Pfeiffer, K. W. Baldwin, and K. W. West, Phys. Rev. Lett. **71** (1993), 613.
- [AWM97] I. L. Aleiner, N. S. Wingreen, and Y. Meir, Phys. Rev. Lett. **79** (1997), 3740.
- [Bar95] A. Barenco, Phys. Rev. Lett. **74** (1995), 4083.
- [BB48] J. Bardeen and W. H. Brattain, Phys. Rev. **74** (1948), 230.
- [BBS97] Ph. Brune, C. Bruder, and H. Schoeller, Phys. Rev. B **56** (1997), 4730.
- [Bee91] C. W. J. Beenakker, Phys. Rev. B **44** (1991), 1646.
- [BHvdW⁺95] R. H. Blick, R. J. Haug, D. W. van der Weide, K. von Klitzing, and K. Eberl, Appl. Phys. Lett. **67** (1995), 3924.

- [BHvKE96] R. H. Blick, R. J. Haug, K. von Klitzing, and K. Eberl, *Surf. Science* **361** (1996), 595.
- [BL82] M. Buettiker and R. Landauer, *Phys. Rev. Lett.* **49** (1982), 1739.
- [BPT93a] M. Buettiker, A. Prêtre, and H. Thomas, *Phys. Rev. Lett.* **70** (1993), 4114.
- [BPT93b] M. Buettiker, A. Prêtre, and H. Thomas, *Phys. Rev. Lett.* **71** (1993), 465.
- [BRB01] T. Brandes, F. Renzoni, and R. H. Blick, cond-mat/0104435, to appear in *Phys. Rev. B*.
- [BS94] C. Bruder and H. Schoeller, *Phys. Rev. Lett.* **72** (1994), 1076.
- [BSH⁺98] E. Buks, R. Schuster, M. Heiblum, D. Mahalu, and V. Umansky, *Nature* **391** (1998).
- [Bue00] M. Buettiker, *J. Low Temp. Phys.* **118** (2000), 519.
- [BvdWHE98] R. H. Blick, D. W. van der Weide, R. J. Haug, and K. Eberl, *Phys. Rev. Lett.* **81** (1998), 689.
- [BWvKP91] T. Bever, A. D. Wieck, K. von Klitzing, and K. Ploog, *Phys. Rev. B* **44** (1991), 3424.
- [Dat95] S. Datta, *Electronic transport in mesoscopic systems*, Cambridge University Press, Cambridge, New York, 1995.
- [Dec01] C. Decker, *Spineffekte in kleinen Quantenpunkten*, Diplomarbeit, Ludwig-Maximilians-Universität München, February, 2001.
- [DLH⁺94] H. Drexler, D. Leonard, W. Hansen, J. P. Kotthaus, and P. M. Petroff, *Phys. Rev. Lett.* **73** (1994), 2252.
- [DS00] M. H. Devoret and R. J. Schoelkopf, *Nature* **406** (2000), 1039.
- [Eto01] M. Eto, cond-mat/0101345.
- [FD93] Y. Fu and S. C. Dudley, *Phys. Rev. Lett.* **70** (1993), 65.
- [FMM⁺93] E. B. Foxman, P.L. McEuen, U. Meirav, N.S. Wingreen, Y. Meir, P.A. Belk, N. R. Belk, M.A. Kastner, and S. J. Wind, *Phys. Rev. B* **47** (1993), 10020.

- [FOvdW⁺00] T. Fujisawa, T.H. Oosterkamp, W.G. van der Wiel, B.W. Broer, R. Aguado, S. Tarucha, , and L.P. Kouwenhoven, *Science* **282** (2000), 932.
- [FSE⁺01] S. De Franceschi, S. Sasaki, J. M. Elzerman, W. G. van der Wiel, S. Tarucha, and L. P. Kouwenhoven, *Phys. Rev. Lett.* **86** (2001), 878.
- [FT97] T. Fujisawa and S. Tarucha, *Superlattices and Microstructures* **21** (1997), 247.
- [FTH01] T. Fujisawa, Y. Tokura, and Y. Hirayama, *Phys. Rev. B* **63** (2001), 81304.
- [FvdWK00] T. Fujisawa, W.G. van der Wiel, and L.P. Kouwenhoven, *Physica E* **7** (2000), 413.
- [GD92] H. Grabert and M. H. Devoret (eds.), *Single charge tunneling: Coulomb blockade phenomena in nanostructures*, series B: physics, no. 294, NATO Advanced Study Institute, Plenum, New York, 1992.
- [GGGK⁺98] D. Goldhaber-Gordon, J. Goeres, M. A. Kastner, H. Shtrikman, D. Mahalu, and U. Meirav, *Phys. Rev. Lett.* **81** (1998), 5225.
- [GGSM⁺98] D. Goldhaber-Gordon, Hadas Shtrikman, D. Mahalu, D. Abusch-Magder, U. Meirav, and M. A. Kastner, *Nature* **391** (1998), 156.
- [GLC97] L. Guo, E. Leobandung, and S. Y. Chou, *Appl. Phys. Lett.* **70** (1997), 850.
- [GM90] L. I. Glazman and K. A. Matveev, *JETP Lett.* **51** (1990), 484.
- [Gur97] S. A. Gurvitz, *Phys. Rev. B* **56** (1997), 15215.
- [GZ68] I. Giaever and H. R. Zeller, *Phys. Rev. Lett.* **20** (1968), 1504.
- [HIL⁺89] W. Hansen, T. P. Smith III, K. Y. Lee, J. A. Brum, C. M. Knoedler, J. M. Hong, and D. P. Kern, *Phys. Rev. Lett.* **62** (1989), 2168.
- [HK93] D. Heitmann and J. P. Kotthaus, *Phys. Today* (1993), 56.
- [HO94] G. Y. Hu and R. F. O'Connell, *Phys. Rev. B* **49** (1994), 16505.
- [HTL⁺94] J. M. Hergenrother, M. T. Tuominen, J. G. Lu, D. C. Ralph, and M. Tinkham, *Physica B* **203** (1994), 327.

- [Hue01] A. Huettel, *Tunnelgekoppelte Quantenpunktsysteme und ihre kapazitive Wechselwirkung*, Diplomarbeit, Ludwig-Maximilians-Universität München, February, 2001.
- [Imr97] Y. Imry, *Introduction to mesoscopic physics*, Oxford University Press, New York, Oxford, 1997.
- [JWM94] A. P. Jauho, N. S. Wingreen, and Y. Meir, *Phys. Rev. B* **50** (1994), 5528.
- [KAA⁺00] S. Komiyama, O. Astafiev, V. Antonov, T. Kutsuwa, and H. Hirai, *Nature* **403** (2000), 405.
- [Kas93] M. A. Kastner, *Phys. Today* **46** (1) (1993), 24.
- [KEMZ99] M. W. Keller, A. Eichenberger, J. M. Martinis, and N. M. Zimmerman, *Science* **285** (1999), 1706.
- [KF99] F. Lieftrink P. Teunissen K. Flensberg, A. A. Odintsov, *Int. J. Mod. Phys. B* **13** (1999), 2651.
- [KMM⁺97] L. P. Kouwenhoven, C. M. Marcus, P. L. Mceuen, S. Tarucha, R. M. Westervelt, and N. S. Wingreen, *Mesoscopic electron transport*, no. 345, NATO Advanced Study Institute, Kluwer, Dordrecht, 1997.
- [Kou95] L. P. Kouwenhoven, *Science* **268** (1995), 1440.
- [KR94] V. I. Kozub and A. M. Rudin, *Phys. Rev. B* **49** (1994), 5710.
- [Kum92] A. Kumar, *Surf. Sci.* **263** (1992), 335.
- [Lan96] R. Landauer, *Science* **272** (1996), 1914.
- [LCW⁺96] C. Livermore, C. H. Crouch, R. M. Westervelt, K. L. Campman, and A. C. Gossard, *Science* **274** (1996), 1332.
- [LD98] D. Loss and D. P. DiVincenzo, *Phys. Rev. A* **57** (1998), 120.
- [Mat99] J. C. Mather, *Nature* **401** (1999), 654.
- [MF95] U. Meirav and E. B. Foxman, *Semicond. Sci. Technol.* **10** (1995), 255.
- [MOL⁺99] J. E. Mooij, T. P. Orlando, L. Levitov, Lin Tian, Caspar H. van der Wal, and Seth Lloyd, *Science* **285** (1999), 1036.

-
- [NPT99] Y. Nakamura, Yu A. Pashkin, and J. S. Tsai, *Nature* **398** (1999), 786.
- [OBS92] A. A. Odintsov, V. Bubanja, and G. Schoen, *Phys. Rev. B* **46** (1992), 6875.
- [OFvdW⁺98] T.H. Oosterkamp, T. Fujisawa, W.G. van der Wiel, K. Ishibashi, R.V. Hijman, S. Tarucha, and L.P. Kouwenhoven, *Nature* **395** (1998), 873.
- [OKAEAKH97] T. H. Oosterkamp, L. P. Kouwenhoven, N. C. van der Vaart A. E. A. Koolen, and C. J. P. M. Harmans, *Phys. Rev. Lett.* **76** (1997), 1536.
- [OKK⁺96] T. H. Oosterkamp, L. P. Kouwenhoven, A. E. A. Koolen, N. C. van der Vaart, and C. J. P. M. Harmans, *Semicond. Sci. Technol.* **11** (1996), 1512.
- [PCS⁺98] S. R. Patel, S. M. Cronenwett, D. R. Stewart, C. M. Marcus, C. I. Duruoetz, J. S. Harris, Jr, K. Campman, and A. C. Gossard, *Phys. Rev. Lett.* **80** (1998), 4522.
- [Pfa98] D. Pfannkuche, *Aspects of coulomb interactions in semiconductor nanostructures*, 1998, Habilitationsschrift, Stuttgart.
- [QBK⁺01] H. Qin, R. H. Blick, J. P. Kotthaus, W. Wegscheider, and M. Bichler, *Phys. Rev. B* **63** (2001), 35320.
- [QGL⁺99] H. Qin, X. Gu, H. Lu, J. Liu, X. Huang, and K. Chen, *Solid State Commun.* **111** (1999), 171.
- [RCU96] F. Ramirez, E. Cota, and S. E. Ulloa, *Superlattics and Microstructures* **20** (4) (1996), 523.
- [RJSaP98] A. A. Kozhevnikov and P. Delsing R. J. Schoelkopf and, P. Wahlgren and and D. Prober, *Science* **280** (1998), 1238.
- [SBA⁺96] U. Sivan, R. Berkovits, Y. Aloni, O. Prus, A. Auerbach, and G. Ben-Yoseph, *Phys. Rev. Lett.* **77** (1996), 1123.
- [SBK⁺99] F. Simmel, R. H. Blick, J. P. Kotthaus, W. Wegscheider, and M. Bichler, *Phys. Rev. Lett.* **83** (1999), 804.
- [SFE⁺00] S. Sasaki, S. De Franceschi, J. M. Elzerman, W. G. van der Wiel, M. Eto, S. Tarucha, and L. P. Kouwenhoven, *Nature* **405** (2000).
- [SHM00] A. Yu. Smirnov, N. J. M. Horing, and L. G. Mourokh, *Appl. Phys. Lett.* **77** (2000), 2578.

- [SHW97] F. Simmel, T. Heinzel, and D. A. Wharam, *Europhys. Lett.* **38** (1997), 123.
- [SIA94] U. Sivan, Y. Imry, and A. G. Aronov, *Europhys. Lett.* **28** (1994), 115.
- [Sim99] F. Simmel, *Transporteigenschaften von Quantenpunkten*, Ph.D. thesis, Ludwig-Maximilians-Universität München, May 1999.
- [SL97] Q. Sun and T. Lin, *J. Phys.: Condens. Matter* **9** (1997), 4875.
- [SL98] Q. Sun and T. Lin, *Phys. Rev. B* **58** (1998), 13007.
- [SMCG99] M. Switkes, C. M. Marcus, K. Campman, and A. C. Gossard, *Science* **283** (1999), 1905.
- [SN96] T.H. Stoof and Yu.V. Nazarov, *Phys. Rev. B* **53** (1996), 1050.
- [SS97] A. Shnirman and G. Schoen, *Phys. Rev. B* **57** (1997), 15400.
- [STFK⁺89] J. H. F. Scott-Thomas, S. B. Field, M. A. Kastner, H. I. Smith, and D. A. Antonadis, *Phys. Rev. Lett.* **62** (1989), 583.
- [Sto96] M. Stopa, *Phys. Rev. B* **54** (1996), 13767.
- [SW96] C. A. Stafford and Ned. S. Wingreen, *Phys. Rev. Lett.* **76** (1996), 1916.
- [SWL00] Q. Sun, J. Wang, and T. Lin, *Phys. Rev. B* **61** (2000), 12643.
- [Sze85] S. M. Sze, *Semiconductor devices: Physics and technology*, John Wiley & Sons, 1985.
- [Tho77] D. J. Thouless, *Phys. Rev. Lett.* **39** (1977), 1167.
- [Til00] A. Tilke, *Einzelelektronentransport in Silicon-on-Insulator-Nanostrukturen*, Ph.D. thesis, Ludwig-Maximilians-Universität München, April 2000.
- [TRH⁺96] S. Tiwari, F. Rana, H. Hanafi, A. Hartstein, E. F. Crabbe, and K. Chan, *Appl. Phys. Lett.* **68** (1996), 1377.
- [TVS⁺99] A. Tilke, M. Vogel, F. Simmel, A. Kriele, R. H. Blick, H. Lorenz, D. A. Wharam, and J. P. Kotthaus, *J. Vac. Sci. Technol.* (1999).
- [uJPG63] P. K. Tien und J. P. Gordon, *Phys. Rev.* **129** (1963), 647.

- [vdW92] Daniel Warren van der Weide, *All-electronic generation and detection of terahertz free-space radiation with subpicosecond pulses*, Ph.D. thesis, Stanford University, December 1992.
- [vdW94] D. W. van der Weide, *J. Opt. Soc. B* **11** (1994), 2553.
- [vdWBAB93] D. W. van der Weide, J. S. Bostak, B. A. Auld, and D. M. Bloom, *Appl. Phys. Lett.* **62** (1993), 22.
- [vdWK] D. W. van der Weide and F. Keilman, U. S. patent 5,748,309, May 5 (1998).
- [vdWtHW⁺00] Caspar H. van der Wal, A. C. J. ter Haar, F. K. Wilhelm, R. N. Schouten, C. J. P. M. Harmans, T. P. Orlando, Seth Lloyd, and J. E. Mooij, *Science* **290** (2000), 773.
- [vHBS92] H. van Houten, C. W. J. Beenakker, and A. A. M. Staring, in *Single charge tunneling: Coulomb blockade phenomena in nanostructures*, see Chap. 5 in Ref. [GD92].
- [VLV⁺96] E. H. Visscher, J. Lindeman, S. M. Verbrugh, P. Hadley, J. E. Mooij, and W. van der Vleuten, *Appl. Phys. Lett.* **68** (1996), 2014.
- [VOJ⁺95] D. Vion, P. F. Orfila, P. Joyez, D. Esteve, and M. H. Devoret, *J. of Appl. Phys.* **77** (1995), 2519.
- [vWvHB⁺88] B. J. van Wees, H. van Houten, C. W. J. Beenakker, J. G. Williamson, L. P. Kouwenhoven, D. van der Marel, and C. T. Foxon, *Phys. Rev. Lett.* **60** (1988), 848.
- [Wal85] J. R. Waldram, *The theory of thermodynamics*, ch. 2, p. 17, Cambridge university press, Cambridge, 1985.
- [WHvKE95] J. Weis, R. J. Haug, K. von Klitzing, and K. Eberl, *Semicond. Sci. Technol.* **10** (1995), 877.
- [WHvKP93] J. Weis, R. J. Haug, K. von Klitzing, and K. Ploog, *Phys. Rev. Lett.* **71** (1993), 4019.
- [WJM93] N. S. Wingreen, A. Jauho, and Y. Meir, *Phys. Rev. B* **48** (1993), 8487.
- [WSW⁺89] A. Wixforth, J. Scriba, M. Wassermeier, J. P. Kotthaus, G. Weimann, and W. Schlapp, *Phys. Rev. B* **40** (1989), 7874.
- [ZS91] W. Zwerger and M. Scharpf, *Z. Phys. B* **85** (1991), 421.

Bibliography

Acknowledgement

I am grateful to many people for their help during my study in Munich. Without their help, I would not have this work smoothly done. I would like to express my special thanks to the following people and the organizations.

I thank the Volkswagen-Stiftung (Dr. von Lengerke) and the DAAD team (Birgit Zelt, Udo Hornberger, Ralf Meuter, Stefan Heinemann, and others) for the financial support. Without these support and help none of this research would have been possible.

I thank Prof. Dr. Jörg P. Kotthaus for giving me an opportunity to do such an interesting and exciting research. His insight into physics helped me to understand many experimental data. He is leading a group very active in nanoscience. The frequent international exchanges of ideas always bring the group's scientific researches up-to-date.

I thank Dr. Robert H. Blick for directing me in this research work. As the direct advisor, he impressed me with his great enthusiasm over physics. His ideas and insight into physics always encouraged me to explore more interesting phenomena. He gave me his only piece of AlGaAs/GaAs heterostructure. It was him who made introductions to me on many beautiful microwave components. It was from him that I learned how to handle and even anatomize the coolest site in Munich. Under his suggestion, I developed the *GPplus* for measurement. Without his efforts, I can hardly imagine how could I get through these three years.

I was impressed by the successful and efficient collaboration with Prof. Daniel W. van der Weide. In one week, he directed me to design and integrate a wideband microwave combiner and a bowtie antenna on a single silicon substrate. He even assembled two nonlinear transmission lines onto this circuit and formed a wideband spectrometer. I thank him for providing us his valuable NLTLs and for revising my manuscripts.

I thank my former super advisor Prof. Kun-ji Chen for guiding me to the realm of mesoscopic physics for the first time: Dr. Xiao-feng Gu and me overcome many unexpected difficulties to fabricate a prototype of single-electron memory at room temperature.

Helmut Krömmer gave me his detailed and strict operation rules in the clean room. Based on these rules, I am confident to make successful nanometer fabrications.

I thank Dr. Friedrich Simmel for guiding me through the basic experiments in the dilfridge room: I did the first successful measurement with one of his samples.

I thank Dr. Qing-feng Sun and Prof. Tsung-han Lin for helpful discussion on photon-assisted tunneling and the non-adiabatic pumping effect.

Alexander W. Holleitner is a nice collaborator. I thank him for always carefully correcting manuscripts for me. Actually, he is enthusiastic over not only semiconductor quantum dots but also the whole life.

I thank Stephan Manus for giving me many tips on microwave experiments and on measurement techniques.

I thank Robert A. Wildfeuer, Andreas K. Hüttel, and Carsten R. Decker for having chances to learn other interesting topics in physics from their “Diplomarbeiten”.

I thank Pit Kiermeier for supporting me enough liquid helium and nitrogen.

The time spent with Markus Vogel and Dr. Artur Erbe in our “printer”-room was always joyful. We have computers installed with Mac Os, Windows, and Linux. They suggested me to use Linux instead of Windows. Then in my computer I have a Chinese version of Linux. They can only use the console without difficulties.

I thank all those people who personally helped and concerned about me.

My parents never stop giving me their love and they expect no return but only that I am fine. I wish them all in health. 我要感谢我的父母给予我的关怀，支持和谅解。我的收获和他们的付出是无法分开的。

I thank many friends in Nanjing and new friends in Munich for giving me encouragement and help.

I thank my wife for being side by side with me. Without her care and support in my life, it would not have been possible for me to finish this work. She also partly processed the layout of my thesis, improved the figures and designed transparencies for my talks.

Curriculum Vitae

Hua Qin, born on the 9th October 1972 in Wujin, China, married

- 1979 – 1984, in Tianjing Primary School, Wujin, China
- 1984 – 1987, in Daixi Middle School, Wujin, China
- 1987 – 1990, in Qianhuang High School, Wujin, China
- 1990 – 1994, bachelor degree in the Physics Department of Nanjing University, Nanjing, China
- 1994 – 1996, pursuing the master degree of Semiconductor Physics and Semiconductor Device Applications in the Physics Department of Nanjing University, Nanjing, China
- 1996 – 1998, Ph. D study on *low-dimensional transport through silicon nanocrystals* in the group of Prof. K. Chen, in the Physics Department of Nanjing University, Nanjing, China
- Since September 1998, Ph. D study on *single-electron tunneling under microwave radiation* in the group of Prof. Dr. J. P. Kotthaus, in the Physics Department of LMU, Munich, Germany

